

**Photometric modeling of Saturn's rings:  
I. Monte Carlo method and the effect of non-zero volume filling factor**

Heikki Salo and Raine Karjalainen

*Dept. of Physical Sciences, Astronomy Division, Univ. of Oulu, P.O. BOX 3000, FIN-90014  
Oulun yliopisto, Finland*

`heikki.salo@oulu.fi`

November 1st, 2001 revised March 21th, 2003

**ABSTRACT**

The scattering properties of particulate rings with volume filling factors in the interval  $D = 0.001 - 0.3$  are studied, with photometric Monte Carlo ray tracing simulations combining the advantages of direct (photons followed from the source) and indirect methods (brightness as seen from the observing direction). Besides vertically homogeneous models, ranging from monolayers to classical many-particle thick rings, particle distributions obtained from dynamical simulations are studied, possessing a non-uniform vertical profile and a power law distribution of particle sizes. Self-gravity is not included to assure homogeneity in planar directions. Our main goal is to check whether the moderately flattened ring models predicted by dynamical simulations (with central plane  $D > 0.1$ ) are consistent with the basic photometric properties of Saturn's rings seen in ground-based observations, including the brightening near zero phase angle (opposition effect), and the brightening of the B-ring with increasing elevation angle (tilt effect).

Our photometric simulations indicate that dense rings are typically brighter in reflected light than those with  $D \rightarrow 0$ , due to enhanced single scattering. For a vertically illuminated layer of identical particles this enhancement amounts at intermediate viewing elevations to roughly  $1 + 2D$ . Increased single scattering is also obtained for low elevation illumination, further augmented at low phase angles  $\alpha$  by the opposition brightening when  $D$  increases: the simulated opposition effect agrees very well with the Lumme and Bowell (1981, *AJ* 86, 1694-1704) theoretical formula. For large  $\alpha$  the total intensity may also decrease, due to reduced amount of multiple scattering. For the low ( $\alpha = 13^\circ$ ) and high ( $\alpha = 155^\circ$ ) phase angle geometries analyzed in (Dones *et al.*, 1993, *Icarus* 105, 184-215) the brightness change for  $D = 0.1$  amounts to 20 % and -17 %, respectively.

In the case of an extended size distribution, dynamical simulations indicate that the smallest particles typically occupy a layer several times thicker than the largest particles. Even if the large particles form a dynamically dense system, a narrow opposition peak can arise due to mutual shadowing among the small particles: for example, a size

distribution extending about two decades can account for the observed about 1 degree wide opposition peak, solely in terms of mutual shadowing. The reduced width of the opposition peak for extended size distribution is in accordance with Hapke’s (1986, *Icarus* 67, 264-280) treatment for semi-infinite layers. Due to vertical profile and particle size distribution, the photometric behavior is sensitive to the viewing elevation: this can account for the tilt-effect of the B-ring, as dense and thus bright central parts of the ring become better visible for larger elevation, whereas in the case of smaller elevation, mainly low volume density upper layers are visible. Since multiple scattering is not involved, the explanation works also for albedo well below unity.

Inclusion of non-zero volume density helps also to model some of the Voyager observations. For example, the discrepancy between predicted and observed brightness at large phase angles for much of the A-ring (Dones *et al.*, 1993) is removed when the enhanced low  $\alpha$  single scattering and reduced large  $\alpha$  multiple scattering is allowed for. Also, a model with vertical thickness increasing with Saturnocentric distance offers at least a qualitative explanation for the observed contrast reversal between the inner and outer A ring in low and high phase Voyager images. Differences in local size distribution and thus on the effective  $D$  may also account for the contrast reversal in resonance sites.

*Subject headings:* planetary rings, Saturn, photometry, radiative transfer, collisional physics, computer techniques

## 1. Introduction

Dynamical models for the collisional steady-state in planetary rings suggest the rings to be fairly flattened, with vertical thickness well below the observational (Lane et al. 1982) upper limit of  $\sim 200$  meters. For example, simulations with the standard elasticity model based on Bridges *et al.*’s (1984) laboratory measurements indicate a ring thickness of only a few tens of meters at most, when the particles’ size distribution is included (Salo 1992b). The largest meter-sized particles, where most of the ring mass resides, are expected to be even more concentrated to the central plane. These simulation thickness estimates are consistent with the various estimates of local velocity dispersion in resonance locations, suggesting a vertical thickness of 10 – 100 meters (see Cuzzi et al. 1984). For optical depths near unity, dynamical models imply central plane volume filling factors  $D(0) \sim 0.1 - 0.3$ . For such highly flattened ring models the mutual self-gravity between particles becomes significant, leading to the formation of local gravitational wakes (Salo 1992a, 1995; Richardson 1994; Daisaka and Ida 1999; Ohtsuki and Emori 2000), essentially similar to Julian and Toomre (1966) wakes in stellar systems. Dynamical wakes, trailing by about 20 degree with respect to the local tangential direction, provide a plausible candidate for the observed bi-symmetric azimuthal brightness variations in the outer parts of Saturn’s rings (Franklin et al. 1987; Dones et al. 1993). In the wakes the volume filling factor is further enhanced.

Practically all photometric modeling of Saturn’s rings has been done in the framework of classical radiative transfer, assuming that the rings are a thick homogeneous multilayer of particles, with a very small volume filling factor (particle separations much larger than their diameters). Studies of interparticle shadowing in homogeneous ring models (Lumme et al. 1983) have indicated that a volume filling factor  $D \approx 0.02$  would explain the observed B-ring opposition-effect, i.e. the increase in the amount of reflected light when the rings are viewed close to zero phase-angle (Sun-ring-observer angle). Likewise, the same models as well as those with  $D = 0$  (Lumme and Irvine 1976; Esposito and Lumme 1977) can explain the brightening of the B-ring with an increasing ring opening angle (“tilt-effect”), in terms of multiple scattering, provided that the particle albedo is close to unity. The only other model studied in detail (Hämeen-Anttila and Vaaranen 1975) has been the extreme monolayer (a 2-D distribution of particles), which however, fails to reproduce correctly the above-mentioned two basic observational phenomena (see Cuzzi et al. (1984)).

So far rather few attempts have been made to reconcile the dynamical and photometric views of rings. Dones et al. (1993) point out that many discrepancies in the photometric behavior of the inner and middle A-ring, and of the B-ring (Doyle et al. 1989), as compared to the classical radiative transfer models with  $D = 0$ , would be naturally accounted for by assuming the rings to be vertically thin. This would be expected to increase the single scattering contribution over the classical value, modifying the deduced single particle phase function and albedo, and thus also affecting the calculated multiply scattered intensities. For example, this might help to match both the low and high phase angle Voyager observations (Dones et al. 1993). Support for the importance of finite ring thickness was given by the ray-tracing calculations in Dones et al. (1989), implying significant brightening of a monolayer model in comparison to a many particle thick multilayer. Increased brightness was also obtained by Peltoniemi and Lumme (1992) in their study of closely packed particulate media. Nevertheless, systematic study of the effects of finite ring thickness, or equivalently, of volume filling factor significantly exceeding zero, is still missing. Especially important would be to address whether dynamical models of moderately flattened rings, falling between the above mentioned two extremes (a 2-D monolayer and a thick multilayer) would be consistent with the opposition brightening and the tilt-angle behavior. Dynamical models also differ from the previously studied multilayer models in having a vertically non-uniform density profile.

We have recently developed a new photometric code for calculation of scattering properties of arbitrary particle fields, with no restrictions on volume density. Especially, the method can be directly applied to calculate the photometric properties of the non-uniform particle distributions predicted by self-gravitating dynamical simulations, which was the main motivation behind its development. The method is based on Monte Carlo ray-tracing, combining the advantages of both the direct and indirect methods (forward from the light source and backward from the viewing point, respectively), which makes it possible to treat  $10^4 - 10^5$  simulation particles with a very small statistical uncertainty of the results. Preliminary application to the azimuthal brightness asymmetry has already been reported (Salo and Karjalainen 1999; Salo et al. 2000; French et al.

2000), demonstrating the viability of dynamical wakes as a cause of the observed asymmetry. Similar suggestion has been recently made by (Porco et al. 2001). In the present manuscript we concentrate on systems which have planar homogeneity (i.e. self-gravity is not included), to check that large  $D$  dynamical models which lead to wakes in the outer parts of Saturn’s rings fulfill the basic photometric constraints set by ground-based observations.

The Monte Carlo code is described in detail in Section 2, while Section 3 tests it against previous classical calculations, and infers some general effects of non-zero volume density on singly and multiply scattered intensities. In Section 4 we show that high-filling factor ring models, suggested by dynamical simulations, are consistent with the ground-based photometric observations (opposition and tilt effects). Especially, the opposition brightening for phase angles below 1 degree can be reproduced even without an intrinsic opposition peak for particles, even for a system with large ( $D > 0.2$ ) central plane filling factor. This is the case for a very extended size distribution. We also briefly discuss the implications for some Voyager observations (high phase angle brightness, contrast reversal at resonance sites, correlation between brightness and occultation optical depth). The next paper (Salo *et al.*, in preparation, hereafter referred as paper II) is devoted to the relation between dynamical wakes and the azimuthal asymmetry as seen in the Voyager observations of transmitted and reflected light.

## 2. Photometric Monte Carlo method

We calculate the amount of light scattered by a local region of a planetary ring, represented by the ensemble of simulation particles with known positions at a given instant of time. Both singly and multiply scattered radiation are taken into account, as well as the planar periodicity assumed in the dynamical simulations. This is very important for modeling of low elevation angle observations, where a light ray can, at least in principle, travel a long horizontal distance before leaving the particle layer. Since the size of the ring particles is much larger than the wavelength of visible light, we assume geometric optics. A straightforward way to calculate the observed brightness is to use the direct Monte Carlo method, which follows the path of individual light rays emitted by the source through successive scatterings, and tabulates their final directions and intensities once they have escaped the layer of scattering particles. The Monte Carlo element comes from the use of a single emergent ray after each scattering event, chosen with the help of random numbers to represent the assumed scattering law. We will first describe this direct Monte Carlo method and then discuss how the variance of the results can be significantly reduced by a combination of direct and indirect (backward) Monte Carlo methods, the latter utilizing the fact that we are interested of the brightness in certain viewing directions only.

## 2.1. Coordinate system of dynamical simulations

Since the coordinate system used in our photometric calculations is the same as that in our dynamical experiments, we describe here briefly the basic features of these simulations. In the local method all gravitational and collisional calculations are restricted to a small region inside the rings, corotating with  $\Omega$ , the local mean angular speed of particles (Wisdom and Tremaine 1988; Toomre and Kalnajs 1991; Salo 1992a). The advantage of this method is that realistic particle sizes and ring surface densities can be studied with a manageable number of simulation particles. Also, linearized equations of motion can be utilized, employing a local Cartesian coordinate system. Due to differential rotation individual particles tend to leave the calculation region, which is taken into account in the form of periodic boundary conditions. These can be described in terms of image particles,

$$\begin{aligned} x' &= x + nL_x, \\ y' &= y + mL_y - 3/2 \, nL_x\Omega t, \\ z' &= z, \end{aligned} \tag{1}$$

where  $m$  and  $n$  are integers,  $L_x$  and  $L_y$  denote the dimensions of the actual calculation region, and  $t$  the time reckoned from the beginning of the simulation; the x-axis points in the radial direction, the y-axis in the direction of orbital motion, and the z-axis is perpendicular to the equatorial plane. Thus, each time a particle crosses the boundary, one of its images enters the calculation region and replaces the leaving particle. Especially, if the crossing occurs across the inner or outer radial boundary, the velocity of the particle is modified by  $\Delta\dot{y} = \pm 3/2 \, \Omega L_x$ , which corresponds to the difference of shear velocity across  $L_x$ . In this manner the evolution of the system is independent of the choice of the origin of the coordinate system. The results are also independent of the size of the calculation region, provided that it is large compared to the mean free path between impacts (Wisdom and Tremaine 1988; Salo 1991).

In the photometric modeling we utilize the results from dynamical simulations. In the present study, only experiments without self-gravity are used, as well as artificially created data for vertically homogeneous systems. In all cases the format of the particle data is similar, and periodic replicas of the particles in the actual calculation region are used. For the dynamical simulations with planar homogeneity studied here, the orientation of the system with respect to the direction to the planet plays no role: this, however, is important in the case of gravitational wake structures having preferential orientation with respect to the local radius vector.

**Insert here Fig. 1**

## 2.2. Direct Monte Carlo method

The simulation region is illuminated by a parallel beam of sunlight, with incident flux  $\pi F$ . The energy flux to the simulation region is

$$L = \pi F |\sin B'| L_x L_y, \quad (2)$$

where  $B'$  is the Solar elevation angle and  $L_x$  and  $L_y$  denote the dimensions of the calculation region. This energy flux is represented by  $N_{phot}$  photon packets, each with initial weight

$$W_0 = L/N_{phot} = \pi F |\sin B'| L_x L_y / N_{phot}. \quad (3)$$

The coordinate system we use is the same local Cartesian system as in the dynamical simulations themselves (see Fig. 1). The path of the photon packet inside the layer of ring particles consists of line segments between successive scatterings. Denote by  $\vec{p} = \{p_x, p_y, p_z\}$  and  $\hat{e} = \{e_x, e_y, e_z\}$  the instantaneous position and direction of the photon packet, and by  $\vec{R}_i = \{x_i, y_i, z_i\}$ ,  $i = 1, \dots, N$  the positions of particles, assumed spherical, with radii  $s_i$ . The intersection of the photon path with the surface of particle  $i$  corresponds to a real root  $t_i$  for the equation

$$(\vec{p} + t_i \hat{e} - \vec{R}_i)^2 = s_i^2, \quad (4)$$

$t_i$  giving the distance along the present photon path to the intersection. The position of the next scattering point is then chosen as

$$\vec{p}' = \vec{p} + t \hat{e} \quad (5)$$

where  $t = \min\{t_i > 0; t_i \text{ real}\}$ . If Eq. (4) has no real roots for any  $i$ , the photon packet is able to escape from the original calculation region. This, however, does not mean that it will escape from the ring, as the packet may intersect one of the image particles, which have positions according to Eq. 1. To search for these intersections, the photon packet is moved to the edge of the original calculation region along its current path, and the above procedure is repeated with the image particles in the region where the packet arrives. In practice it is more convenient to replace the photon with an image photon, entering the original calculation box from an appropriately modified position (thus avoiding the need for storing separately the positions of image particles). Altogether, the search for possible intersections is repeated until a new target particle is found, or until the photon position is such that no intersection will be possible. This is the case if either

$$p_z > \max\{z_i + s_i\} \quad \text{and} \quad e_z \geq 0, \quad (6)$$

or

$$p_z < \min\{z_i - s_i\} \quad \text{and} \quad e_z \leq 0. \quad (7)$$

Formally, we also set a upper limit of 1000 for the maximum number of image regions checked, but this limit is in practice never reached. In the case of escape, the final direction and weight of the photon packet are stored.

When a photon packet intersects a particle surface, its direction is modified according to the surface element's reflection law  $S$ , and its weight is reduced by the surface albedo  $A$ . The reflection function is defined so that  $AS(\mu, \phi, \mu_0, \phi_0)d\mu d\phi$  gives the probability that a photon arriving at the surface from the direction  $(\mu_0, \phi_0)$  will scatter to an interval  $d\mu, d\phi$  about the direction  $(\mu, \phi)$ . Here  $\mu_0 = \cos(i)$  and  $\mu = \cos(\epsilon)$ , where  $i$  and  $\epsilon$  denote the angles of incident and emergent rays with respect to the normal vector  $\hat{n}$  of the surface element at the intersection point, while  $\phi_0$  and  $\phi$  are the azimuthal directions in a coordinate system where the polar direction is along  $\hat{n}$ . For most of our simulations we have assumed Lambert scattering, in which case  $S \equiv S_L(\mu, \mu_0) = \mu/\pi$ .

In the case  $S$  is independent of the azimuth of scattering (as is the case for  $S_L$ ), the new photon direction is obtained by

$$\phi' = 2\pi r_1, \quad (8)$$

where  $r_1$  is a uniformly distributed random number between 0 and 1,  $r_1 = RND(0, 1)$ . The new polar direction is obtained by setting

$$\frac{\int_1^{\mu'} S d\mu}{\int_1^0 S d\mu} = r_2 = RND(0, 1), \quad (9)$$

and solving for  $\mu'$ . In the case of Lambert's law this implies  $\cos(\epsilon') = \mu' = \sqrt{r_2}$ . The new photon direction in the simulation coordinate system,  $\hat{e}'$ , is then obtained by (Salo 1988) (if  $n_z^2 \neq 1$ )

$$\begin{aligned} e_z' &= n_z \cos \epsilon' + \sin \epsilon' \cos \phi' \sqrt{1 - n_z^2}, \\ e_x' &= \frac{1}{1 - n_z^2} [n_x (\cos \epsilon' - n_z e_z') - \sin \epsilon' \sin \phi' n_y \sqrt{1 - n_z^2}], \\ e_y' &= \frac{1}{1 - n_z^2} [n_y (\cos \epsilon' - n_z e_z') + \sin \epsilon' \sin \phi' n_x \sqrt{1 - n_z^2}]. \end{aligned} \quad (10)$$

If  $n_z^2 = 1$ , then

$$\begin{aligned} e_z' &= n_z \cos \epsilon', \\ e_x' &= \sin \epsilon' \cos \phi', \\ e_y' &= \sin \epsilon' \sin \phi'. \end{aligned} \quad (11)$$

At the scattering event the weight of the photon packet is reduced by  $A$ , and a new line segment is calculated, until the packet escapes, or a pre-assigned maximum number of scatterings (typically 100) has taken place.

In order to convert the photon weights to observed intensities, we assume that the escaping photon packets are registered at a distance  $\Delta$  from the simulation system, in a direction corresponding to the elevation angle  $B$  and azimuthal angle  $\theta$ , counted with respect to the simulation  $x$ -axis. The area of registration is  $dA = \cos B dB d\theta \Delta^2$  and the total flux arriving at  $dA$  is

$\sum_{m=1}^{N_{phot}} W_m(B, \theta)$ , where  $W_m$  denotes the weight escaping toward  $dA$  due to the  $m'$ th photon (most of these are typically zero). The intensity  $I(B, \theta)$  is then obtained by dividing the energy flux by  $dA$  and by the solid angle of the illuminating ring patch as seen from the registration area,  $\omega_s = \frac{L_x L_y |\sin B|}{\Delta^2}$ , yielding

$$I(B, \theta)_{dir} = \frac{\sum_{m=1}^{N_{phot}} W_m(B, \theta)}{L_x L_y |\sin B| \cos B dB d\theta} \quad (12)$$

The subscript 'dir' is used to distinguish this from the intensity calculated below with the indirect method. Taking into account Eq. 3, and normalizing with the incident solar flux, we obtain

$$\frac{I(B, \theta)_{dir}}{F} = \frac{\pi |\sin B'|}{|\sin B| \cos B dB d\theta} \frac{\sum_{m=1}^{N_{phot}} W_m(B, \theta)/W_0}{N_{phot}}. \quad (13)$$

Since  $I/F$  is proportional to an average  $\langle W'_m \rangle$  over the photon packets ( $W'_m \equiv W_m/W_0$ ), its variance can be estimated from

$$\delta^2 \left( \frac{I_{dir}}{F} \right) = \left( \frac{\pi \sin B'}{\sin B \cos B dB d\theta} \right)^2 \frac{\langle W_m'^2 \rangle - \langle W'_m \rangle^2}{N_{phot}}. \quad (14)$$

The implied uncertainty  $\Delta(I/F) \approx \sqrt{\delta^2(I/F)}$  is fairly large. For example, assume that most of the intensity is due to single scatterings, and that the number of photons reaching the registration area is  $N(B, \theta) = p(B, \theta)N_{phot}$ . Then the weight carried to the registration area is either  $AW_0$  or 0, and  $\langle W_m'^2 \rangle \approx pA^2$  and  $\langle W'_m \rangle \approx pA$ , and the fractional error

$$\frac{\Delta(I/F)_{dir}}{(I/F)_{dir}} \approx \sqrt{\frac{(1-p)}{pN_{phot}}}. \quad (15)$$

As  $p$  is small,  $1-p \approx 1$  and the fractional error  $\approx N(B, \theta)^{-\frac{1}{2}}$ , as expected for a direct Monte Carlo estimate.

### 2.3. Backward Monte Carlo method (Indirect method)

The above described direct method, although very easy to implement and test, has the disadvantage that only a small fraction of all photon packets contributes to the brightness in a given direction we are interested in, leading to a large variance of the result. In fact, this variance is large enough to make the direct method unsuitable for practical use (see Section 3). The efficiency can be significantly improved by a combination with a backward Monte Carlo method, sampling the brightness as seen from a pre-specified viewing direction or directions. The path of the photon packet from one intersection to the next is calculated as in the direct method, but additionally, in



each scattering event we now check whether the illuminated point is visible from the given observing direction  $(B, \theta)$  : not hidden by the particle itself, or by any other particle or image particle. This check can be done with the same method that is used in the above described search of photon-particle intersections. If no intervening particles are found, then this illuminated point contributes to the intensity in the registration direction by the amount

$$I_{km}(B, \theta) = \frac{W_{km} A S_{km}}{|\sin B| L_x L_y}, \quad (16)$$

where  $S_{km} = S(\mu_o, \mu')$ ,  $\mu' = \hat{n}_k \cdot \hat{o}$ , with  $\hat{o} = \{\cos B \cos \theta, \cos B \sin \theta, \sin B\}$  specifying the registration direction, and  $W_{km}$  is the weight before the  $k'$ th scattering of the  $m'$ th photon packet. After this the photon path is continued toward the next scattering as before. The total intensity  $I(B, \theta)_{indir}$  is obtained by summing over the different scatterings of  $N_{phot}$  photon packets, which after normalization yields

$$\frac{I(B, \theta)_{indir}}{F} = \frac{\pi |\sin B'|}{|\sin B|} \frac{\sum_{m=1}^{N_{phot}} \sum_k (W_{km}(B, \theta)/W_0) A S_{km}}{N_{phot}}. \quad (17)$$

The variance of the result can be estimated in a similar fashion as for the direct method,

$$\delta^2 \left( \frac{I_{indir}}{F} \right) = \left( \frac{\pi \sin B'}{\sin B} \right)^2 \frac{\langle W_m'^2 \rangle - \langle W_m' \rangle^2}{N_{phot}}, \quad (18)$$

where  $W_m'$  now denotes  $\sum_k (W_{km}/W_0) A S_{km}$ .

A considerable reduction in the total CPU time is achieved for a desired accuracy, as now in principle every photon intersection with a particle can contribute to the brightness in a given direction, instead of only those photons actually escaping to this direction. As an idealized example consider again a case where single scattering dominates, and for simplicity assume that the scattering is isotropic (and neglect all shadowing), so that  $S_{1m} = \frac{1}{4\pi}$ . If the total fraction of photons scattered to any direction is  $p_T$ , then each of the scattered  $p_T N_{phot}$  photons yields  $W_m' = \frac{A}{4\pi}$ . Proceeding as before, the fractional error becomes

$$\frac{\Delta(I/F)_{indir}}{(I/F)_{indir}} \approx \sqrt{\frac{(1 - p_T)}{p_T N_{phot}}}. \quad (19)$$

So, although the  $N_{phot}^{-1/2}$  dependence of the error is retained, its magnitude is roughly  $\left( \frac{N(B, \theta)}{N_{phot}} \right)^{\frac{1}{2}}$  times smaller than the error in the direct method. Also in a more realistic case with non-isotropic phase function and multiple scattering the efficiency is significantly improved, as shown by the examples studied below.

## 2.4. Different surface albedo values

Both direct and indirect methods provide an easy way to look separately at singly scattered and higher order contributions, by storing information of how many times a photon has scattered before the escape (direct method) or before it contributes to the intensity in a given direction (indirect method). This also makes it possible to obtain the brightness for any surface albedo from a single run: by choosing  $A = 1$  in the run and by denoting with  $\Delta I_k$  the intensity due to scattering by  $k$  times, we have the total scattered intensity for surface albedo  $A_0$

$$I_{tot} = \sum_1^{max} A_0^k \Delta I_k. \quad (20)$$

## 2.5. Spatial partitioning

The most time consuming part of the above calculations is the search of intersections between a photon packet and particles. This time consumption can be reduced by limiting the number of particles for which the intersection is checked for. We use a simple 2D spatial partitioning, where a rectangular  $M_x \times M_y$  mesh is superposed over the particle field, and store a list of particle indices belonging to each cell, as well as the maximum distance from the cell center  $\vec{p}_c$ , up to which its particles can cause intersections,

$$d_{max}^2 = \left(\frac{L_x}{M_x} + s_{max}\right)^2 + \left(\frac{L_y}{M_y} + s_{max}\right)^2, \quad (21)$$

where  $s_{max}$  is the maximum particle radius in the cell. Before looking for the actual particle intersections, the minimum distance of each cell center from the photon path is calculated,

$$d_c^2 = (\vec{p}_c - \vec{p})^2 - [(\vec{p}_c - \vec{p}) \cdot \hat{e}]^2, \quad (22)$$

and only those particles which belong to a cell that can in principle intersect the current path,  $d_c < d_{max}$ , are actually checked. This simple trick effectively replaces the  $N$  (particle number) dependence of the intersection search with  $N^{1/2}$ , and since the particle positions are fixed, these lists need to be constructed only once during a run, causing very small overhead CPU time-consumption. Typically, a subdivision to about 20 by 20 cells provided an optimal speedup for  $N \approx 10^4$  simulation particles, reducing the time required for the search of intersection to about 10% of that which would be needed without partitioning. Also 3D partitioning was checked but this did not yield any additional speedup. Namely, even in the 2D partitioning we can easily discard sub-cells for which the distance of the photon packet from the central plane is already too large for intersections. Examples of CPU-time consumption are given in caption of Fig. 7.

## 2.6. Saturn-shine

The brightness due to the illumination by Saturn is calculated in a similar manner as that due to the Sun. The only difference is that the directions of the incoming photons are sampled from the solid angle extended by Saturn’s ball, as viewed from the ring patch. In practice the ball of Saturn is divided into latitude and longitude surface elements, for each of which it is tested whether it is illuminated by the Sun, and whether it is visible from the ring (Price and Baker 1975). The brightness of each point of Saturn is calculated from Barkstrom’s law (Barkstrom 1973),

$$\frac{I_{sat}}{F} = \frac{k_1}{\mu} \left( \frac{\mu\mu_0}{\mu + \mu_0} \right)^{k_2} \quad (23)$$

where  $\mu_0$  and  $\mu$  here denote the direction cosines of the incident and emergent radiation on Saturn’s surface, and  $k_1$  and  $k_2$  are numerical factors depending on the phase angle between the incident and emergent rays, interpolated from the values tabulated in Table V in Dones et al. (1993). The number of photons shot from each Saturn’s surface element is proportional to the energy flux reaching the ring patch. Final results are normalized to F, as for the scattering due to direct solar illumination. In the treatment of Saturn-shine we approximate the planet to be spherical, whereas Dones et al. (1993) take also into account its oblateness.

## 2.7. Spherical particle phase-functions

Most of our simulations employ Lambert’s scattering law for each ring particle’s *surface element*. However, in order to compare with various results in earlier literature, other scattering laws were also implemented, defined in terms of the distribution of scattering from the *spherical particle* as a whole. The difference is that the scattering probability is now defined solely in terms of the phase angle  $\alpha$ , the difference between the directions of the incoming and outgoing rays, as seen from the scattering point. Especially, we use the Henyey-Greenstein phase function

$$P_{HG}(\alpha) = \frac{1 - g^2}{(1 + g^2 + 2g \cos \alpha)^{\frac{3}{2}}} \quad (24)$$

where  $g$  is the anisotropy parameter,

$$g = - \langle \cos \alpha \rangle = - \frac{1}{2} \int_0^\pi P(\alpha) \cos \alpha \sin \alpha d\alpha, \quad (25)$$

varying between  $g = -1$  (perfect back scatterer) and  $g = 1$  (perfect forward scatterer). Also, we employ the combination of two Henyey-Greenstein functions, used in Esposito and Lumme (1977) and Lumme et al. (1983),

$$P(\alpha) = bP_{HG}(\alpha, g_1) + (1 - b)P_{HG}(\alpha, g_2), \quad (26)$$

and the power-law phase function

$$P_{power}(\alpha) = c_n(\pi - \alpha)^n \quad (27)$$

defined in Dones et al. (1993). In all cases the phase function is normalized so that the integral over all solid angles  $\int P(\alpha) 2\pi \sin \alpha d\alpha = 4\pi$ . For Eq. 27 the normalization factors  $c_n$  and the anisotropy parameters  $g$  corresponding to various exponents  $n$  are given in Table IV in Dones *et al* (1993).

Some modifications are required when spherical particle phase functions are used instead of the surface element's reflection law. In choosing the direction of the photon after scattering, Eqs. 8 - 11 are employed, with  $P(\alpha)/4\pi$  now replacing  $S(\mu)$ , and  $\hat{n}$  now standing for the direction of the incoming photon (as seen from the particle), not for the surface element's normal direction. When using the spherical phase function, the information of where the scattering takes place on the particle surface is not defined, so that there is an ambiguity about where to start the emerging photon packet. We experimented with two ways of choosing the post-scattering starting point, either from the particle center or from the intersection point of the incoming photon. Although the former choice would be more in accordance with the concept of the spherical particle phase function, the latter choice seemed to give more realistic results. Namely, as described below in more detail, we carried out comparisons for the Lambert scattering, using both the surface element's reflection law, and the corresponding spherical-particle phase function

$$P_L(\alpha) = \frac{8}{3\pi}[\sin \alpha + (\pi - \alpha) \cos \alpha], \quad (28)$$

in which case it is possible to check the error introduced.

### 3. Preliminary tests and the influence of non-zero volume density

In order to test the correctness of the Monte Carlo method several checks are carried out. First of all, the results of the indirect method are checked against the direct method, and the error estimates given in the previous section are verified. Secondly, the Monte Carlo results are tested against the classical calculations in the limit of vanishing volume filling factor  $D$ , both with comparisons to analytic results for isotropic scattering calculated in terms of Chandrasekhar's X and Y-functions, and with comparisons to Dones et al. (1993) in the case of power-law phase function. Besides these tests, this section highlights the modifications caused in the overall scattering behavior by a non-zero  $D$ .

### 3.1. Particle distributions

In this study two types of particle fields are studied:

- 1) vertically homogeneous systems of identical particles, created by uniformly distributed, non-overlapping particles, and
- 2) particle fields obtained from dynamical simulations, both with identical particles and with a size distribution.

In most of the preliminary comparisons, homogeneous particle fields are employed, realized with  $N \sim 10^4$  particles uniformly distributed within the calculation region, with the condition that no overlaps are allowed between particles, nor with their replicas extending over the periodic boundaries. The optical depths are specified in terms of the dynamical optical depth

$$\tau_{dyn} = (\sum_i \pi s_i^2) / (L_x L_y), \quad (29)$$

the total surface area of particles divided by the area of the calculation region, which is the basic quantity employed in dynamical experiments. Different values of the volume filling factor  $D$  correspond to different physical thicknesses  $H$  of the particle layer<sup>1</sup>. For a homogeneous layer of identical particles  $D \equiv D_{uni} = \frac{4s}{3H} \tau_{dyn}$ , where  $s$  is the radius of the particles. In practice, systems with  $D$  up to 0.3 can be easily constructed with the random placement of non-overlapping particles.

For the particle fields taken from dynamical simulations the vertical profile is always non-uniform, being determined by the balance between the collisional dissipation of random kinetic energy and the viscous gain of energy from the systematic velocity field. No self-gravity is included in order to assure the homogeneity in planar directions. In dynamical simulations the velocity change in impacts is determined by the normal coefficient of restitution  $\epsilon_n$ , describing the ratio of the post- and precollisional relative velocity components in the direction joining the particle centers. For the  $\epsilon_n$  we use the standard velocity-dependent elasticity model of Bridges et al. (1984),

$$\epsilon_n(v_n) = \min[(v_n/v_c)^{-0.234}, 1], \quad (30)$$

where  $v_n$  is the normal component of the relative velocity of the impacting bodies and the scale parameter  $v_c$  equals  $v_B = 0.0077 \text{ cm/s}$  in Bridges *et al.*'s measurements. In some experiments other elasticity laws are briefly examined. The simulations are performed for the Saturnocentric distance  $a = 100,000 \text{ km}$ , with  $\Omega = 1.94 \cdot 10^{-4} \text{ s}^{-1}$ . The particle size distribution is assumed to follow the power law

$$dN/ds \propto s^{-q}, \quad s_{min} < s < s_{max}, \quad q = 3, \quad (31)$$

with the upper size limit fixed to  $s_{max} = 5 \text{ meters}$ . According to Voyager radio science experiments (Marouf et al. 1983) this type of law describes the size distribution in Saturn's rings, with a lower

---

<sup>1</sup>Actually,  $H$  denotes the thickness of the layer occupied by the particle centers, so that some particles extend even outside  $H/2$  from the central plane

size limit of  $\sim 1$  cm. However, due to computational restrictions on the number of particles, we have to use a larger truncation radius: in most of our size distribution experiments  $s_{min} = 0.1$   $m$  is used. As a special case also simulations with identical 5 meter particles are reported. With a particle size distribution the volume density profile depends on the relative vertical distributions of the different sized particles. In general, the velocity dispersion and thus also the vertical scale height of the smaller particles exceeds that of the largest ones, although the system is still far from energy equipartition (Salo 1992b). Some illustrative examples of the studied particle distributions are given in Fig. 2, while Tables 1 and 2 list the models used. In all dynamical experiments the system is evolved for at least 20 orbital periods before a snapshot for photometric simulation is chosen, to assure the attainment of a local steady-state particle distribution. However, as a single snapshot is used from each simulation, some random noise is inevitably present, as seen, for example, from the scatter in the effective vertical thickness values listed in Tables 1 and 2.

**Insert here Fig. 2**

**Insert here Table 1**

**Insert here Table 2**

For comparison with previous literature, monolayer particle distributions are also briefly studied. In the 2D case the method of random placement of particles becomes inefficient already for a rather low  $\tau_{dyn}$ , as overlaps are difficult to handle. Instead of using lattice-based assignment, we chose to create monolayer models also with dynamical simulations. Even if there are overlaps in the initial distribution, the force method we use for impacts (Salo 1995) rapidly leads to a steady-state with no overlaps between particles. A practical detail worth mentioning is that since dense 2D-systems are very prone to axisymmetric overstability (Salo 2001) already for  $\tau_{dyn} \sim 0.3$ , the radial size of the calculation region in these 2-dimensional simulations needs then to be small (say,  $L_x/s < 50$ ) to suppress overstability and to assure the homogeneity of the monolayer model in the radial direction.

### 3.2. Dynamical vs. photometric optical thickness

In the case of a vertically thick multilayer, with  $D \rightarrow 0$ ,  $\tau_{dyn}$  defined in Eq. 29 equals the normal photometric optical depth  $\tau_{phot}$ , defined by the probability  $f = \exp(-\tau_{phot})$  for a perpendicular light ray to pass through the layer without being intercepted. In a case of a slanted path with  $\mu_s = \sin B_s$  the probability is  $\exp(-\tau_s)$ , where  $\tau_s = \tau_{phot}/\mu_s$ . However, with a finite thickness layer,  $\tau_{phot}$  generally exceeds  $\tau_{dyn}$ , as illustrated in Fig. 3 for vertically homogeneous systems. The case of a strict monolayer ( $H/s = 0$ ) is also shown, in which case the maximal  $\tau_{dyn} = \pi/\sqrt{12} \approx 0.907$ , corresponding to  $\tau_{phot} \approx 2.374$  (Hämeen-Anttila and Vaaraniemi 1975). In general, for the studied

range  $D \leq 0.3, \tau \leq 2$ , the photometric  $\tau$  is enhanced by

$$\tau_{phot}/\tau_{dyn} \approx 1 + kD, \quad \text{with } k = 1 - 1.5. \quad (32)$$

This is in good agreement with the enhancement factor of  $1/(1 - D)$  suggested by Esposito (1979). The same type of dependence for  $\tau_{phot}/\tau_{dyn}$  holds also in the case of a vertical distribution of identical particles, provided that  $D$  is identified with the central plane volume density  $D(0)$ ; however, in the case of a size distribution  $\tau_{phot}/\tau_{dyn}$  is closer to unity, the difference between  $\tau_{phot}$  and  $\tau_{dyn}$  decreasing with increasing  $s_{max}/s_{min}$  (see Tables 1 and 2). For example, if  $s_{min} = 0.1$  then  $k \approx 0.7 - 1.0$  for  $\tau_{dyn} = 0.5 - 2.0$ .

**Insert here Fig. 3**

In the case of a monolayer, the dependence  $\tau_s = \tau_{phot}/\mu_s$  is not valid, the actual attenuation increasing more rapidly with decreasing  $\mu_s$ , as noted in Hämeen-Anttila and Vaaraniemi (1975). In fact, the effect is even stronger than suggested by Eqs. 17-18 in Hämeen-Anttila and Vaaraniemi (1975): for example  $\tau_{phot}(B_s = 90^\circ) = 1$  actually corresponds to  $\tau_{phot}(B_s = 26^\circ) \approx 1.3$ , whereas their Table I gives 1.08. However, with increased layer thickness this  $B_s$  dependence becomes insignificant: already for  $H/s = 6$  the normal photometric optical depths derived from  $B_s = 90^\circ$  and  $B_s = 26^\circ$  agree within a few percent for  $\tau_{dyn} < 2$  (Fig. 3). For even smaller  $B_s$  larger differences might be possible, but this was not studied in the present work as due to a very small penetration probability a very large  $N_{phot}$  would be required.

In what follows we drop the subscript from  $\tau_{phot}$  but retain its use in  $\tau_{dyn}$  whenever the distinction is significant ( $D > 0$ ).

### 3.3. Indirect vs. Direct Monte Carlo Method

**Insert here Fig. 4**

Figure 4 compares the angular distribution of scattering obtained with direct and indirect MC methods. Different orders of scattering up to 5 are displayed, for a normally illuminated uniform layer of Lambert-particles with dynamical optical depth  $\tau_{dyn} = 0.5$ . Altogether  $10^7$  photons were shot at a particle field composed of 10 000 particles, with  $D = 10^{-3}$ . The normal illumination was chosen in order to reduce the scatter in the direct method, as then the average over azimuth can be taken in obtaining the brightness in various latitude bins. The  $I/F$  values with the indirect method were obtained from the same run, for 30 pre-chosen viewing directions. Altogether, the agreement is excellent in both the reflected ( $B > 0^\circ$ ) and transmitted light ( $B < 0^\circ$ ), for all studied orders of scattering. Note the larger scatter in the  $(I/F)_{dir}$  values even with the summing over azimuths. In the case of an arbitrary illumination direction, the azimuthal bin-size would need to be comparable to the latitude bin-size (in this case  $2^\circ$ ), meaning that the scatter of results would increase by a typical factor of  $(360^\circ/2^\circ)^{\frac{1}{2}} \approx 10$ . On the other hand, the obtained  $(I/F)_{indir}$  would

be practically indistinguishable from that in the figure already for  $N_{phot} \sim 10^5$ .

**Insert here Fig. 5**

The large reduction of uncertainty obtained with the indirect method is further illustrated in Fig. 5, for  $B' = 45^\circ$  illumination angle, and  $10^\circ \times 10^\circ$  collection bins in the direct method. Fig. 5 also confirms the validity of the statistical error estimates given by Eqs. 14 and 18, by comparing them with the standard deviation of  $I/F$  obtained in ten separate runs with different seeds for the random number generator. The increased relative error for small  $|B|$  results from the small number of photons escaping to low elevation angles (direct method) or being able to contribute to the flux in the registration direction (indirect method). The increased fractional error for small  $B$  indicates that in the applications to ground-based photometry of Saturn's rings, a typical number of  $> 10^5$  photons is needed to assure a relative accuracy better than about 1% for  $B \sim 6^\circ$ , even with the indirect method. On the other hand, in order to get a sufficient resolution for comparison with observation, the bin-size in the direct method should be even smaller than adopted here (say, at most  $1^\circ \times 1^\circ$ ), making the required number of photons excessively large ( $\sim 10^8$ ) for a similar accuracy. Therefore from here on all Monte Carlo calculations are carried out with the indirect method.

Besides including a sufficient number of photons, additional caution is needed in calculation of viewing or illumination angles near zero, due to the long slanted paths through system. For a homogeneous square-shaped region of identical particles,  $H/L_x = \frac{4}{3\sqrt{\pi}D}\tau_{dyn}^{1.5}N^{-0.5}$ . For example, the total vertical thickness of the particle field in Fig. 4 corresponds to  $H/s = 670$ , while even with  $N = 10^4$  particles its extent in the horizontal direction is only  $L_x/s = 250$ . In order to assure that a path with, say  $|B| = 6^\circ$  is completely covered,  $N_{box} = H/(L_x \tan B) \approx 25$  replicas of the actual simulation box are needed in every direction. Otherwise, in the direct method a photon can escape (or enter, if  $B' < 90^\circ$ ) the system through the vertical borders, or a contribution of scattering can be registered before it is certain that no intervening particles would be found (in the indirect method). The use of too few replicas of the actual region will lead in all cases to an artificial brightening. For example, in the case of Fig. 4 the use of  $N_{box} = 5$  or 10 replicas would yield an erroneously enhanced  $I_{ss}$ , by factors of 2 and 1.3, respectively, for  $B = 6^\circ$ . However, since in practice only a very small fraction of photons will ever travel through several replicas, elimination of this problem with the inclusion of an appropriate number of particle replicas is not very CPU-time consuming. In this respect the formulation in terms of image photons instead of image particles (see Section 2) is very useful, as there is no need to store any huge number of image particle positions.

Additional tests with different numbers of particles in the actual simulation region indicate that the results are not sensitive to  $N$  for the used particle fields with  $N > 10^3 - 10^4$ . For small  $N$  the discreteness of the particle field may become evident in some cases, especially for small  $B$  and  $B'$ , as the scattering will then depend strongly on the few outermost particles on the illuminated side of the system. The problem is also most pronounced in the case of size distribution, as the number of largest particles is necessarily fairly small for the used power-law. However, in the present



case of systems with planar homogeneity, the effect of discreteness can be significantly reduced by rotating the particle field randomly between each new photon path (in practice, the illumination and viewing azimuths are rotated). This procedure is applied in most of the subsequent plots.

A final point to consider is the accuracy of the search of photon path -particle intersections: for small  $D$  the distances traveled between intersections can be large compared to particle dimensions. Therefore double precision is used in this search. This is especially important when using the surface elements' reflection law, where the distribution of intersection points needs to be accurately sampled on the particle surfaces.

### 3.4. The effect of non-zero volume density

In the classical  $D \rightarrow 0$  case, when the particles are separated by large distances as compared to their size (so that the far-field approximation is valid), the single scattering components of the reflected and transmitted radiation are given by (van de Hulst 1980)

$$\begin{aligned} \left(\frac{I_{ss}}{F}\right)_{refl} &= \frac{AP(\alpha)\mu_0}{4(\mu + \mu_0)} (1 - \exp[-\tau(1/\mu + 1/\mu_0)]) , \\ \left(\frac{I_{ss}}{F}\right)_{trans} &= \frac{AP(\alpha)\mu_0}{4(\mu - \mu_0)} (\exp[-\tau/\mu] - \exp[-\tau/\mu_0]) , \quad (\mu \neq \mu_0) \\ &= \frac{AP(\alpha)\tau}{4\mu_0} \exp[-\tau/\mu_0], \quad (\mu = \mu_0) \end{aligned} \quad (33)$$

Here the factor  $\tau_{path} = \tau(1/\mu + 1/\mu_0)$  represents the total optical path of a reflected ray, with  $\mu_0 = |\sin B'|$  and  $\mu = |\sin B|$ . These theoretical curves for single scattering were also displayed in Fig. 4. Clearly the studied value  $D = 0.001$  is small enough to approximate well the classical limit. The only differences are seen near  $B = B' = 90^\circ$ , where the simulated single scattered flux exceeds the theoretical one: this is due to the well-known opposition brightening, addressed in detail in the next section.

**Insert here Fig. 6**

In the case of larger  $D$  other differences appear (Fig. 6), the reflected overall intensity increasing with  $D$ . This is due to enhanced singly scattered flux and is most pronounced near  $B = 0^\circ$ . Similarly, transmitted singly scattered radiation is strongly reduced near  $B = 0^\circ$ . This behavior is not accounted for by the enhanced  $\tau/\tau_{dyn}$  studied in Fig. 3, which has only a small influence for  $\tau \sim 1$ . Rather, the behavior at low viewing angles follows from the fact that only certain portions of the finite sized particles are visible. For example, when the system is viewed from the sunlit side at a very low elevation angle, mainly the illuminated upper surfaces of the outermost particles are seen, enhancing the reflection. Similarly, when viewed from the opposite side, particle

hemispheres predominantly in the shadow are visible. Since the total geometric thickness decreases with increasing  $D$  ( $H/s = 4/3 \tau_{dyn}/D$ ), this contribution of outermost particle layers increases with  $D$ . The increase near  $B = 90^\circ$  corresponds to the opposition brightening which extends to a larger angular region when  $D$  is increased. In contrast to single scattering, the multiply scattered flux is less affected, being reduced near  $B = 0^\circ$ , both for reflected and transmitted radiation. Other experiments with  $\tau \leq 2$  also indicate that the typical brightening in the reflected radiation depends rather weakly on  $\tau$ . Altogether, the fractional increase in the singly scattered reflected radiation for  $\tau \sim 1$  amounts (at intermediate elevations outside the opposition peak region) to about

$$\frac{I_{ss}(D)}{I_{ss}(D=0)} \approx 1 + 2D \quad \text{for } B' = 90^\circ, \quad (34)$$

in the studied case of a homogeneous system composed of equal-sized particles. This agrees well with the study of Peltoniemi and Lumme (1992) who found about 50% increase in the brightness of a normally illuminated layer of rough particles when  $D$  was changed from 0.1 to 0.4.

Insert here Fig. 7

The studied case of exactly perpendicular illumination is naturally a very special one. However, a qualitatively similar overall enhancement of reflected  $I_{ss}$  is seen also in the case of slanted illumination (see Fig. 7), except that the brightening seen near  $B = 0^\circ$  in Fig. 6 is now more prominent on the viewing azimuths opposite to illumination,  $\phi - \phi' \sim 180^\circ$ , corresponding to large phase-angle. Also, as  $B'$  decreases, the reduction of  $I_{ms}$  seen near  $B = 0^\circ$  in Fig. 6 becomes more pronounced. Since the large  $\alpha$  reflection is dominated by multiply scattering (for the studied backscattering Lambert case with  $A=0.5$ ), the total effect of large  $D$  is to reduce the large phase angle brightness for small  $B$ 's. At the same time the low  $\alpha$  brightness remains enhanced, due to opposition brightening of singly scattered component. Further, more realistic examples of low elevation angle results are shown in the next sections, where the calculations are compared to ground-based and Voyager observations.

Insert here Fig. 8

It is also of interest to check whether allowing for a non-uniform vertical density profile and particle size distribution will affect the brightening due to non-zero volume density. For these comparisons dynamical simulation data are used. In principle, it may be expected that when taking into account the vertical distribution, the system will have a smaller effective  $D$  when viewed with low  $B$  as compared to larger elevations, when the densest inner parts are better visible. However, when limiting to identical particles, the effect of the vertical profile turns out to be rather weak, reducing somewhat the brightness increase near  $B = 0^\circ$  in Fig. 6. On the other hand, when a particle size distribution is also taken into account the situation changes significantly (Fig. 8). As mentioned above, in dynamical simulations the smaller particles typically occupy a thicker vertical layer than the largest ones, corresponding to several times the diameter of the largest particles (see

Fig. 9, upper frame, and Table 1). This partial segregation of particle sizes increases the vertical gradient of the volume density. Also, the ‘envelope’ formed by the small particles will effectively help to hide the inner dense portions of the system. The effect of particle size distribution on the brightness for  $B' = 90^\circ$  is studied in Fig. 8, for different widths of a power-law distribution. As the distribution is extended to smaller and smaller sizes, the brightness peak near  $B = 0^\circ$  seen in the case of homogeneous systems gradually disappears. Also the overall brightening as compared to  $D = 0$  is reduced, and the opposition peak gets increasingly narrow. However, even for the largest size range studied,  $s_{max}/s_{min} = 100$ , the overall intensity stays significantly higher than it would be in the case of a thick multilayer with the same  $\tau$  (approximated by the  $D_{uni} = 0.001$  case in Fig. 8)

**Insert here Fig. 9**

The lower frame in Fig. 9 illustrates the qualitative reason for the elevation angle dependence, by showing the relation between the local volume density  $D(z = z_0)$  and the cumulative optical depth  $\tau(z > z_0)$  when the system is traversed from  $z_0 = \infty \rightarrow -\infty$ . Esposito’s formula  $\tau_{phot}/\tau_{dyn} = (1 - D(z))^{-1}$  was used in construction of  $\tau(z > z_0)$  (see the figure caption). For example, with a  $B = 6^\circ$  viewing elevation  $\tau/\sin B$  attains unity already for a layer where  $D \approx 0.03$  when the size distribution extends from 0.1 to 5 meters, while in the case of identical particles, the same optical depth would be attained in a layer with  $D \approx 0.1$ . Consequently the photometric behavior of the system with a size distribution can be expected to resemble that of a much smaller effective  $D$  for a system of identical particles, although they have practically the same dynamical  $D$  (the filling factors at the central plane are in the range  $0.33 \rightarrow 0.25$ , for  $s_{max}/s_{min} = 1 \rightarrow 50$ ). This modification in the effective photometric behavior in the case of size distribution will have importance when ground-based and Voyager observations are interpreted in Section 4.

### 3.5. Spherical-particle scattering laws

All the above calculations have been performed assuming Lambert’s law for surface element’s reflection law, providing in itself a useful first approximation for the photometric behavior of predominantly back-scattering ring particles (anisotropy parameter  $g = -\frac{4}{9}$  for Lambert-spheres). However, to be able to model more general photometric behavior, and to be able to compare to previous literature, other scattering laws are needed. The scattering properties of individual particles are typically specified in terms of the effective spherical-particle scattering law, which can not generally be expressed in terms of surface element’s reflection law. Nevertheless in the case of Lambert surfaces we can test the error introduced by replacing the surface element law with the corresponding Lambert-sphere phase function, Eq. 28. This is studied in Fig. 10, comparing the use of the particle center and the scattering point as the origin of the post-scattering photon path segment. In the case  $D \rightarrow 0$  both these choices yield identical results compared to using the surface element’s reflection law. However, for finite  $D$ , the use of the intersection point is clearly

a better approximation, judged by the good agreement with the exact surface element law. Even for  $D = 0.1$  the overall differences in the reflected radiation are typically less than a few percent, if the intersection point is used: largest differences are seen at  $B \rightarrow 0^\circ$  where the intersection point method overestimates the increase in reflected  $I_{ss}$ . For the same region, the particle center method fails completely to reproduce the enhanced reflected  $I_{ss}$ , as well as the attenuation of the transmitted  $I_{ss}$ . Most importantly, the opposition brightening is accurately reproduced when using the intersection point, in contrast to using particle centers, in which case it is almost absent.

The qualitative reason for the failure of the particle center method is easy to understand, remembering the dominating role of outermost particle layers in the case of geometrically thin systems. At low  $B > 0$  the centers of the uppermost particles are much more effectively shielded from viewing than their upper, illuminated hemispheres: the emerging singly scattered photon is thus more prone to be intercepted by other particles than what it would be if emerging from the scattering point, leading to a strong attenuation of reflected single scattering. Similarly, the transmitted singly scattering is increased for small  $|B|$ , as the particle centers are now more easily visible than the upper, illuminated hemispheres. No such shift of photon location is present in the intersection point method, and the opposite, much weaker trend of  $I_{ss}$  for small  $|B|$  follows from the slightly incorrect sampling of the surface elements' scattering law: for example for  $B > 0$ , too much weight is given to photons scattered near the centers of the illuminated hemispheres, as these are not so likely to be attenuated. The opposition brightening on the other hand results mainly from the nearly identical photon paths before and after the scattering: this symmetry is broken in the case of particle-center method, but is retained for the intersection point method. From here on, all experiments with non-Lambert scattering are performed with the intersection point method.

Insert here Fig. 10

As a further test of our treatment of spherical-particle phase functions we applied our method to isotropic scattering,  $P_{iso} = 1$ , in which case analytical results for the combined single and multiple scattered intensity are available in the classical limit  $D \rightarrow 0$  (Chandrasekhar 1960),

$$\begin{aligned} (I/F)_{refl} &= \frac{\mu_0}{4(\mu + \mu_0)} A[X(\mu)X(\mu_0) - Y(\mu)Y(\mu_0)], \\ (I/F)_{trans} &= \frac{\mu_0}{4(\mu - \mu_0)} A[Y(\mu)X(\mu_0) - X(\mu)Y(\mu_0)], \end{aligned} \quad (35)$$

where  $X = X(A, \tau)$  and  $Y = Y(A, \tau)$  are Chandrasekhar's functions, tabulated e.g. in Sobouti (1963) and van de Hulst (1980). From these the multiply scattered component can be separated by subtracting the single scattering contributions given by Eqs. 33. Comparisons with  $D = 10^{-3}$  indicate excellent agreement with theoretical values, while for non-zero  $D$  similar brightening in

reflected light and reduction of transmission is seen as for the Lambert-case studied in Fig. 6.

In the next section we will use the power-law scattering function introduced in Dones et al. (1993) in comparison to observations. Fig. 11 checks the results with the present MC method in comparison to those in Dones *et al.* (see their Figs 11 and 12), calculated for observing geometries in the Voyager images for small and large solar phase angles ( $\alpha = 13.2^\circ$  and  $155.3^\circ$ ). The phase function used here ( $n = 3.09$  in Eq. 27) corresponds closely to the behavior of Callisto, being more backscattering than the Lambert law ( $g = -0.55$  as compared to  $g = -0.44$ ). Besides the  $D = 0$  case studied in Dones *et al.*, the changes due to constant non-zero  $D$  are also indicated for some  $\tau$  values: see also Table 3 where the brightness changes as compared to  $D = 0$  are listed. For small phase angles single scattering dominates, and accordingly a non-zero  $D$  will lead to an enhanced brightness, which for  $D = 0.1$  amounts to about 20%. For comparison, Dones et al. (1989) report a single-scattering enhancement by 1.65 for a monolayer model, which is in good agreement with the factor 1.6 we find for a monolayer with  $\tau_{phot} = 1.0$ . On the other hand, large phase angle behavior is dominated by multiple scattering, and a non-zero  $D$  will reduce the ring brightness, by about 15 – 20% for  $D = 0.1$ . For  $\tau_{dyn} = 0.1$  even stronger reduction of  $I_{ms}$  is obtained, resulting from the almost monolayer nature implicated by  $D = 0.1$  in this case. Altogether the modifications of non-zero  $D$  found here are similar to those in Fig. 7 for a Lambert phase function. However, with an extended size distribution the increase in the low  $\alpha$  brightness is significantly reduced (see Table 3). Also, the multiply scattered contribution at high  $\alpha$  approaches the classical  $D = 0$  level as the width of the distribution increases. This low vs. high  $\alpha$  behavior is studied in more detail in Section 4.3.

**Insert here Fig. 11**

**Insert here Table 3**

Also shown in Fig. 11 are contributions from Saturn’s illumination, both from Dones et al. (1993) and from our present calculations. We also verified the correct ring longitude dependence of Saturn shine, by checking our calculations against Fig. 13 in Dones *et al.*. Saturn-shine is not considered further in the present study, concentrating on observational comparisons in cases where it plays only an insignificant role. It will be included in Paper II in the analysis of the azimuthal asymmetry for a wider range of observing geometries.

#### 4. Applications to Saturn’s rings

We next apply our MC method to the photometric behavior of Saturn’s rings. Our main goal is to check whether the moderately flattened, large volume density models predicted by dynamical simulations are consistent with the tilt effect, i.e. the brightening of the B-ring with an increasing elevation angle (Camichel 1958), and the opposition effect, i.e. the strong increase in the ring brightness for phase angles less than a few degrees (Irvine 1966; Bobrov 1970). Previous detailed

studies (Lumme and Irvine 1976; Esposito and Lumme 1977) suggest that classical multilayer models ( $D = 0$ ) can account for the tilt effect in the B-ring, as well as for its absence in the A-ring, by the larger amount of multiple scattering in the B-ring. Similarly, Lumme et al. (1983) showed that the opposition brightening is most naturally accounted for by the enhanced single scattering contribution near the zero solar phase angle, due to the reduced amount of mutual shadowing between particles. Since the angular width of the predicted opposition peak depends sensitively on the volume density, the opposition effect sets a very strong observational constraint on the effective volume filling factor, and thus, also on the vertical extent of the rings. Especially, Lumme et al. (1983) also argued that any intrinsic opposition effect for the particles themselves cannot replace the shadowing effect (except in the unlikely situation that the observed phase curve corresponds exactly to the single particle phase function). The derived small  $D \approx 0.02$  for the B-ring (Lumme et al. 1983), which corresponds to a vertical ring thickness of  $\sim 50$  particle radii for  $\tau \sim 1$ , seems to be in clear contradiction with our dynamical models of section 3. On the other hand, strict monolayer models (Hämeen-Anttila and Pyrkko 1972; Hämeen-Anttila and Vaaranemi 1975), although allowing the tilt effect, cannot account for the opposition behavior without an intrinsic opposition peak for the particles. It is thus of considerable interest to check what is the photometric behavior of the dynamical models sketched in Section 3, falling between these two extremes. Besides calculating the photometric implications of these dynamical models, we also briefly check that our method can reproduce the main results of the previous studies.

#### 4.1. Opposition brightening

Theoretical arguments (Irvine 1966) suggest that the maximum increase in the single scattered component is by a factor of 2 at the exact opposition, and that significant brightening takes place over an angular range  $\alpha \sim D$ . To get a quantitative picture, we have performed MC calculations with  $D$  ranging from 0.004 to 0.1. We start by assuming a homogeneous layer of particles, with  $\tau_{dyn} = 0.4$  and 1.0, the values which have been used to represent Saturn’s A and B rings in previous studies (Lumme and Irvine 1976; Esposito and Lumme 1977; Lumme et al. 1983). In accordance with the analysis of ground-based observations we use  $B = B'$ , so that the variation in Solar phase angle is due to the azimuthal difference in illumination and viewing. Two elevation angles,  $B = 6^\circ$  and  $26^\circ$ , represent the range for which ground-based photometry has been analyzed in previous literature.

Figure 12 displays the ratio of simulated singly scattered flux to the theoretical one for  $D = 0$  (Eq. 33), as a function of  $\alpha$  for various  $B, \tau$  combinations. Also shown is the theoretical enhancement ratio. According to Lumme and Bowell (1981), the inclusion of shadowing yields

$$\frac{I}{F} = 2p_1\phi_p(\alpha)\phi_s(\alpha, \bar{\mu}, \tau, D)\frac{\mu_0}{\mu + \mu_0}, \quad (36)$$

where  $p_1$  is the geometric albedo of particles and  $\phi_p$  is the particle phase-function, normalized to

unity at  $\alpha = 0$ . The shadowing function  $\phi_s$  is calculated by (Lumme and Bowell 1981)

$$\begin{aligned}\phi_s(\alpha, \bar{\mu}, \tau, D) &= x e^x \int_{t_0}^1 t^{2x-1} e^{-xt} dt, \\ x &= \frac{-\ln(1-D)}{1.19 \sin(\alpha)} \approx \frac{D}{1.19 \sin(\alpha)}, \\ t_0 &= \exp(-\tau/(x\bar{\mu})),\end{aligned}\tag{37}$$

where  $\bar{\mu} = 2\mu\mu_0/(\mu + \mu_0)$  is the harmonic mean of the sines of the illumination and observation elevations: observations at slightly different  $\mu$  and  $\mu_0$  are usually reduced to this representative value. These formulas were originally derived in Lumme and Bowell (1981) for arbitrary shaped, non-identical particles: in the above form they apply to identical spherical particles (Lumme et al. 1983). In the limit  $\tau/\bar{\mu} \rightarrow \infty$ ,  $t_0 \rightarrow 0$  and the integral yields  $\phi_s(\alpha = 0^\circ) = 1$ , whereas  $\phi_s \rightarrow 0.5$  as  $\alpha \gg 0^\circ$ .

In terms of  $P(\alpha)$  (Lumme and Irvine 1976),

$$p_1 \phi_p(\alpha) = AP(\alpha)/4,\tag{38}$$

so that combining Eqs. 37 and 36 with Eq. 33 indicates enhanced single scattering

$$E(\alpha, \bar{\mu}, \tau, D) \equiv E(x, \tau/\bar{\mu}) = \frac{I/F(D)}{I/F(D=0)} = \frac{2\phi_s(x, \tau/\bar{\mu})}{1 - \exp(-\tau_{path})},\tag{39}$$

corresponding to a 2-fold maximum increase in exact opposition for  $\tau_{path} \rightarrow \infty$ . According to Fig. 12, the agreement of  $I_{ss}$  with the Lumme-Bowell formula is very good in all cases, including those where  $\tau_{path}$  is moderately small. Especially, the  $D$ -dependence is fairly accurately described for the studied range  $D < 0.1$ . Also, the multiply scattered contribution near opposition is practically unaltered by different  $D$ 's, in agreement with Esposito (1979).

**Insert here Fig. 12**

**Figure 13 studies in more detail the dependence of maximal opposition enhancement on  $\tau_{path}$  ( $=2\tau/\bar{\mu}$ ). In the limit  $\alpha/D \rightarrow 0$ , while keeping  $\tau/\bar{\mu}$  finite, one has  $t_0 \rightarrow 1$  and the Eq. 37 implies  $\phi_s \rightarrow 1 - \exp(\tau/\bar{\mu})$ , indicating**

$$E_{max} = \frac{2}{1 + \exp(-\tau_{path}/2)}\tag{40}$$

**for any non-zero  $D$ . This formula seems to be very accurately valid even for  $\tau_{path} \sim 1$ , when the enhancement is only about 20%. This figure also compares the simulated and theoretical angular width of the opposition peak, evaluated numerically from Eq.**

**37**, likewise indicating a fairly good agreement for all studied  $\tau_{path}$  values. Note that in the extreme case studied,  $\tau_{dyn} = 0.25$ , so that  $H/s$  is only about 3 for  $D = 0.1$

**Insert here Fig. 13**

In Lumme et al. (1983) the above formulas (Eqs. 36 and 37) for single scattered flux were applied in fitting the observed phase curves of Saturn’s B ring at various elevation angles, and it was found that a homogeneous multilayer model with  $D = 0.02$  and  $\tau > 1$  gave a satisfactory fit for the whole range  $B = 6^\circ - 26^\circ$ . Additionally, the estimated amount of multiple scattering yielded a set of acceptable combinations of asymmetry parameters  $g$  and single-particle albedos  $A$ . In Fig. 14 (upper row) we use one of the final models in Lumme et al. (1983) (their Model A assuming a Henyey-Greenstein phase function with  $g = -0.30, A = 0.92$ ), together with their observations in the red band. In agreement with Lumme et al. (1983) the observed steepness of phase curve corresponds fairly well to  $D = 0.02$ , for both studied values of  $B$ , while for example  $D = 0.1$  would make the opposition peak much too extended. On the other hand, even with  $D = 0.02$  we have a disagreement between our calculated overall  $I/F$  level and observations for  $B = 26^\circ$ : we return to this in the next section addressing the tilt-effect in more detail. In the case of a strict monolayer model the brightness would stay practically constant over the studied  $\alpha$  range.

**Insert here Fig. 14**

Is there a way to make high  $D$  preferred by dynamical models consistent with the observed opposition effect? In principle, the vertical profile might help to reduce the width of the opposition peak for low elevation angle observations, as the scattering will occur mainly on the upper layers with smaller  $D$  than in the central plane. However, in itself this effect is too weak to modify significantly the opposition peak. For example, taking the  $\tau_{dyn} = 1.25$  run with identical 5 meter particles, with  $D(0) = 0.33$  (Table 1), yields for  $B = 6^\circ$  a phase curve which is fairly close to the  $D_{uni} = 0.1$  curve in Fig. 12, whereas for  $B = 26^\circ$  it would be much flatter, close to that one would obtain for  $D_{uni} = 0.33$ . Consequently, the vertical distribution alone seems not to be able to account for the observed steepness of opposition brightening in the case of dense rings.

On the other hand, as shown in the previous section, an extended size distribution is much more effective in shifting the photometric behavior to resemble that with lower  $D$ . The two lowermost rows in Fig. 14 apply the size distribution models of the previous section, and indeed, when the size range is sufficiently extended (0.05 to 5 meters), a very good fit to observations on both  $B$  values is achieved. In this figure a Henyey-Greenstein function with  $g = -0.35$  was used, chosen with the purpose of fitting the brightness level of the curve in the last frame with observations. A similar reasonable fit can be obtained with the Callisto phase function: in Fig. 15 the most extended size distribution model of Fig. 14 is compared to observations (Lumme et al. 1983) in both red and blue. Although no specific attempt was made to deduce any set of best  $g$  and  $A$  combinations, the overall agreement is fairly good. Thus at least in principle the observed opposition effect of Saturn’s rings could be interpreted as arising from mutual shadowing, without any contradiction between



dynamical and photometric assumptions. The requirement for this is that the size distribution extends to about 0.05 meters, for a particle elasticity close to that of the Bridges et al. (1984) formula.

Insert here Fig. 15

It is of interest to compare the effect of the size distribution on the width of the opposition peak,  $w$ , with the treatment of semi-infinite particle layers in Hapke (1986), according to which

$$\tan(w/2) = \frac{n_e(1) \langle \sigma \rangle \langle r \rangle}{2} \quad (41)$$

$$n_e = -n \log(1 - D)/D \quad (42)$$

where  $\langle \sigma \rangle$  is the number averaged scattering cross-section of particles,  $\langle r \rangle = \sqrt{\langle \sigma \rangle / \pi}$ ,  $n$  is the number density of particles, while  $n_e$  is the effective number density for extinction when taking into account the finite volume density. These quantities are to be evaluated at the layer where the slant optical depth calculated according to Eq. 42 equals unity ( $n_e = n_e(1)$ ). Inserting  $n = D / \langle V \rangle$ , where  $\langle V \rangle$  is the average volume of particles, yields

$$w/D \approx \frac{2 \tan(w/2)}{-\log(1 - D)} = \frac{\langle \sigma \rangle \langle r \rangle}{\langle V \rangle}, = \frac{3}{4} \frac{\langle s^2 \rangle^{1.5}}{\langle s^3 \rangle} \quad (43)$$

In the case of identical particles this gives  $w/D \approx 3/4$ , whereas in the general case  $w/D$  depends on the form of the size distribution at the depth of effective scattering  $\tau_s \approx 1$ . In Hapke (1986) the function  $Y = \frac{\langle s^2 \rangle^{1.5}}{\langle s^3 \rangle}$  was tabulated for different power-law size distributions, as a function of  $W_s = s_{max}/s_{min}$ . Especially, for  $q = 3$ ,

$$Y = \frac{\sqrt{2}(\log(W_s))^{1.5} W_s}{(W_s - 1)(W_s^2 - 1)^{0.5}} = Y_{Hapke} \times \frac{W_s^2}{(W_s - 1)(W_s^2 - 1)^{0.5}} \quad (44)$$

a correction factor has been added to Hapke's tabulated value  $Y_{Hapke}$ , valid for the limit  $W_s \gg 1$ .

Insert here Fig. 16

In Fig. 16 the simulated width of the opposition peak is compared to Eq. 43, using the size distribution runs with  $W_s = 1 - 100$ , and comparing both the cases with  $B = B' = 6^\circ$  and  $B = B' = 26^\circ$ . In the left-hand frame the angular width of the opposition peak is shown normalized by a common value  $D = 0.3$  (close to the typical value of  $D(z = 0)$  in these runs), to emphasize the absolute trend of  $w$  vs.  $W_s$ , as well as the large difference between  $B = 6^\circ$  and  $26^\circ$ . Although for  $B = 26^\circ$  the simulated  $w/D$

is close to that predicted by Eq. (44), for  $B = 6^\circ$  the actual width is much smaller. A more appropriate comparison is made in the right-hand frame, using  $D$ 's evaluated at the depth where the slant optical depth is unity. For  $B = 26^\circ$  these vary between  $D = 0.15 - 0.28$ , while for  $B = 6^\circ$ ,  $D = 0.021 - 0.095$ . These are very similar to values indicated by Fig. 9, although for consistency, we have now used Hapke's formula, Eq. 42, which corresponds to  $\tau_{phot}/\tau_{dyn} \approx 1 + 0.5D$ , instead of  $\tau_{phot}/\tau_{dyn} = 1/(1 - D) \approx 1 + D$  used in the previous plot. Now for both  $B = 6^\circ$  and  $B = 26^\circ$  the behavior of  $w/D$  is close to that predicted by Eq. 44 (solid line). The clearest discrepancy is seen for small  $W_s$ , corresponding to systems with the highest effective volume density - in fact, part of this discrepancy would be removed if  $\tau_{phot}/\tau_{dyn} = 1/(1 - D)$  were used.

Figure 16 also shows the curves  $Y_{26^\circ}$  and  $Y_{6^\circ}$ , evaluated using the actual particle size distributions at the geometric depth corresponding to  $\tau_s = 1$  (dotted and dash-dotted lines), deviating slightly from the effective  $Y$  for the whole system, due to the above described vertical segregation of sizes. However, the difference is not very pronounced. Also note carefully that the curves for  $Y_{26^\circ}$  and  $Y_{6^\circ}$  do not fall close to the correct simulated values: for  $B = 6^\circ$  the simulated width is narrower than the predicted one, whereas the opposite is true for  $B = 26^\circ$ . This could be due to an additional  $\tau_{path}$  effect similar to that studied for identical particles in Fig. 13, which is not included to Hapke's formulas for semi-infinite layer. Nevertheless, Hapke's physical picture of opposition peak being mainly determined by effective photometric parameters at the unit slant optical depth seems to be fairly useful in interpreting the simulation results, and in accordance with the speculations we presented in connection to Figs. 8 and 9.

#### 4.2. Tilt effect

Ground-based observations indicate that the brightness of the A ring is almost independent of elevation (tilt) angle while that of the B-ring increases by about 25% between 6 and 26 degrees (Lumme and Irvine 1976). In Lumme and Irvine (1976) (see also Price 1974), this brightening was interpreted in terms of increased multiple scattering for increasing  $\mu$ , this component being much more important in the B-ring ( $\tau = 1$ ) than in the A-ring ( $\tau = 0.4$ ). However, it was fairly difficult to get enough multiple scattering, even with the single scattering albedo close to unity. For example, the Lambert-phase function can not yield a strong enough tilt-effect for the B-ring (Lumme and Irvine 1976). In Esposito and Lumme (1977) it was proposed that an inclusion of a forward scattering lobe to the single particle phase function, using formulas of the type of Eq. 26, would help in this respect, by enhancing the amount of multiple scattering.

In both Lumme and Irvine (1976) and Esposito and Lumme (1977)  $D = 0$  was assumed. Strict monolayer models with Lambert-type particles can also produce a strong tilt-effect without the need for multiple scattering (Hämeen-Anttila and Vaaraniemi 1975). Basically the brightening with increasing elevation would then be due to limb-darkening of particles: at low elevation angles only

shallowly illuminated edges of the particles are visible, reducing the brightness. As  $B = B'$  increases larger portions of the particles become visible, including the almost perpendicularly illuminated bright particle centers. For even larger  $B$  the gaps between particles become visible, finally reducing the brightness. Since for monolayer models lower  $\tau$  corresponds to a larger separation between particles, this eventual dimming is achieved at smaller elevation for  $\tau = 0.4$  than for  $\tau = 1.0$ , explaining the difference for the A and B-rings in the monolayer-models.

**Insert here Fig. 17**

Fig. 17 (uppermost row) compares Monte Carlo calculations for monolayer models similar to those in Hämeen-Anttila and Vaaraniemi (1975) (Lambert-scattering) and for multilayer models with the same phase functions as in Esposito and Lumme (1977). Models for both the A and the B ring are shown, together with observations (Lumme and Irvine 1976) in the green band ( $\alpha = 6^\circ$ ). Multiple scattered contributions are shown separately, to emphasize the basic difference in the cause of the tilt-angle behavior in these two models. Due to high  $D$  in the monolayer model, a lower particle albedo can account for the overall brightness level. However, the abrupt drop in the brightness as  $\mu \rightarrow 0$  predicted by the monolayer model is not present in the observations, which on the other hand are well fitted by the models of Esposito and Lumme (1977). The results of our calculations agree well with the theoretical curves presented in both Hämeen-Anttila and Vaaraniemi (1975) and in Esposito and Lumme (1977). Note that in the former study a successful comparison was made to another set of observations (Hämeen-Anttila and Pyykko 1972), which however was based on many fewer images than that of Lumme and Irvine (1976) and also may suffer from an inadequate smearing correction (see Lumme and Irvine (1976)).

In the middle row of Fig. 17 vertically uniform systems with increasing volume densities are compared, for the Callisto phase function. In accordance with Section 3.4, larger  $D$ , or equivalently a smaller vertical thickness, enhances the brightness. According to Fig. 14 this can be interpreted to follow from the more extended opposition peak for larger  $D$ . For the A-ring case the opposition brightening is less pronounced, due to its lower  $\tau$  (compare to Fig. 12). In comparison to a monolayer, the strong drop in brightness for  $\mu \rightarrow 0$  is absent (or just weakly present for  $D = 0.1$ ), indicating that this effect in the monolayer model is an artifact caused solely by the requirement of having the particle centers strictly in the same plane, and not due to non-zero  $D$ . However, all the curves for uniform  $D$  are rather flat for  $\tau = 1$ , and thus not able to account for the B-ring tilt-effect.

In the case of an extended size distribution (lowermost row in Fig. 17) the tilt effect for the B-ring is nicely fitted. This follows from the fact that for low elevation angles the reflection is mainly due to the rarefied envelope formed by the small particles, whereas with increasing elevation the dense inner layers become more important. Consequently, the  $I/F$  curve follows the curves of successfully larger constant  $D$  as  $\mu$  increases. Also in these size distribution models the required amount of multiple scattering is fairly small, allowing for a moderately low particle albedo. In the figure the best fit is achieved for  $s_{min} \approx 0.10 - 0.5$  meters, smaller and upper minimum values

yielding either a bit too flat, or too rapidly rising  $I/F$  vs  $\mu$ , respectively. On the other hand, the observed flatness of the A-ring tilt curve is less sensitive to size distribution.

Thus, models with moderately high central plane filling factor seem to be consistent with both the opposition and tilt-angle behavior of the B-ring, provided that the particles' size distribution is taken into account. However, as mentioned above we were not able to find a very satisfactory fit to observations for a uniform system with  $D = 0.02$ , in terms of multiple scattering in large albedo models (see Fig. 14, upper row). Since this result disagrees with the conclusions in Lumme et al. (1983), even though the same phase function was used, we considered it important to check the cause of the difference. In this respect it is important to note that in Lumme et al. (1983) the comparison to observations was only made in an indirect manner, via the fraction of multiple scattering indicated by their observational fits and their theoretical models, not by actually comparing the fitted and observed brightness curves. As described below, the inability to account for the observed tilt-behavior with the Lumme et al. (1983)'s phase function is likely to arise from their way of combining the theoretical opposition-brightened single scattering flux and the numerically calculated fractional amount of multiple scattering.

In Lumme et al. (1983) the total intensity (for  $\mu = \mu_0 = \bar{\mu}$ ) was written as

$$I(\alpha, \bar{\mu})/F = p_1 \phi_p(\alpha) \phi_s(\alpha, \bar{\mu}) + p_m(\bar{\mu}), \quad (45)$$

where, as in Eq. 37,  $\phi_p$  and  $\phi_s$  are the normalized particle phase-function, and the above described Lumme-Bowell shadowing function ( $\phi_s(\alpha = 0^\circ) = 1$  and  $\phi_s \rightarrow 0.5$  for  $\alpha \gg 1^\circ$ ),  $p_1$  is the geometric albedo, and  $p_m$  is the contribution of multiple scattering ( $p_m \rightarrow 0$  as  $\mu \rightarrow 0^\circ$ ). For the studied range  $\alpha < 6^\circ$ ,  $\phi_p(\alpha)$  stays close to unity. Thus  $I(0^\circ, \bar{\mu})/F = p_1 + p_m(\bar{\mu})$  whereas for example for  $\alpha = 6^\circ$ , studied in Fig. 17,  $I(6^\circ, \bar{\mu})/F \approx p_1/2 + p_m(\bar{\mu})$ . Lumme et al. (1983) define the multiple scattering factor

$$Q(\bar{\mu}) = p_m(\bar{\mu})/(p_1 + p_m(\bar{\mu})), \quad (46)$$

which corresponds to the fractional contribution of multiple scattering at *zero phase angle* (including the opposition brightening of the single scattered contribution). From fits to their observed phase curves at various  $\bar{\mu}$ , Lumme et al. (1983) find  $p_1$  to stay practically constant, and determine the value of  $Q(\bar{\mu}) \equiv Q_{obs}$ . For a given choice of the particles' phase function,  $p_1$  then determines the single particle albedo  $A$ . The next step in Lumme et al. (1983) was to use a radiative transfer code, *without* allowance for mutual shadowing, for determining  $Q_{model}(\bar{\mu})$  for the adopted phase function. A large range of models with different  $A$ 's and parameters  $b, g_1, g_2$  in a 2-lobe Henyey-Greenstein phase functions were systematically explored and the fit was considered acceptable if this  $Q_{model}$  agreed with  $Q_{obs}$  at all observed  $\bar{\mu}$ 's within error bars. However, the problem in this procedure is with this identification of  $Q_{model}$  and  $Q_{obs}$ . Namely, as the opposition effect was not included in their theoretical multiple scattering calculations, these yield a  $Q'_{model}$  which actually corresponds to

$$Q'(\bar{\mu}) = p'_m(\bar{\mu})/(p_1/2 + p'_m(\bar{\mu})), \quad (47)$$

where  $p_1/2$  is the singly scattered flux without a contribution from opposition brightening. As a consequence, the actual amount of multiple scattering,  $p'_m = \frac{p_1 Q'}{2(1-Q')}$ , following from Eq. 47 is only one-half of  $p_m = \frac{p_1 Q}{(1-Q)}$  following from Eq. 46. Thus, the identification of  $Q_{model}$  with  $Q_{obs}$  in Lumme et al. (1983) seems to have overestimated the amount of multiple scattering following from the assumed phase function by a factor of two.

**Insert here Fig. 18**

Support for our conclusion about the cause of the discrepancy is given in Fig. 18, showing the singly and multiply scattered contributions for the Lumme et al. (1983) Model A, calculated by our MC method. With  $D = 10^{-3}$ , approximating the classical limit, we find a good agreement with the  $Q_{model}$  calculated by Lumme et al. (1983) (see their Table IV): however the combined  $I_{ss} + I_{ms}$  (solid line) falls clearly below observations. On the other hand, if we multiply by two the fractional contribution of multiple scattering, as we suspect is implied by their procedure, the  $I_{ss} + 2I_{ms}$  (dashed line) would fall much closer to the observations, in the manner indicated by Fig. 3 in Lumme et al. (1983). The same holds for the other models in Table IV in Lumme et al. (1983). The only effect of the non-zero  $D$  is to increase slightly the amount of single scattering: using  $D = 0.02$  instead of  $D = 0.001$  shifts the I/F curves upward by about 0.03 for all  $\mu$ . In conclusion, it seems that in order to account for the B-ring tilt effect with multiple scattering, an even larger fractional contribution of multiple scattering would be needed than implied by Lumme et al. (1983)'s models.

### 4.3. Voyager observations

In their detailed analysis of Voyager images Dones et al. (1993) successfully explain the overall photometric behavior of the A-ring, in terms of macroscopic ( $s \gg \lambda_{vis}$ ) backscattering ring particles. The deduced single particle phase function and albedo vary slightly with planetocentric distance, the particles becoming less backscattering ( $g \approx -0.55 \rightarrow -0.5$ ) toward the outer edge, and albedo slowly decreasing being, however, close to 0.5 throughout the ring. The amount of microscopic forward scattering dust was estimated to be very small. However, Dones et al. (1993) also point out several aspects in which the photometric behavior deviates from that following from their classical radiative transfer models. For example, the optical depth profile derived from Voyager 2 photopolarimetric (PPS) occultation measurements shows a correlation with the reflected intensity profile, which is not expected for a thick multilayer ring at low elevation angles for which  $\tau_{path} \gg 1$ . Also, the A ring as a whole shows a reversed contrast in high and low phase angle images, the inner parts being brighter than the outer parts for low  $\alpha$ , while the opposite is true for high  $\alpha$ . Contrast reversal is seen also locally near strong density waves, which appear brighter than their surroundings at large  $\alpha$  and less bright for  $\alpha < 20^\circ$ . For the outer thirds of the A-ring Dones *et al.* find that a power-law type particle phase function can reproduce well both the small and large  $\alpha$  behavior, whereas for the inner two thirds their models imply too much brightness for

$\alpha > 100^\circ$ . As suggested by Dones et al. (1993) all these discrepancies may be related to a smaller vertical thickness in the inner portion of the A-ring, the thickness gradually increasing toward the outer boundary, for example due to the net energy input via numerous satellite resonances. In the density wave regions themselves the local thickness may be expected to be most strongly enhanced.

**Insert here Fig. 19**

The effect of small vertical thickness on the brightness at large phase angle is tested in Fig. 19. Here Voyager observations for the inner A-ring ( $a=122,500$  km, with  $\tau \sim 1$ ) are compared to models with different volume filling factors. As the optical depth in this region is higher than the typical value for the A-ring, a larger  $D$  (possibly further enhanced by a smaller  $H$ ) may also be expected. The left panel (with  $D \approx 0$ ) corresponds to Fig. 17 in Dones et al. (1993), indicating how power-law phase functions giving the right brightness in the small  $\alpha$ -regime fail to fit the high  $\alpha$  observations. As in Dones et al. (1993), the scaled reflectivity,  $I/F$  multiplied by  $\frac{4(\mu+\mu_0)}{\mu_0}$ , is shown. For low  $\alpha$ , where single scattering dominates, this multiplying factor removes the geometric part of Eq. 33, the scaled intensity thus representing the product  $AP(\alpha)$ , making it easier to compare observations with different  $B$  and  $B'$ . In the right panel, a homogeneous model with  $D = 0.1$  is studied (corresponding to  $H/s \approx 13$ ). In agreement with the cases studied in Section 3, larger volume density enhances single scattering, making it possible to match the low  $\alpha$  observations with a nearly 20% smaller albedo. Since the high  $\alpha$  brightness is mainly due to multiple scattering, this is consequently reduced due to the change in  $A$ . Also, as the multiple scattering component is reduced by the non-zero  $D$  itself (see Fig. 11, and Table 3), the total reduction amounts to about one half, enough to bring the large  $\alpha$  brightness to a reasonable agreement with observations. Similar improvement in the match can be achieved for even somewhat larger  $D$ 's. In contrast, a monolayer model would fail, giving a too *small* high  $\alpha$  brightness, if the albedo is reduced to match the low  $\alpha$  brightness. However, in the case where an extended particle size distribution (with  $s_{min} < 1.0$  meters) is included, the match is not as much improved over that for  $D = 0$ , since the enhancement in low  $\alpha$  brightness is less than for single-sized particles and since the multiply scattered component for large  $\alpha$  is in fact almost the same as in the  $D = 0$  case (see Table 3). **However, the use more elastic particles would increase the effective  $D$  also in the case of a more extended size distribution: for example, if a constant elasticity  $\epsilon_n = 0.1$  is adopted, then  $s_{min} = 0.1$  meters (see Table 3) would yield a very similar curve as obtained for  $s_{min} = 1.0$  meters in the case of the Bridges *et al.* elasticity law (corresponds in many respects  $\epsilon_n \sim 0.5$ ), being still within the uncertainty of observations.**

For Voyager observing geometries the brightness of a thick multilayer ring with  $D = 0$  is expected to be practically independent of optical depth for  $\tau > 0.4$ , characteristic for the A-ring. The allowance of non-zero  $D$  alone will not change the situation if  $D$  is constant with  $\tau$  (see Fig. 11). However, in dynamical simulations  $D$  always increases monotonically with  $\tau$ , and if this increase is strong enough, it may lead to a correlation between  $I$  and  $\tau$  also for the interesting range of  $\tau = 0.4 - 1.0$ . Fig. 20 displays the  $I$  vs.  $\tau$  dependence for dynamical simulation models, both for identical 5 m particles and for an extended size distribution with  $s_{min} = 0.1$  m. Both low and high

phase angle are studied, and the simulation parameters are also listed in Table 2. For identical particles  $D(z = 0)$  increases from 0.12 to 0.25 as  $\tau_{phot}$  varies from  $0.4 \rightarrow 1.0$ , leading to about a 10% increase in the low  $\alpha$  brightness, in contrast to less than 2% variation for the  $D = 0$  case. The resulting  $I$  vs.  $\tau$  dependence is also applied for constructing a model radial brightness profile for the A-ring, based on PPS optical depth measurements (Fig. 20, lower frame) . Although the modeled brightness variations are smaller than the actual ones, there is some similarity to observations of the inner A-ring (see. e.g. Fig. 7 in Dones et al.). In comparison, in the case of extended size distribution the sensitivity of brightness on  $\tau$  is much reduced, and the model brightness profile is almost as flat as that for the  $D = 0$  case. For large phase angles the brightness is practically constant for  $\tau = 0.4 - 1.0$ , in all three cases.

**Insert here Fig. 20**

In principle, the difference found above in the low and high phase I/F dependence on  $\tau$  (for the identical particle model) implies that the ratio  $I_{135^\circ}/I_{155^\circ}$  increases slightly with  $\tau$ . Thus the inner portion of the A-ring, with higher than average  $\tau$ , would be relatively more bright in low  $\alpha$  images in comparison to large  $\alpha$ , than the optically thinner outer ring. However, according to the model of Fig. 20 this ratio varies less than 10% for  $\tau = 0.4 - 1.0$ , and is thus insignificant in comparison to the observed large contrast difference between the inner and outer A-ring. The observed strength of contrast reversal amounts to roughly 2, if estimated by the ratio of

$$\frac{I/F(\alpha = 9^\circ, a \approx 122,500 \text{ km})}{I/F(\alpha = 9^\circ, a \approx 136,000 \text{ km})} \approx 1.3 \quad (48)$$

and

$$\frac{I/F(\alpha = 155^\circ, a \approx 122,500 \text{ km})}{I/F(\alpha = 155^\circ, a \approx 136,000 \text{ km})} \approx 0.65, \quad (49)$$

indicated by Figs. 7 and 9 in Dones et al. (1993). Qualitatively, this strong contrast reversal might be accounted for if the effective  $D$  has a rather high value, say  $D > 0.2$ , at the inner A-ring, decreasing to practically zero near the outer edge. The possible effects of such variations are studied in Fig. 21a, showing the fractional brightness enhancement in non-zero  $D$  models over that for  $D = 0$ , as a function of phase angle. According to this figure, a uniform system of identical particles with  $D = 0.2 \rightarrow 0$  as  $a$  increases from  $122,500 \rightarrow 136,000 \text{ km}$  could provide nearly the observed amount of difference. In this simple picture, neglecting any optical depth or phase function effects, the overall brightness profile would be flattest for  $\alpha \approx 120^\circ - 130^\circ$ , where the enhancement in the brightness due to non-zero  $D$  turns into reduced brightness. However, again the inclusion of an extended size distribution ( $s_{min} < 1 \text{ m}$ ) would significantly weaken this effect, at least for the Bridges et al. (1984) elasticity law.

**Insert here Fig. 21**

The reduced brightness at strong density wave regions relative to their surroundings, seen in low  $\alpha$  images, and respectively the increased brightness in large  $\alpha$  images (see Figs. 7-9 in Dones

et al. (1993)) might in principle also follow from a reduced  $D$  due to locally enhanced ring thickness. However, the model in terms of spatial variation in  $D$  only is insufficient to account for the fact that the contrast reversal occurs at  $\alpha \approx 20^\circ$  (see Fig. 22 in Dones et al. (1993)), not around  $120^\circ$  as in the model of Fig. 21a. On the other hand, if we assume that a significant number of small particles is released in the resonance zone (say,  $\sim 10$  cm particles otherwise trapped on the surfaces of the larger particles) the situation improves. Fig. 21b shows a crude model for the Mimas 5:3 resonance zone. For the background ring,  $\tau_{dyn} = 0.4$  is assumed (corresponding to the PPS occultation value), and a size distribution from 0.5 to 5 meters, while for the resonance zone the distribution is extended to 0.15 meters, which for a power-index  $q = 3$  indicates enhanced  $\tau_{dyn} = 0.6$ . In the resonance zone the effective  $D$  is reduced due to these extra particles, making it dimmer in the backscattered light than the surrounding region. However, for  $\alpha > 20^\circ$  the increase in  $\tau$  is sufficient to brighten the resonance site over its surroundings (without increased  $\tau$  the reversal would take place near  $\alpha = 120^\circ$ , as can be roughly estimated by comparing the curves for the two size distribution models compared in Fig. 21a). Altogether, the qualitative agreement of this simple experiment to the observations shown in Fig. 22 in Dones et al. (1993) is surprisingly good, except that the observed amplitude of contrast is about 50% larger. There are several obvious ways to refine this model: for example assuming also larger vertical thickness for the resonance site would further decrease its  $D$ , thus increasing the brightness drop for low  $\alpha$ .

## 5. Discussion and Summary

Photometric modeling of Saturn’s rings, including multiple scattering and a particle size distribution, has been carried out in a straightforward manner by using a Monte Carlo (MC) technique (see e.g. Plass and Kattawar 1968; Salo 1988). We assumed that the layer of simulation particles was illuminated by a large number of photons, arriving either from the Sun or from Saturn, and followed in detail the path of each individual photon through the successive scatterings. The new direction after scattering was obtained by MC-sampling from either the surface element’s scattering law, or from a spherical-particle phase function: in the latter case it was found more accurate to continue the photon path from the intersection point, not from the particle center. The periodic boundary conditions of the dynamical simulation were taken explicitly into account, so that a photon escaping from the actual calculation region enters one of the image regions of the original simulation region. Inclusion of image particles is very important in modeling of low illumination and viewing elevations.

Some computational tricks were employed to enhance the efficiency of the calculations (e.g. in the search of intersection points, treatment of image particles). Most importantly, the direct MC-method was augmented with a backward MC, as it would be very wasteful to deduce the brightness of the system in a given viewing angle by sampling only photons leaving the system to this direction. Instead, for each scattering event we checked whether the scattering point was visible from the pre-defined viewing direction. If so, we added the contribution of this scattering



to the final brightness in this direction, taking into account the scattering law of the particle or surface element. In this manner, each of the path segments of each photon may contribute to the result in the direction we are interested in. Compared to direct MC this reduces the necessary number of photons by even a factor of 1000, for a given desired accuracy.

The results of the Monte Carlo code were checked against previous calculations, both in the limit of vanishing volume density  $D$  (Dones et al. 1993; Esposito and Lumme 1977) and in the limit of a monolayer (Hämeen-Anttila and Vaaraniemi 1975). Different phase-functions (Lambert, Henyey-Greenstein, power-law) and both ground-based and Voyager geometries were checked. Also comparisons to Chandrasekhar’s analytical expressions for isotropic scattering were used. The obtained good agreement in all these tests, and the good computational efficiency of the indirect method, makes it well suited for detailed photometric modeling of Saturn’s rings.

Our experiments with homogeneous systems with non-zero  $D$  indicate that finite ring thickness can lead to significant brightening of the singly scattered reflected component (and reduction of the transmitted one) whereas the multiple scattering is less affected, in agreement with Dones et al. (1989), Peltoniemi and Lumme (1992), and Esposito (1979). For perpendicularly illuminated layers of identical particles with  $\tau \sim 1$ , this brightening amounts to roughly  $(1 + 2D)$  for most directions of emerging radiation. Increased brightness is also obtained for low elevation illumination, being most pronounced at small phase angles. However, high  $\alpha$  brightness, dominated by multiple scattering for backward-scattering particles, is reduced. Non-zero  $D$  also enhances the photometric optical thickness of the particle layer over its dynamical optical depth, the latter defined by the total fractional area of particles, often termed also geometric optical thickness (see e.g. French and Nicholson 2000). For homogeneous systems of identical particles  $\tau_{phot}/\tau_{dyn} \approx 1 + kD$ , with  $k \sim 1 - 1.5$ , consistent with Esposito (1979) and Peltoniemi and Lumme (1992). In the case of a vertical profile, a fairly similar result for  $\tau_{phot}/\tau_{dyn}$  is obtained when the central plane volume filling factor  $D(z = 0)$  is used for  $D$ . Somewhat weaker increase is obtained also in the case of extended size distribution ( $k \sim 0.7 - 1$ , for  $s_{max}/s_{min} = 50$ ). For dynamical models of identical particles where the vertical thickness often corresponds to only a few particle diameters,  $\tau_{phot}$  may exceed  $\tau_{dyn}$  even by 50%, as reported already by Wisdom and Tremaine (1988). In the case of a strict monolayer, the derived  $\tau_{phot}$  increases strongly with decreased path elevation, but this effect seems to be small if even a modest amount of vertical thickness is allowed for.

In the case of particle fields taken from dynamical simulations, many important differences are seen. In this case the vertical profile is not uniform, but is determined by the balance between collisional dissipation, viscous heating, and the vertical energy flux (see e.g. Schmidt et al. 1999). Especially, when the particle size distribution is included, the overall enhancement of reflected single scattering is reduced, even by about 50% for  $s_{max}/s_{min} = 50$  and power-law index  $q = 3$ . For very oblique paths this reduction is even stronger, resulting from the elevation angle dependent photometric properties of the layer. Namely, for slanted paths the system becomes optically thick on the layers which correspond to a much smaller effective  $D$  than the central plane density. On the other hand, when the layer is viewed more and more perpendicularly, the better the dense central

parts are visible. Inclusion of a size distribution enhances dependence effect significantly, as the vertical energy balance typically implies larger velocity dispersion and consequently larger layer thickness for the small particles in comparison to the largest ones (see Tables 1 and 2), leading to a strong gradient in the vertical volume density profile.

Our experiments of opposition brightening for homogeneous systems of identical particles confirm the theoretical calculations of mutual shadowing by Lumme and Bowell (1981), which seem to describe very accurately the enhancement of single scattering in all our simulations with  $\tau_{path} = 1 \rightarrow 20$ ,  $D < 0.1$ . Also, our experiments indicate that the observed steepness of I/F vs.  $\alpha$  for the B-ring corresponds closely to that for a homogeneous system with  $D \approx 0.02$ , in agreement with Lumme et al. (1983). However, this estimate for  $D$  is much smaller than those based on dynamical considerations, including the dynamical models studied in the present work. This discrepancy has previously led to the suggestion that the opposition brightening (or at least a major part of it) is produced intrinsically on particle surfaces and is not due to mutual interparticle shadowing (Cook et al. 1973; Hämeen-Anttila and Vaaraniemi 1975; Hapke 1986). Mishchenko and Dlugach (1992) suggested that the narrow brightness peak is produced by coherent backscattering, i.e. due to constructive interference of light from small regolith grains on the ring particles' surfaces. Further support for this was presented in Mishchenko (1993), pointing out that the brightness enhancement is expected to be connected with a sharp peak in negative linear polarization. Observations by Lyot (1929) and Johnson et al. (1980) indeed indicate such a narrow polarization peak for Saturn's rings, with half-width of about 0.3 degrees, which made Mishchenko (1993) conclude that the observed brightness peak is completely due to the coherent backscatter effect. However, this evidence given by the polarization peak is weakened by the study of Dollfus (1996), who did not find such a peak but only a much more shallow increase in negative polarization, typical for many Solar System surfaces. Nevertheless, recent analysis of HST multi-color observations (Poulet et al. 2002) imply that the coherent backscatter in terms of the Shkuratov et al. (1999) model can successfully account for the opposition brightening.

One of our main results is that mutual shadowing can hardly be excluded as an at least partial explanation for the opposition peak. This holds true even in the case of dynamically dense systems, provided that the ring possesses an extended distribution of sizes. In fact, mutual shadowing is likely to be important for all extended size distribution models presented in the literature. The examples of Section 3 indicated that for the Bridges et al. (1984)'s elasticity law, a minimum particle size  $s_{min} = 0.05$  meters was able to approximate quite well both the low and large tilt angle phase curves. This estimated size range  $s_{max}/s_{min}$  is roughly consistent with that derived from Voyager radio occultation measurements (Marouf et al. 1983), as well as that recently estimated by French and Nicholson (2000), who obtained  $s = 30$  cm to 20 meters based on the amount of forward diffracted light estimated from comparison of Voyager and ground-based occultation experiments. The widths of the opposition peak we calculate are in fairly good agreement with Hapke (1986) theoretical formula.

**Insert here Fig. 22**

However, the opposition brightening due to mutual shadowing is likely to depend on all the dynamical factors affecting the vertical volume density profile, including besides the size distribution also the dynamical optical depth and the elasticity of particle impacts. In Fig. 22 some additional examples are provided for  $s_{min} = 0.1$  m, illustrating the role of particle elasticity in dynamical simulations. Besides the Bridges *et al.*'s formula used in section 3, also more elastic particles with  $v_c/v_B = 4$  in Eq. 30 are studied, as well as more inelastic particles with a constant coefficient of restitution  $\epsilon_n = 0.1$ . In comparison to the case  $v_c/v_B = 1$ , the more elastic case leads to a larger vertical thickness of the system, and similarly the  $\epsilon_n = 0.1$  case leads to a significantly more flattened ring. As a consequence, the less elastic case with a larger volume density leads to a clearly wider opposition peak, whereas for  $v_c/v_B = 4$  the peak gets more narrow, and in fact approximates the observations at least as well as the more extended size distribution with  $v_c/v_B = 1$ . Clearly, detailed comparisons between various models and observations, combined with the allowance for the intrinsic opposition peak, would provide efficient constraints for the local properties of rings.

The tilt effect for the B-ring seems to follow very naturally from the inclusion of a vertical profile and size distribution. The basic mechanism for the tilt effect in our models is the increase of the backscattering brightness for a layer with a non-zero  $D$ . With increased elevation angle deeper and thus denser regions contribute to the scattering, making the total brightness increase. It is important to note that this brightness increase is not limited to the regime of the opposition peak: also size-distribution systems with a rather narrow opposition peak exhibit an increase in the general brightness level. In section 3 the best fit for brightening with elevation angle was obtained for a distribution with  $s_{min} = 0.1$  meters; however models with  $s_{min}$  in the range of 0.05 to 0.5 meters would also fall within the uncertainty of the used ground-based data (and the uncertainty of particles elastic properties). For smaller optical depths, corresponding to the A-ring, the overall effect is small, in accordance with observations, and is not very sensitive to minimum size. As for the opposition effect, better observational data of the elevation angle behavior would help to constrain the particle size distribution.

It is interesting to note that the non-homogeneous vertical structure as an explanation for the B-ring tilt-effect was theoretically considered already by Hämeen-Anttila and Pyykko (1972), in terms of a two-component model with bright particles near the central plane being surrounded by an envelope of small particles with a lower albedo. Possible physical explanations for the albedo difference were also given, in terms of large particles being coated by smaller ones. Altogether this model for the tilt effect resembles the present explanation, except that we attribute the brightness of the central layer to the high volume-density induced brightening. Models even more similar to ours were studied in Jantunen (1982), who proposed that in the case of a vertical profile the broad opposition peak of the dense central parts of the rings will become visible in the case of increased tilt angle. Except for not taking into account the particle size distribution, her models are very similar to ours.

On the other hand, our model for the tilt effect differs from that by Lumme and Irvine (1976) and Lumme *et al.* (1983), who attribute the brightening to an increased amount of multiple scat-

tering in optically thick rings. In principle, this would work provided that the single scattering albedo is very close to unity, and phase functions like those in Esposito and Lumme (1977) are assumed. However, the recent analysis of HST observations (Cuzzi et al. 2002) suggests that multiple scattering is insignificant for Earth-based observing geometries, as they found very little difference in the elevation angle behavior between observations at different wavelengths. A similar conclusion about multiple scattering was obtained by Dones et al. (1993) from analysis of Voyager observations. Our mechanism for the tilt effect in terms of a vertically thin ring model is consistent with these observations, as no multiple scattering is involved.

The allowance of non-zero volume density in Saturn’s rings helps to account for many previously problematic Voyager observations, like the difficulties in matching simultaneously the low and high  $\alpha$  brightnesses for the inner A-ring, as well as for the B-ring (Dones et al. 1993; Doyle et al. 1989) with classical  $D = 0$  models, the rings having only about one half of the modeled brightness in large  $\alpha$ . If we accept that these ring regions are likely to be strongly flattened, the implied brightening for low  $\alpha$  observations will reduce the fitted  $AP(\alpha)$  value, leading to a decreased brightness for large  $\alpha$  due to less multiple scattering. The large  $\alpha$  brightness is further reduced by the non-zero  $D$  itself. Reasonable fits to observations are also obtained in the case of size distribution with  $s_{min} > 0.1 - 1.0$  meters (lower limit increasing with increasing elasticity). On the other hand, the outermost A-ring fits well with classical models (Dones et al. 1993), consistent with a large local ring thickness. This implied distance dependence of ring thickness offers also a possible qualitative explanation for the contrast reversal between the inner and outer A-ring, as seen in low and high  $\alpha$  images. Contrast reversals are also seen in strong resonance zones, taking place for  $\alpha \approx 20^\circ$ : a simple model for this was also presented, in terms of an enhanced amount of small particles in the resonance site, accompanied by an increase in the local optical depth. The A-ring also exhibits an overall correlation between optical depth and intensity which significantly exceeds that expected for a optically thick multilayer ring. According to our models based on dynamical simulations for identical particles, such an effect might be expected to take place via the optical depth dependent volume density. However, this seems to be not possible for any extended size distribution.

All the models addressed in this study have assumed planar homogeneity. Dynamical studies indicate that particle mutual self-gravity will inevitably lead to local particle inhomogeneities, gravity wakes (Salo 1992a), provided that the local velocity dispersion is small. For example this would be the case when the Bridges et al. (1984) elasticity law is assumed. Due to the preferential orientation of wakes, trailing by about  $20^\circ$  with respect to the local tangential direction, the appearance of the system becomes dependent on the ring longitude. Indeed, strong observational evidence for wakes is provided by the azimuthal brightness asymmetry, at least for their presence in the mid A-ring (Dones et al. 1993; Franklin et al. 1987). Wakes may well be present also in the dense parts of the B-ring, where the larger surface mass density can be expected to compensate the stronger disrupting effect of the differential rotation in comparison to the A-ring. However, for the B-ring the larger optical depth may reduce the contrast related to such formations. Such gravitational wakes, if present, will modify the local volume density and optical depth: in wakes

$D$  will be enhanced, whereas the regions between wakes may appear as partially transparent. This is likely to lead to differences in the ring opening angle dependence of the ring brightness, as the relative fraction of visible wake/inter-wake regions will depend on the observing elevation. Also, since the strength of wakes is dependent on surface mass density, this might introduce an additional mechanism causing dependence between local optical thickness and local brightness. The photometric effects of the wake structure will be studied in detail in paper II.

In addition to wakes, there are also other possible dynamical phenomena which might be reflected in the photometric properties of rings. For example, dense rings may be susceptible to viscous overstability, manifesting as coherent axisymmetric velocity, density and local thickness oscillations (Borderies et al. 1985; Mosqueira 1996; Schmit and Tscharnuter 1995). Our recent studies, including direct N-body simulations with plausible parameter values for the densest parts of the B-ring, have confirmed the viability of this mechanism (Salo et al. 2001; Schmidt et al. 2001; Schmidt and Salo 2003). Like gravity wakes (which may co-exist with overstability (Salo et al. 2001)), coherent axisymmetric oscillations, if present, will modify the volume density of rings. A longitude and elevation angle dependence may also be expected, most likely different from that due to non-axisymmetric wakes.

We have explored the effect of non-zero  $D$  for Saturn’s ring’s photometry, and shown that using the particle distribution data obtained from dynamical simulation models helps in many instances to account for the observed photometric properties. For example the B-ring tilt effect follows in a very robust way from the dynamical models. Several qualitative ways to account for the Voyager observations were also sketched. Interestingly, some of the implications of these simple models are not well in accordance with the currently preferred view of Saturn’s rings possessing a wide power-law distribution of particle sizes extending down to cm-range. A summary of various results is provided in Table 4. For example, the overall contrast reversal of the A-ring, and especially the correlation between  $\tau$  and  $I$ , would be easiest to explain with a model with a very narrow size range. Somewhat to the same direction, the predicted opposition effect due to mutual shadowing for an extended size distribution ( $s_{min} = 0.05 - 0.10$  m) is even too efficient in accounting for observations, leaving perhaps too little room for an intrinsic opposition effect. One possibility which might help to fit together these implications is that the local properties of rings, especially the size distribution, show even a larger variation with distance than usually thought, A-ring possessing a clearly narrower size range than the B-ring (say  $\sim 0.5$  meters in comparison to  $\sim 0.05$  meters) The role of self-gravity might be important in this respect, as it may lead to efficient sticking of particles in the A-ring (Salo 1992a, 1995; Ohtsuki 1993). Clearly, improved datasets with good phase angle, elevation angle and spatial coverage, as provided by the recent HST-observations (Cuzzi et al. 2002; Poulet et al. 2002), and especially by the Cassini data in the near future, will be crucial in providing constraints for the combined dynamical and photometric modeling.

**Insert here Table 4**

## 6. Conclusions

The main conclusions of our study are (see also Table 4):

1) Allowance for non-zero volume density  $D$  leads to increased  $\tau_{phot}/\tau_{dyn}$  and enhanced brightness of backward reflected single scattered radiation, in comparisons to  $D = 0$  case. For large phase angles, dominated by multiple scattering, the brightness is slightly decreased. Inclusion of a power-law size distribution dilutes these effects, but they remain significant even for the widest distribution studied, with  $s_{min} = 0.05$  meters (assuming  $s_{max} = 5$  meters and  $q = 3$ ).

2) Dynamically dense systems, even with central plane  $D(0) > 0.2 - 0.3$ , may exhibit a narrow opposition peak similar to that observed for Saturn’s rings, solely due to mutual shadowing among the small particles of an extended size distribution. The required width of the distribution depends on the vertical thickness via the particle elasticity: for the Bridges *et al.* elasticity law  $s_{min} \sim 0.05$  meters is implied, whereas more (less) elastic particles would correspond to somewhat larger (smaller)  $s_{min}$ . Thus, interparticle shadowing needs to be included in the models of the intrinsic opposition effect, and may help to set constraints for both the size distribution of particles, and the particle elasticity.

3) Simulated particle fields with non-uniform vertical density profile account for the observed elevation angle brightness dependence of Saturn’s rings. The monotonically rising B-ring tilt curve seems to be best reproduced by a size distribution with  $s_{min} \sim 0.1$  meters. The flat tilt curve for the A-ring is also reproduced, being less sensitive to size distribution.

4) Assumption of non-zero  $D$  helps to fit simultaneously both the low and high phase angle Voyager observations of Saturn’s inner A-ring. In the case of size distribution,  $s_{min} > 1$  meters is required for the Bridges *et al.* elasticity law. However, less elastic particles would allow smaller  $s_{min}$  ( $\sim 0.1$  meters for  $\epsilon_n = 0.1$ ).

5) A simple qualitative explanation for the overall contrast reversal of the inner and outer A-ring between low and high  $\alpha$  images was suggested in terms of vertical thickness increasing with planetocentric distance. Similarly, contrast reversal in resonance site seems to indicate local differences in both the size distribution and the optical thickness.

6) A correlation between optical thickness and ring brightness is also seen in low  $\alpha$  models of identical particles with large  $D$ , but this effect disappears for an extended size distribution and for large  $\alpha$ , the observed correlation probably manifesting a different mechanism.

This work was supported by the Academy of Finland and the Väisälä Foundation. We thank Kari Lumme and Jeff Cuzzi for making useful suggestions on the manuscript, and the reviewers Larry Esposito and Luke Dones for their detailed suggestions for improving the manuscript. We are also grateful to Jeff Cuzzi, Dick French, and Francois Poulet for providing preprint of their recent analysis of HST observations.

## REFERENCES

- Barkstrom, B. J. (1973). A comparison of the Minneart reflectance law and the reflectance from a nonconservative isotropic scattering atmosphere. *J. Geophys. Res.*, 78:6370–6372.
- Bobrov, M. S. (1970). *The Rings of Saturn*. NASA TT F-701 (Translation of Kol'tsa Saturna, Nauka, Moscow).
- Borderies, N., Goldreich, P., and Tremaine, S. (1985). A granular flow model for dense planetary rings. *Icarus*, 63:406–420.
- Bridges, F. G., Hatzes, A., and Lin, D. N. C. (1984). Structure, stability and evolution of Saturn's rings. *Nature*, 309:333–335.
- Camichel, H. (1958). Mesures photométriques de Saturne et de son anneau. *Annales d'Astrophysique*, 21:231–242.
- Chandrasekhar, S. (1960). *Radiative transfer*. New York: Dover, 1960.
- Cook, A. F., Franklin, F. A., and Pallucioni, F. D. (1973). Saturn's Rings - A Survey. *Icarus*, 18:317–337.
- Cuzzi, J. N., French, R. G., and Dones, L. (2002). HST multicolor (255 - 1042 nm) photometry of Saturn's main rings. I. Radial profiles, phase and opening angle variations, and regional spectra. *Icarus*, 158:199–223.
- Cuzzi, J. N., Lissauer, J., Esposito, L., Holberg, J., Marouf, E., Tyler, G., and Boischot, A. (1984). Saturn's rings: Properties and processes. In Greenberg, R. and Brahic, A., editors, *Planetary Rings*, pages 73–199. The University of Arizona Press.
- Daisaka, H. and Ida, S. (1999). Spatial structure and coherent motion in dense planetary rings induced by self-gravitational instability. *Earth Planets Space*, 51:1195–1213.
- Dollfus, A. (1996). Saturn's rings: Optical reflectance polarimetry. *Icarus*, 124:237–261.
- Dones, L., Cuzzi, J. N., and Showalter, M. R. (1989). Simulations of light scattering in planetary rings. In *Dynamics of Astrophysical Discs*, pages 25–26. Cambridge University Press.
- Dones, L., Cuzzi, J. N., and Showalter, M. R. (1993). Voyager photometry of Saturn's A Ring. *Icarus*, 105:184–215.
- Doyle, L. R., Dones, L., and Cuzzi, J. N. (1989). Radiative transfer modeling of Saturn's outer B ring. *Icarus*, 80:104–135.
- Esposito, L. W. (1979). Extension to the classical calculation of the effect of mutual shadowing in diffuse reflection. *Icarus*, 39:69–80.

- Esposito, L. W. and Lumme, K. (1977). The tilt effect for Saturn’s rings. *Icarus*, 31:157–167.
- Franklin, F. A., Cook, A. F., Barrey, R. T. F., Roff, C. A., Hunt, G. E., and de Rueda, H. B. (1987). Voyager observations of the azimuthal brightness variations in Saturn’s rings. *Icarus*, 69:280–296.
- French, R. G., Dones, L., and Salo, H. (2000). HST Observations of the azimuthal brightness asymmetry in Saturn’s rings. *Bull. Am. Astron. Soc.*, 32:864.
- French, R. G. and Nicholson, P. D. (2000). Saturn’s Rings II. Particle sizes inferred from stellar occultation data. *Icarus*, 145:502–523.
- Hämeen-Anttila, K. A. and Pyykko, S. (1972). Photometric behaviour of Saturn’s rings as a function of the Saturnocentric latitudes of the Earth and the Sun. *A&A*, 19:235–247.
- Hämeen-Anttila, K. A. and Vaaraniemi, P. (1975). A theoretical photometric function of Saturn’s rings. *Icarus*, 25:470–478.
- Hapke, B. (1986). Bidirectional reflectance spectroscopy. IV - The extinction coefficient and the opposition effect. *Icarus*, 67:264–280.
- Irvine, W. M. (1966). The shadowing effect in diffuse reflection. *J. Geophys. Res.*, 71:2931–2937.
- Jantunen, H. (1982). The photometric function for Saturn’s rings. *Moon and Planets*, 26:383–387.
- Johnson, P. E., Kemp, J. C., King, R., Parker, T. E., and Barbour, M. S. (1980). New results from optical polarimetry of Saturn’s rings. *Science*, 283:146–149.
- Julian, W. H. and Toomre, A. (1966). Non-axisymmetric responses of differentially rotating disks of stars. *ApJ*, 146:810–830.
- Lane, A. L., Hord, C. W., West, R. A., Esposito, L. W., Coffeen, D. L., Sato, M., Simmons, K. E., Pomphrey, R. B., and Morris, R. B. (1982). Photopolarimetry from Voyager 2 - Preliminary results on Saturn, Titan, and the rings. *Science*, 215:537–543.
- Lumme, K. and Bowell, E. (1981). Radiative transfer in the surfaces of atmosphereless bodies. I - Theory. *AJ*, 86:1694–1704.
- Lumme, K. and Irvine, W. M. (1976). Photometry of Saturn’s rings. *AJ*, 81:865–893.
- Lumme, K., Irvine, W. M., and Esposito, L. W. (1983). Theoretical interpretation of the ground-based photometry of Saturn’s B ring. *Icarus*, 53:174–184.
- Lumme, K. and Reitsema, H. J. (1978). Five-color photometry of Saturn and its rings. *Icarus*, 33:288–300.
- Lyot, B. (1929). Recherche sur la polarization de la lumière des planètes et de quelques substances terrestres. *Ann. Obs. Meudon VIII, Fasc 1. (NASA-TTF-187, 1964)*.



- Marouf, E. A., Tyler, G. L., Zebker, H. A., Simpson, R. A., and Eshleman, V. R. (1983). Particle size distributions in Saturn’s rings from Voyager 1 radio occultation. *Icarus*, 54:189–211.
- Mishchenko, M. I. (1993). On the nature of the polarization opposition effect exhibited by Saturn’s rings. *ApJ*, 411:351–361.
- Mishchenko, M. I. and Dlugach, Z. M. (1992). Can weak localization of photons explain the opposition effect of Saturn’s rings? *MNRAS*, 254:15P–18P.
- Mosqueira, I. (1996). Local simulations of perturbed dense planetary ring. *Icarus*, 122:128–152.
- Ohtsuki, K. (1993). Capture probability of colliding planetesimals - dynamical constraints on accretion of planets, satellites, and ring particles. *Icarus*, 106:228–246.
- Ohtsuki, K. and Emori, H. (2000). Local N-body simulations for the distribution and evolution of particle velocities in planetary rings. *AJ*, 119:403–416.
- Peltoniemi, J. I. and Lumme, K. (1992). Light scattering by closely packed particulate media. *J. Opt. Soc. Am. A*, 9:1320–1326.
- Plass, G. N. and Kattawar, G. W. (1968). Monte Carlo calculations of light scattering from clouds. *Applied Optics*, 7:415–419.
- Porco, C. C., Throop, H. B., and Richardson, D. C. (2001). Light scattering in Saturn’s rings: Basic disk properties and the A Ring azimuthal asymmetry. *Bull. Am. Astron. Soc.*, 33:1091–1092.
- Poulet, F., Cuzzi, J. N., French, R. G., and Dones, L. (2002). A study of Saturn’s ring phase curves from HST observations. *Icarus*, 158:224–248.
- Price, M. J. (1974). Optical scattering properties of Saturn’s ring. II. *Icarus*, 23:388–398.
- Price, M. J. and Baker, A. (1975). Illumination of Saturn’s ring by the ball. I - Preliminary results. *Icarus*, 25:136–145.
- Richardson, D. C. (1994). Tree code simulations of planetary rings. *MNRAS*, 269:493–511.
- Salo, H. (1988). Monte Carlo modeling of the net effects of coma scattering and thermal reradiation on the energy input to cometary nucleus. *Icarus*, 76:253–269.
- Salo, H. (1991). Numerical simulations of dense collisional systems. *Icarus*, 90:254–270.
- Salo, H. (1992a). Gravitational wakes in Saturn’s rings. *Nature*, 359:619–621.
- Salo, H. (1992b). Numerical simulations of dense collisional systems. II - Extended distribution of particle sizes. *Icarus*, 96:85–106.
- Salo, H. (1995). Simulations of dense planetary rings. III. Self-gravitating identical particles. *Icarus*, 117:287–312.

- Salo, H. (2001). Numerical simulations of collisional dynamics of planetary rings. In Pöschel, T. and Luding, S., editor, *Granular Gases*, pages 330–349. Springer.
- Salo, H. and Karjalainen, R. (1999). Dynamical and photometric modeling of azimuthal brightness asymmetry in Saturn’s rings. *Bull. Am. Astron. Soc.*, 31:1160.
- Salo, H., Karjalainen, R., and French, R. G. (2000). Modeling the azimuthal brightness asymmetry in Saturn’s rings. *Bull. Am. Astron. Soc.*, 32:864.
- Salo, H., Schmidt, J., and Spahn, F. (2001). Viscous overstability in Saturn’s B-ring: I. Direct simulations and measurement of transport coefficients. *Icarus*, 153:295–315.
- Schmidt, J. and Salo, H. (2003). Weakly Nonlinear Model for Oscillatory Instability in Saturn’s Denese Rings. *Physical Rev. Letters*, 90:061102(1)–(4).
- Schmidt, J., Salo, H., Petzschmann, O., and Spahn, F. (1999). Vertical distribution of temperature and density in a planetary ring. *A&A*, 345:646–652.
- Schmidt, J., Salo, H., Petzschmann, O., and Spahn, F. (2001). Viscous overstability in Saturn’s B-ring: II. Hydrodynamic theory and comparison to simulations. *Icarus*, *in press*.
- Schmit, U. and Tscharnuter, W. (1995). A fluid dynamical treatment of the common action of self-gravitation, collisions, and rotation in Saturn’s B-ring. *Icarus*, 115:304–319.
- Shkuratov, Y. G., Kreslavsky, M. A., Ovcharenko, A. A., Stankevich, D. G., Zubko, E. S., Pieters, C., and Arnold, G. (1999). Opposition Effect from Clementine Data and Mechanisms of Backscatter. *Icarus*, 141:132–155.
- Sobouti, Y. (1963). Chandrasekhars’s X-, Y-, and related functions. *ApJS*, 7:411–560.
- Toomre, A. and Kalnajs, A. J. (1991). Spiral chaos in an orbital patch. In *Dynamics of Disc Galaxies (B. Sundelius, Ed.)*, Göteborg, Sweden, pages 341–358.
- van de Hulst, H. C. (1980). *Multiple Light Scattering: Tables, Formulas and Applications Vol. 1-2*. Astronomical Observatory: University of Leiden, 1980, Academic Press, New York.
- Wisdom, J. and Tremaine, S. (1988). Local simulations of planetary rings. *AJ*, 95:925–940.

Fig. 1.— Definition of the coordinate system and angle variables used in the dynamical and photometric simulations. The x-axis points to the radial direction, the y-axis toward the orbital mean motion, while the z-axis completes a right-handed coordinate system.

Fig. 2.— Some examples of particle distributions used in photometric calculations. In the upper row a homogeneous system with volume density  $D = 0.1$  is shown, both as projected to the equatorial plane, and as seen from the side, along the direction of the orbital motion. The model was created by randomly placing the particles to the calculation region, with the condition that no overlaps are allowed between particles or periodic image particles. The two other examples are snapshots from dynamical simulations, using the Bridges *et al.*'s (1984) elasticity law to describe the inelastic collisions. In all cases, just the innermost region of the particle field is displayed, having a factor of 2.5 larger actual extent in both planar directions. In the case with the most extended size distribution used ( $s = 0.05 - 5\text{m}$ ), the total number of particles is  $\sim 200,000$ .

Fig. 3.— Relation between dynamical and photometric optical depths. The frame on the left shows the ratio  $\tau_{phot}/\tau_{dyn}$  for homogeneous systems with different vertical thicknesses, measured by  $H/s$ , where  $H$  is the full thickness of the layer occupied by the particle centers and  $s$  is the radius of particles. In the middle, the same ratio is shown as a function of volume density  $D$ , for  $\tau_{dyn} = 0.5, 1.0$  and  $2.0$ . Also shown are linear fits,  $\tau_{phot}/\tau_{dyn} = 1 + kD$ , with  $k = 1.0, 1.25$  and  $1.5$ . In all cases photometric optical depth is calculated for a path with  $B_s = 90^\circ$ . On the right, the normal photometric optical depth, deduced from various slanted paths ( $\tau_{phot} = \tau_s/\sin B_s$ ) is illustrated, both for a monolayer model ( $H/s = 0$ ), and for a moderately thin multilayer  $H/s = 6$ : only  $\tau_{dyn} = 0.5$  is shown for the latter case, but for example  $\tau_{dyn} = 1.5$  yields a practically identical result. Error bars in  $\tau_{phot}$  are calculated from  $(fN_{phot})^{-0.5}/\sin B_s$ , where  $f$  is the fraction of photons passing through the system without being intercepted.

Fig. 4.— Comparison of the direct vs. indirect method. A homogeneous system with  $\tau_{phot} \approx \tau_{dyn} = 0.5$  and  $D = 0.001$  is perpendicularly illuminated ( $B' = 90^\circ$ ) with  $N_{phot} = 10^7$  photons. In the direct method, escaping photons are sampled with 2 degree bins in the observing elevation  $B$ , averaged over the whole azimuth range. Lambert surface-element scattering was used with albedo  $A = 1$ , and contributions from different orders of scatterings ( $k$ ) are shown separately. Large boxes stand for the indirect method and dots for the direct method. Solid curves indicate the theoretical single scattered ( $k = 1$ ) flux for  $D = 0$  (Eqs. 33).

Fig. 5.— Check of the validity of the error estimates. The same particle field as studied in Fig. 4 was illuminated from  $B' = 45^\circ$ , and viewed from various elevations. The azimuthal difference in viewing and illumination was  $\theta - \theta' = 10^\circ$ . The upper row shows results from MC-simulations with  $10^4$  and  $10^5$  photons; in the direct method  $10^\circ \times 10^\circ$  bin-size has been used. In the lower frames the error estimates from a single run according to Eqs. 14 and 18 are shown with dashed lines, and compared with the actual RMS-difference in a series of 10 simulations performed with different seeds of the random number generator (symbols). Note the much larger error in the direct method as compared to the indirect method, even for the very large collection bin used. Lambert element's

reflection law has been used and  $A = 1$  is assumed.

Fig. 6.— The effect of non-zero volume density  $D$  on the brightness of a perpendicularly illuminated homogeneous system. Lambert reflection is used with  $A=0.5$ . The singly (SS) and multiply (MS) scattered components are shown separately, with  $I_{tot} = I_{ms} + I_{ss}$ . The dashed and solid curves indicate the theoretical  $I_{ss}$  for  $D = 0$ , both for  $\tau = 1.0$  and  $1.5$ . The former  $\tau$  value corresponds to the used  $\tau_{dyn}$ , while the latter value equals the photometric  $\tau$  for  $D = 0.2$ ,  $\tau_{dyn} = 1.0$  according to Fig. 3. Note that the  $I/F$  scales for reflected intensities do not start from zero.

Fig. 7.— The brightness change of a homogeneous system with  $\tau_{dyn} = 1$ ,  $D = 0.1$  in comparison to  $D \rightarrow 0$ , shown separately for singly scattered (upper row), multiply scattered (middle) and total reflected radiation (lowermost row). Three cases of oblique illumination with  $B' = 60^\circ$ ,  $20^\circ$  and  $8^\circ$  are compared, as a function of observing elevation  $B$  and azimuth with respect to illumination,  $\phi - \phi'$ . Only  $B > 0$  is shown as the behavior of transmitted light is qualitatively similar to that in Fig. 6, with no strong  $\phi - \phi'$  dependence. Note the logarithmic scale of  $B$ , chosen to emphasize the low elevation angle behavior. Lambert reflection is used with  $A=0.5$ . Contours corresponding to reduced brightness are shown by dashed lines. The multiply scattered fluxes for  $D = 0$  were constructed from runs with  $D = 0.10$  and  $D = 0.01$ , by  $I_{ms}(D = 0) = I_{ms}(D = 0.01) - 0.01/0.09 \times (I_{ms}(D = 0.10) - I_{ms}(D = 0.01))$ . The CPU time consumption (with 2.2 GHz Pentium processor and LINUX/g77 compiler) was about 10 sec/direction/ $5 \cdot 10^5$  photons, for  $N = 10^4$  particles. For  $D = 0.01$  the CPU-consumption is about 2-fold as compared to  $D = 0.1$ , due to larger physical thickness.

Fig. 8.— The effect of size-distribution on the brightness of a perpendicularly illuminated system. The combined singly scattered and multiply scattered fluxes (Lambert scattering with  $A=0.5$ ) are shown for the size distribution models of Fig. 9, and compared with the homogeneous  $D_{uni} = 10^{-3} \approx 0$  model for the same  $\tau_{dyn} = 1.25$ . The  $\tau_{dyn} = 1.5$  model with the most extended distribution  $s = 0.05 - 5.0$  m is not shown: in reflected light it would fall almost on top of  $s_{min} = 0.1$  m model, while in the transmitted light the larger  $\tau$  would lead to somewhat smaller  $I/F$ .

Fig. 9.— In the upper frame the effective vertical thickness  $H$  as a function of particle size is shown for the studied size distribution models. The effective value for different size bins is calculated by  $H = \sqrt{12 \langle z^2 \rangle_{bin}}$ , based on the formula  $\langle z^2 \rangle = \frac{H^2}{12}$  valid for a vertically homogeneous layer with a total thickness  $H$ . In each case the minimum and maximum particle sizes are indicated, while the power-law index  $q = 3$ . Except for the case with  $s_{min} = 0.05$  m, all distributions are taken from dynamical simulations with  $\tau_{dyn} = 1.25$ , after 20 orbital periods, when the collisional steady-state has been established. For the case of  $s_{min} = 0.05$  m, the distribution has been created by adding particles to the simulation with  $s = 0.1 - 5$  m: the size distribution of these extra particles extends smoothly the power-law of the original particles, and the vertical dispersion assigned to them follows that of the smallest 10% of the particles in the original distribution. This extrapolation is justified by the trend in different simulations with decreasing  $s_{min}$ . For a power-law with  $q = 3$ , the extension of  $s_{min}$  from 0.1 to 0.05 m increases  $\tau_{dyn}$  from 1.25 to 1.5. The Bridges et al. (1984)'s

elasticity law has been assumed, and the upper limit of the size distribution is fixed to 5 meters. The simulations were performed for  $a = 100,000 \text{ km}$  but there is little difference in the  $H/s$  for other  $a's$ . In the lower frame the relation between the volume density and optical depth is shown for the models of the upper row. This was constructed by tabulating separately the functions  $D(z)$  and  $\tau_z(z)$ , where the latter describes the total photometric optical depth of particles with  $z_i > z$ , estimated by  $\int_z^\infty n(z') < \pi s^2 >_{z'} (1 - D(z'))^{-1} dz'$ , where  $n(z')$  is the total number density, and  $\pi < s^2 >$  the number-averaged geometric cross section at the height  $z'$ . Vertical lines, from the left to right, indicate where  $\tau_z(z)/\sin B_s$  equals unity, for  $B_s = 6^\circ$  and  $B_s = 26^\circ$ , respectively.

Fig. 10.— Comparison between using Lambert elements' reflection law and Lambert-sphere phase function, both for continuing the post-scattering photon path from the particle center or from the intersection point. A homogeneous system with  $D = 0.1$ ,  $\tau_{dyn} = 1$ ,  $A = 0.5$  is studied.

Fig. 11.— Comparison of Monte Carlo calculations to Figs. 11 and 12. in Dones *et al.* (1993). The Callisto phase function (=Eq. 27 with  $n = 3.09$ , see Dones *et al.*) is used, and  $A = 0.5$ . Lines are traced from Dones *et al.*, while boxes stand for the present calculations with  $D \approx 0$ ,  $\tau \approx \tau_{dyn} = 1$ . Crosses indicate a few additional calculations with  $D = 0.1$ . In the calculation of Saturn's illumination, the mean of  $I/F$  obtained by using the red- and blue-band Saturn models in Dones *et al.* is shown. The low  $\alpha(13.2^\circ)$  curves have  $B = 12.8^\circ$  and  $B' = 8^\circ$ , while for large  $\alpha(155.3^\circ)$ ,  $B = 9.7^\circ$  and  $B' = 3.9^\circ$ .

Fig. 12.— Opposition brightening of singly scattered radiation. Results of MC simulations for homogeneous systems with  $D = 0.004$ ,  $0.02$  and  $0.1$  are shown for different  $B$  and  $\tau_{dyn}$  combinations, together with the theoretical model by Lumme and Bowell (1981) (curves represent Eq. 39). Simulation phase curves have been scaled by  $D \approx -\log(1 - D)$  to make it easier to compare different  $D$ 's to the theoretical curve: the horizontal scale corresponds to  $1.15^\circ$ ,  $5.7^\circ$  and  $30^\circ$ , for  $D = 0.004$ ,  $0.02$  and  $0.1$ , respectively. The values of path optical depths marked in the plots are calculated by  $\tau_{path} = 2\tau_{dyn}/\sin B'$ , thus corresponding to  $D = 0$ . The effect of using the actual photometric  $\tau_{path}$  for  $D = 0.1$  ( $= 2.04$  instead of  $1.82$ ) is indicated by the dashed line in the  $\tau_{dyn} = 0.4$ ,  $B = 26^\circ$  case, where the difference is most significant.

Fig. 13.— On the left: the maximum amplitude of opposition brightening of singly scattered radiation as a function of  $\tau_{path}$ . The results of MC simulations of Fig. 12 for  $\alpha = 0^\circ$  are compared to Lumme-Bowell formula, predicting  $E_{max} = E(\alpha = 0) = I_{ss}(\alpha = 0, D \neq 0)/I_{ss}(\alpha = 0, D = 0) = 2(1 + \exp(-\tau_{path}/2))^{-1}$ . A few additional cases with  $\tau_{dyn} = 0.25$ ,  $B = 26^\circ$  and  $B = 50^\circ$  are also included, to extend the comparisons to lower  $\tau_{path}$ . On the right, the theoretical and simulated width  $w$  of the opposition peak are compared:  $w$  is defined by  $E(w) - 1 = (E_{max} - 1)/2$ . Solid ticks on the right axis also mark the width calculated from Hapke (1986)'s formula for a semi-infinite layer of particles. In this plot, the actual  $\tau_{path}$  calculated from simulated  $\tau_{phot}$ , and the exact logarithmic factor are used in theoretical formulas.

Fig. 14.— In the uppermost row homogeneous systems with different  $D$ 's are compared to the

observed B-ring phase curves. The observational curves for  $B' = B = 6^\circ$  and  $26^\circ$  are constructed from Lumme et al. (1983) Eqs. (4), (5) and Table IIb, using  $I_{EZ}/F = 0.68$  for the calibration of the brightness of Saturn's equatorial zone in the red ( $\lambda = 620 \text{ nm}$ , Lumme and Reitsema (1978)). The assumed albedo ( $A=0.92$ ) and phase function (Henye-Greenstein law with  $g = -0.3$ ) correspond to model A in Lumme et al. (1983), and  $\tau_{dyn} = 1$ . In the two lower rows size distribution models with increasing width are compared ( $\tau_{dyn} = 1.25$ , except for the last model for which  $\tau_{dyn} = 1.5$ ). The albedo is the same as in the homogeneous models, while  $g = -0.35$ .

Fig. 15.— The most extended size distribution model ( $s = 0.05 - 5m$ ,  $\tau_{dyn} = 1.5$ ) of Fig. 14 is compared to the observed red and blue phase curves of Saturn's B-ring. The observational curves for red are the same as in Fig. 14, and the curves for blue ( $\lambda = 430 \text{ nm}$ , Lumme and Reitsema (1978)) are also from Eqs. (4), (5) and Table IIb in Lumme et al. (1983), using  $I_{EZ}/F = 0.26$ . Models assume the Callisto phase function.

Fig. 16.— The width of opposition peak in size distribution simulations, in comparison to Hapke (1986)'s formulas. In the left panel, the width of the opposition peak for elevations  $B = 6^\circ$  and  $B = 26^\circ$  is shown, normalized by  $D = 0.3$ , which approximates the central plane filling factor in our size distribution runs (see table 2). The solid line indicates the function  $Y = \frac{3\langle s^2 \rangle^{1.5}}{4\langle s^3 \rangle}$ , while the dashed line indicates the approximation valid for  $s_{max}/s_{min} \gg 1$ , given in Table I in Hapke (1986). In the right panel, the width is normalized by the volume filling factor at unit slant optical depth,  $D(\tau_s = 1)$ , yielding a fair agreement with theoretical formula. In addition, dashed and dotted curves indicate the values of  $Y$  evaluated directly from the particle distributions.

Fig. 17.— Monte Carlo calculations of the A and B ring tilt effect, in comparison to Lumme and Irvine (1976) observations in green light ( $\lambda = 550 \text{ nm}$ , Lumme and Reitsema (1978)). The observed values are traced from the Figs. 5 and 2 in Esposito and Lumme (1977), using  $I_{EZ}/F = 0.62$ . In the upper row, Monte Carlo calculations for a homogeneous ring with  $D \approx 0$  and for a monolayer are compared. For the multilayer model, Eq. 26 with  $g_1 = -0.5$ ,  $g_2 = 0.5$ ,  $b = 0.4538$  was used, while for the monolayer Lambert element scattering was assumed. The dashed lines indicate the amount of multiple scattering. Here  $\tau_{phot} = 0.4$  and  $1.0$  for both multilayer and monolayer models: in the latter case this actually refers to  $\tau_{phot}(90^\circ)$ . In the middle row, runs for homogeneous systems with different  $D$ 's are compared, using Callisto phase function. In the lower-most row, extended size distributions models are studied ( $\tau_{dyn} = 0.4$  and  $1.25 - 1.5$  for A and B-ring models, respectively). In all cases  $\alpha = 6^\circ$ .

Fig. 18.— Model A in Lumme et al. (1983) is studied: Henye-Greenstein phase function with  $g = -0.3$ ,  $A = 0.92$ , homogeneous multilayer with  $D = 0.001$  and  $\tau_{dyn} = 1$ , for  $\alpha = 6^\circ$ . The observational values for the red band are from Table IIa in Lumme et al. (1983). The solid curves show the single scattering and total fluxes calculated with the MC method, as well as indicating how the results would be better consistent with observations if the multiple scattering contribution is multiplied by a factor of 2 (dashed curve). As detailed in the text, this has likely been the effect of the combination of theoretical singly scattered flux and the radiative transfer calculations

for multiple scattering, as carried out in Lumme et al. (1983). The dotted curve shows the good agreement in the calculated fractional amount of multiple scattering: symbols stand for values in Table IV in Lumme et al. (1983), while the curve denotes the current calculations. In the case  $D = 0.02$  the  $I/F$  due to single scattering would rise by about 0.03.

Fig. 19.— In the left panel, various power-law phase functions are shown in comparison to Voyager observations at  $a = 122,500$  km. A uniform ring model with  $\tau_{dyn} = 1$ ,  $D = 0.004$  is studied, approximating the classical  $D=0$  case. The scaled reflectivity, explained in the text, is shown. The data are taken from Fig. 17 in Dones et al. (1993), and the same power-law phase functions are studied, for observing geometries tabulated in Table II in Dones *et al.*, corresponding to two set of solar elevations,  $B' \approx 4^\circ$  and to  $B' \approx 8^\circ$ . In the right panel, the same phase functions are applied to a homogeneous ring with  $D = 0.1$ : due to increased brightness at backscattering, the low  $\alpha$  observations can be fitted with a smaller albedo,  $A = 0.42$ . Because of reduced multiple scattering at high  $\alpha$  (resulting both from the smaller  $A$  and from the increased  $D$  itself), also the high  $\alpha$  observations are better fitted.

Fig. 20.— Dependence between  $\tau$  and the ring brightness, for geometries corresponding to Fig. 11. Dynamical simulation models both with identical 5 m particles and with a size distribution from 0.1 to 5 meters are studied, and compared with the  $D = 0$  case. In the plot the simulation results are plotted against their photometric  $\tau$ 's, listed in table 3. In the lower frame the  $I$  vs.  $\tau$  dependences for  $\alpha = 13^\circ$  are applied for converting the PPS occultation profile into a brightness profile model.

Fig. 21.— In a) the phase angle dependence of various models is shown relative to the  $\tau = 1.0, D = 0$  multilayer model. The used values of  $\alpha, B$  and  $B'$  correspond to those in Fig. 19: the scatter of points results from combining two set of solar elevations, not from any Monte Carlo uncertainty. Models include a homogeneous system with  $D = 0.2$  and two size distribution models, with  $s_{min} = 1.0$  and 0.2 meters. In b) the difference of  $I/F$  for the Mimas 5:3 resonance site in comparison to its surroundings is modeled, by assuming that the surrounding region has  $\tau_{dyn} = 0.4$  and a size distribution from 0.5 to 5 meters. For the resonance site it is assumed that a  $q = 3$  size distribution extends to 0.15 meters, with correspondingly increased  $\tau_{dyn} = \log(\frac{5.0}{0.15}) / \log(\frac{5.0}{0.5}) \times 0.4 \approx 0.6$ . Compare with Fig. 22 in Dones *et al.* (1993). In both frames  $A = 0.5$  and the Callisto phase function are assumed.

Fig. 22.— Opposition effect due to mutual shadowing, calculated for dynamical simulations with different particle elasticities. Solid curves refer to Lumme et al. (1983) observations in red and the phase function and albedo are the same as in Fig. 14. In comparison to Fig. 14, which assumes  $v_c/v_B = 1$ ,  $s_{min} = 0.05$ m, the more elastic model with  $v_c/v_B = 4$  yields an opposition phase curve close to the observed one for  $s_{min} = 0.1$  m instead of  $s_{min} = 0.05$  m.

Table 1. Particle distributions obtained from dynamical simulations: A and B-ring models

$\tau_{dyn}$	size range <sup>1</sup>	elasticity <sup>2</sup>	D(0)	H range <sup>3</sup>	$\tau_{phot}/\tau_{dyn}$	Comment
0.4	5	$v_B$	0.14	23.7	1.12	Fig. 17
0.4	0.5 - 5	$v_B$	0.11	25.8 - 8.8	1.08	Fig. 17
0.4	0.1 - 5	$v_B$	0.10	21.7 - 9.4	1.07	Fig. 17
1.25	5	$v_B$	0.33	28.6	1.41	Fig. 8, 9, 16, 21
1.25	2 - 5	$v_B$	0.33	26.1 - 14.3	1.38	Fig. 8, 9 16,
1.25	1 - 5	$v_B$	0.33	23.3 - 9.8	1.28	Fig. 8, 9, 14, 16, 21
1.25	0.5 - 5	$v_B$	0.34	21.5 - 8.4	1.27	Fig. 8, 9, 16, 17
1.25	0.2 - 5	$v_B$	0.29	21.3 - 8.3	1.18	Fig. 8, 9, 14, 16, 21
1.25	0.1 - 5	$v_B$	0.25	20.7 - 8.6	1.15	Fig. 8, 9, 14, 16, 17, 21
1.5 <sup>4</sup>	0.05 - 5	$v_B$	0.26	23.0 - 8.2	1.16	Fig. 9, 14, 15, 16, 17
1.25	0.1 - 5	$4v_B$	0.23	32.8 - 9.3	1.16	Fig. 22
1.25	0.1 - 5	$v_B$	0.25	20.7 - 8.6	1.15	Fig. 22
1.25	0.1 - 5	$\epsilon_n = 0.1$	0.35	10.3 - 5.9	1.19	Fig. 22

<sup>1</sup>Lower and upper size limits (in meters) for a power-law size distribution with power-index  $q = 3$

<sup>2</sup>The value of the scale factor  $v_c$  in the velocity dependent elasticity law, Eq. 30, or the value of the constant coefficient of restitution.  $v_B = 0.0077 \text{ mm/sec}$

<sup>3</sup>Effective vertical thicknesses,  $H = \sqrt{12 \langle z^2 \rangle}$ , for the subgroups of smallest and largest particles, defined by dividing the system into 6 logarithmic size bins

<sup>4</sup>Obtained by extending the simulation model with the size range from 0.1 to 5 meters, by including additional non-overlapping small particles with the same vertical dispersion as the smallest particles in the original distribution



Table 2. Particle distributions obtained from dynamical simulations:  $\tau_{dyn}$  varied<sup>1</sup>

$\tau_{dyn}$	$\tau_{phot}$	$\tau_{phot}/\tau_{dyn}$	D(0)	H range [m]	$I(13^\circ)^2$	$I(155^\circ)^3$
Size distribution 0.1 - 5.0 meters, q=3						
0.1	0.10	1.02	0.03	20.7 - 7.5	0.148	0.0066
0.2	0.21	1.03	0.06	21.4 - 8.2	0.199	0.0102
0.3	0.31	1.05	0.07	23.4 - 9.4	0.218	0.0119
0.4	0.42	1.07	0.10	21.7 - 9.4	0.226	0.0129
0.5	0.53	1.07	0.11	22.6 - 10.0	0.228	0.0129
0.7	0.76	1.09	0.16	22.3 - 10.4	0.229	0.0131
1.0	1.13	1.13	0.22	21.1 - 11.3	0.229	0.0134
1.25	1.45	1.15	0.25	20.7 - 11.2	0.228	0.0134
1.50	1.83	1.22	0.32	20.7 - 12.4	0.228	0.0135
2.00	2.53	1.27	0.37	20.1 - 13.1	0.231	0.0136
Identical 5.0 meters						
0.1	0.10	1.02	0.04	22.2	0.153	0.0060
0.2	0.21	1.05	0.07	23.1	0.213	0.0093
0.3	0.33	1.09	0.11	23.3	0.238	0.0107
0.4	0.45	1.12	0.14	23.7	0.251	0.0110
0.5	0.58	1.16	0.17	24.2	0.257	0.0112
0.7	0.85	1.22	0.23	24.4	0.266	0.0113
1.0	1.33	1.33	0.29	26.1	0.275	0.0110
1.25	1.76	1.41	0.33	28.2	0.279	0.0110
1.50	2.21	1.47	0.36	30.3	0.281	0.0109
2.00	3.14	1.57	0.41	35.3	0.283	0.0108

<sup>1</sup>All simulations assume the Bridges et al. (1984) velocity dependent elasticity.

<sup>2</sup>I/F for Callisto phase function with albedo A=0.5, for the same geometry as in Fig. 11, left panel

<sup>3</sup>For the geometry of Fig. 11, right panel

Table 3. Fractional brightness change in low and high  $\alpha$  simulations<sup>1</sup>, in comparison to homogeneous D=0.001 models for the same  $\tau_{dyn}$ .

CASE	SS(13°)	MS(13°)	TOT(13°)	SS(155°)	MS(155°)	TOT(155°)
$\tau_{dyn}=0.10$ , D=0.1	19 %	-24 %	19 %	13 %	-30 %	-28 %
$\tau_{dyn}=0.25$ , D=0.1	22 %	-12 %	22 %	13 %	-20 %	- 19 %
$\tau_{dyn}=0.50$ , D=0.1	21 %	-10 %	20 %	12 %	-18 %	-17 %
$\tau_{dyn}=1.00$ , D=0.1	20 %	-8 %	20 %	12 %	-18 %	-17 %
$\tau_{dyn}=2.00$ , D=0.1	20 %	-9 %	19 %	12 %	-18 %	-17 %
$\tau_{dyn}=1.25$ , 5m	35 %	-4 %	34 %	17 %	-18 %	-16 %
$\tau_{dyn}=1.25$ , 2.0-5m	29 %	1 %	28 %	13 %	-10 %	-9 %
$\tau_{dyn}=1.25$ , 1.0-5m	22 %	6 %	21 %	6 %	-5 %	-5 %
$\tau_{dyn}=1.25$ , 0.5-5m	18 %	7 %	18 %	6 %	1 %	1 %
$\tau_{dyn}=1.25$ , 0.2-5m	13 %	8 %	13 %	3 %	2 %	2 %
$\tau_{dyn}=1.25$ , 0.1-5m	10 %	7 %	10 %	1 %	2 %	2 %
same <sup>2</sup> , $\epsilon_n = 0.1$	21 %	11 %	20 %	3 %	-6 %	-6 %
$\tau_{dyn}=0.4$ , 0.1-5m	9 %	4 %	9 %	3 %	0 %	0 %

<sup>1</sup>The values of  $B$  and  $B'$  are the same as in Fig 11

<sup>2</sup>Except for this model, the Bridges et al. (1984) velocity dependent elasticity is assumed.

Table 4. Success of Monte Carlo models in explaining various observations, and their implications for the particle size distribution<sup>1</sup>

Observation	Fitted	Minimum particle size <sup>2</sup>	Comment
B-RING:			
• Opposition effect	YES	0.05 – 0.10 m depends on elasticity <sup>3</sup>	Fig. 14 Fig. 22.
• Tilt effect	YES	~ 0.1 m	Fig. 17
A-RING:			
• Tilt effect	YES	not very sensitive	Fig. 17
• Low vs. high $\alpha$ Brightness	YES	> 0.1 – 1.0 m depends on elasticity <sup>4</sup>	Fig. 21. Table 3
• Contrast reversal			
Inner/outer ring	YES?	> 1 m	Fig. 21a
Resonance zones	YES?	0.5 m / 0.15 m ok <sup>5</sup>	Fig. 21b
• $I$ vs. $\tau$ correlation	NO	too weak even for identical particles	Fig. 20

<sup>1</sup>Note that inclusion of self-gravity is likely to be important, at least for A-ring.

<sup>2</sup>For a power law with  $s_{max} = 5$  meters and  $q = 3$ .

<sup>3</sup>Implied minimum size decreases with elasticity:  $s_{min} \approx 0.05$  m for Bridges *et al.* elasticity law

<sup>4</sup>Implied minimum size increases with elasticity:  $s_{min} \sim 1$  m for Bridges *et al.* elasticity law

<sup>5</sup>0.15-0.5 meter particles released at the resonance

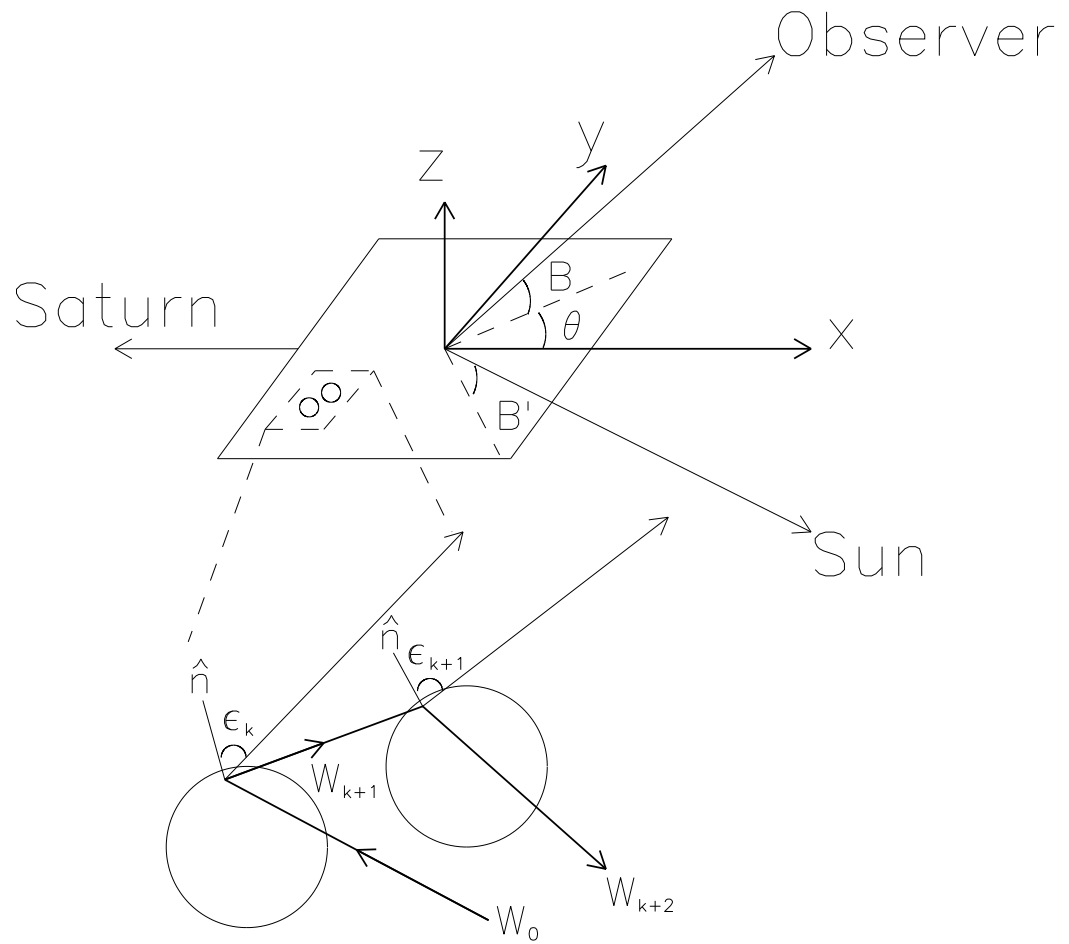


Fig. 1.

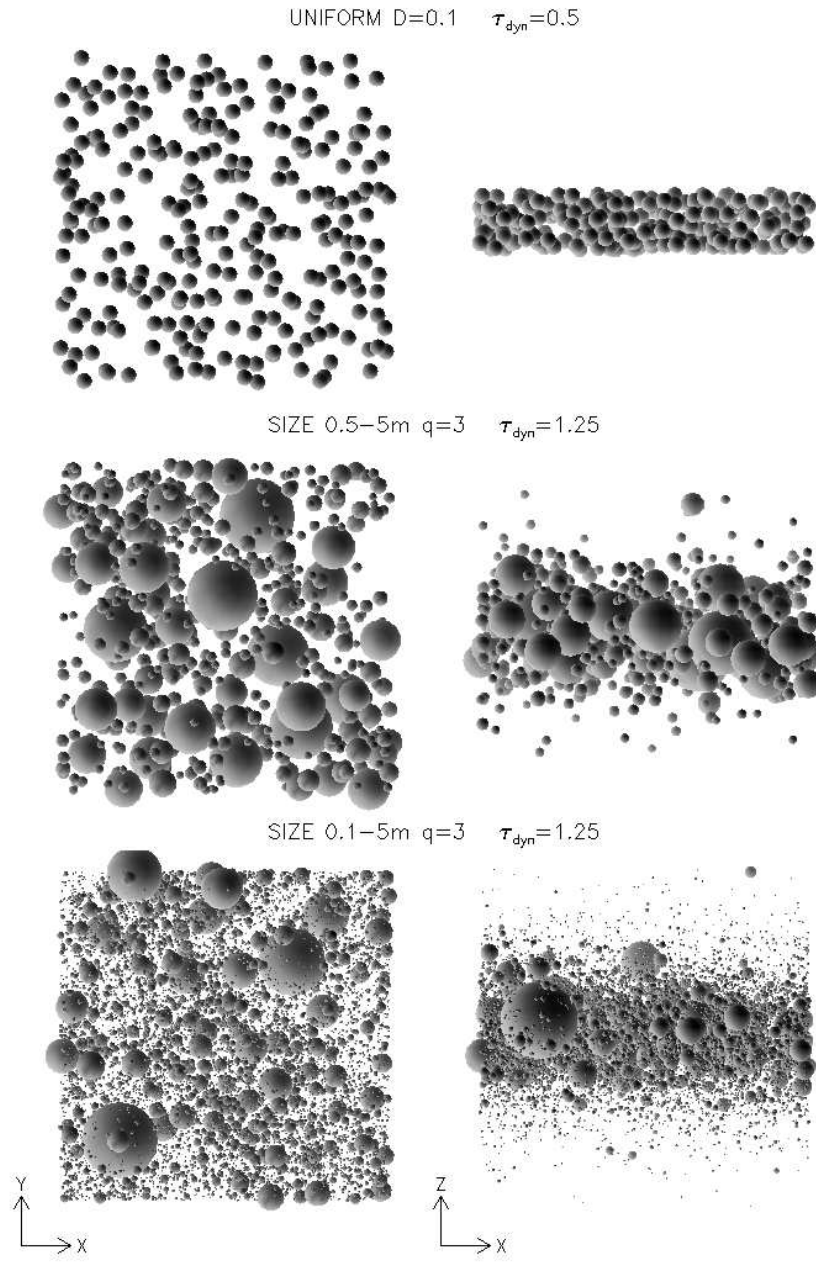


Fig. 2.

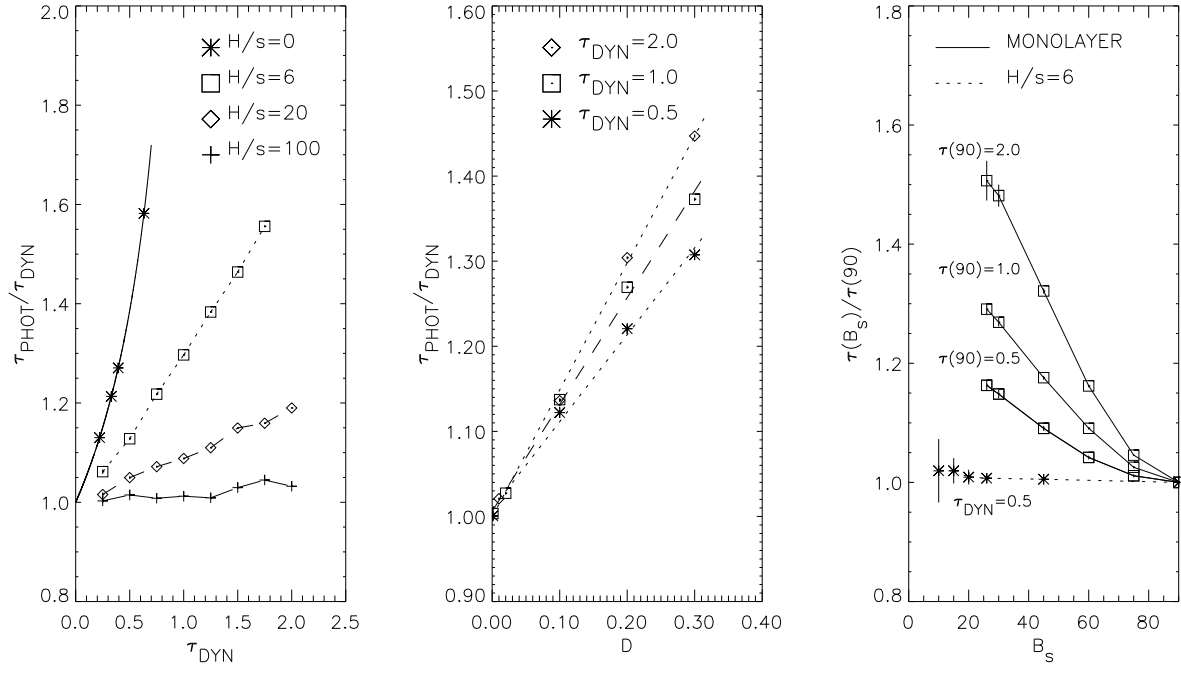


Fig. 3.

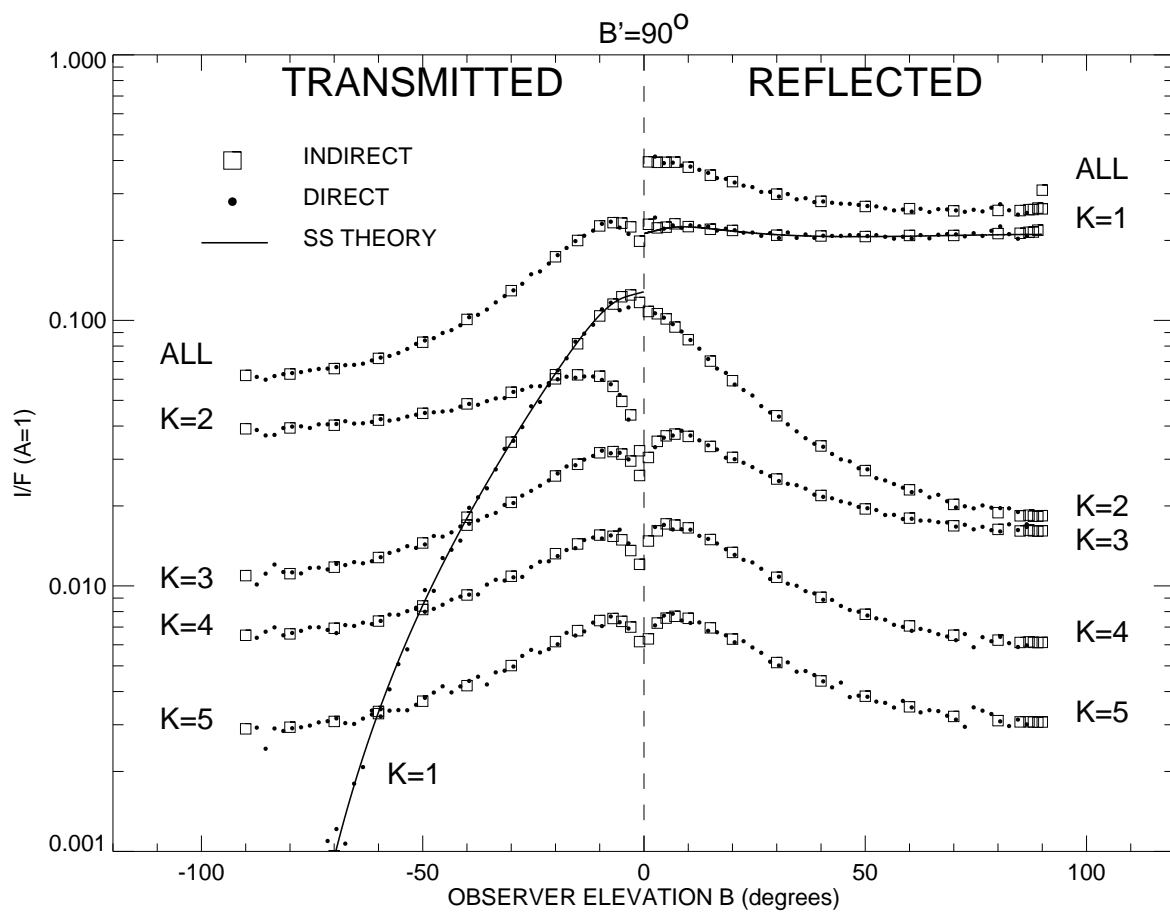


Fig. 4.

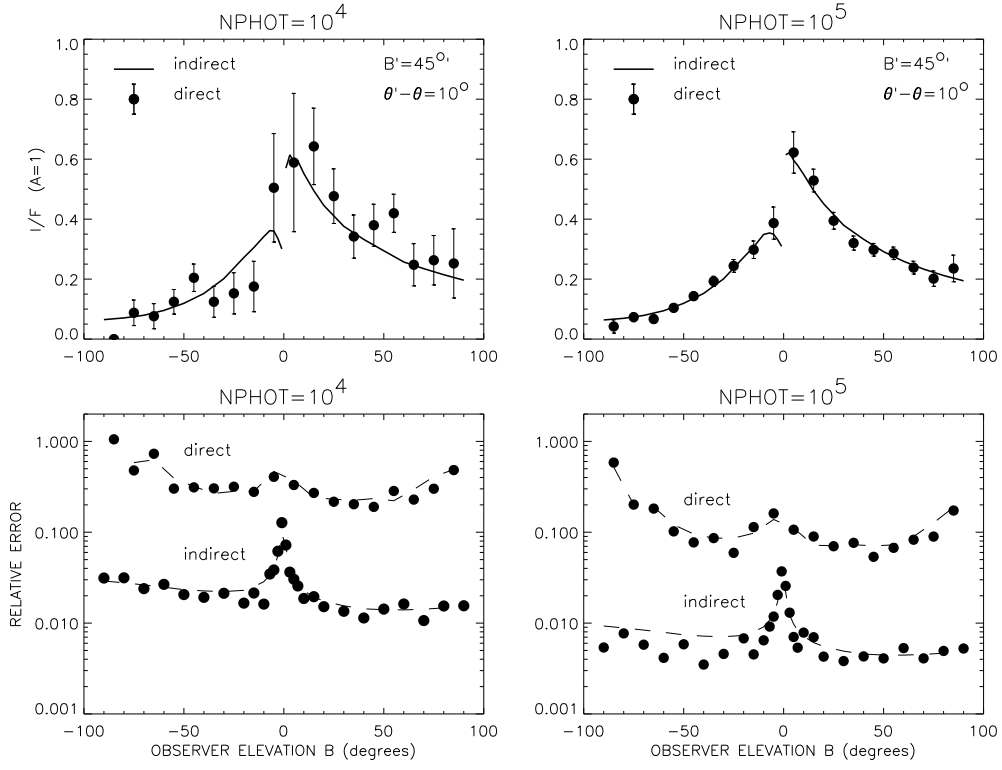


Fig. 5.



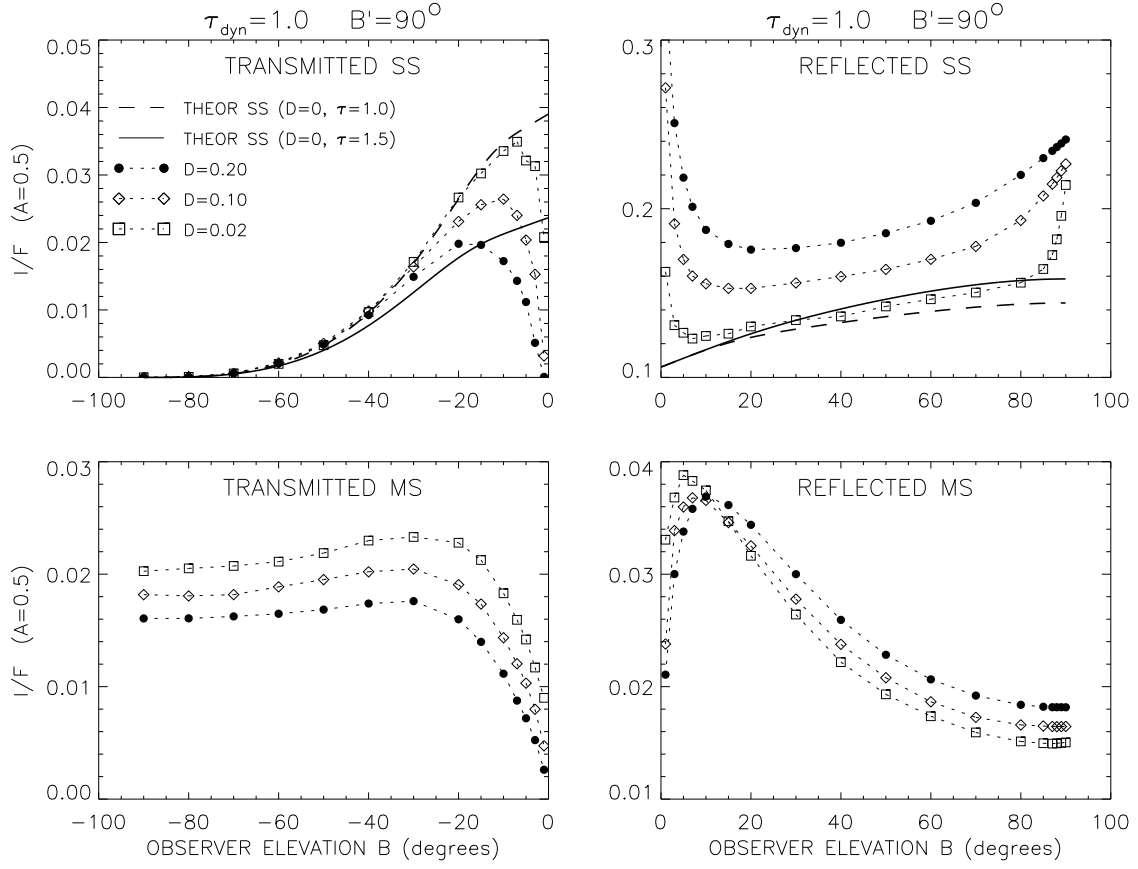


Fig. 6.

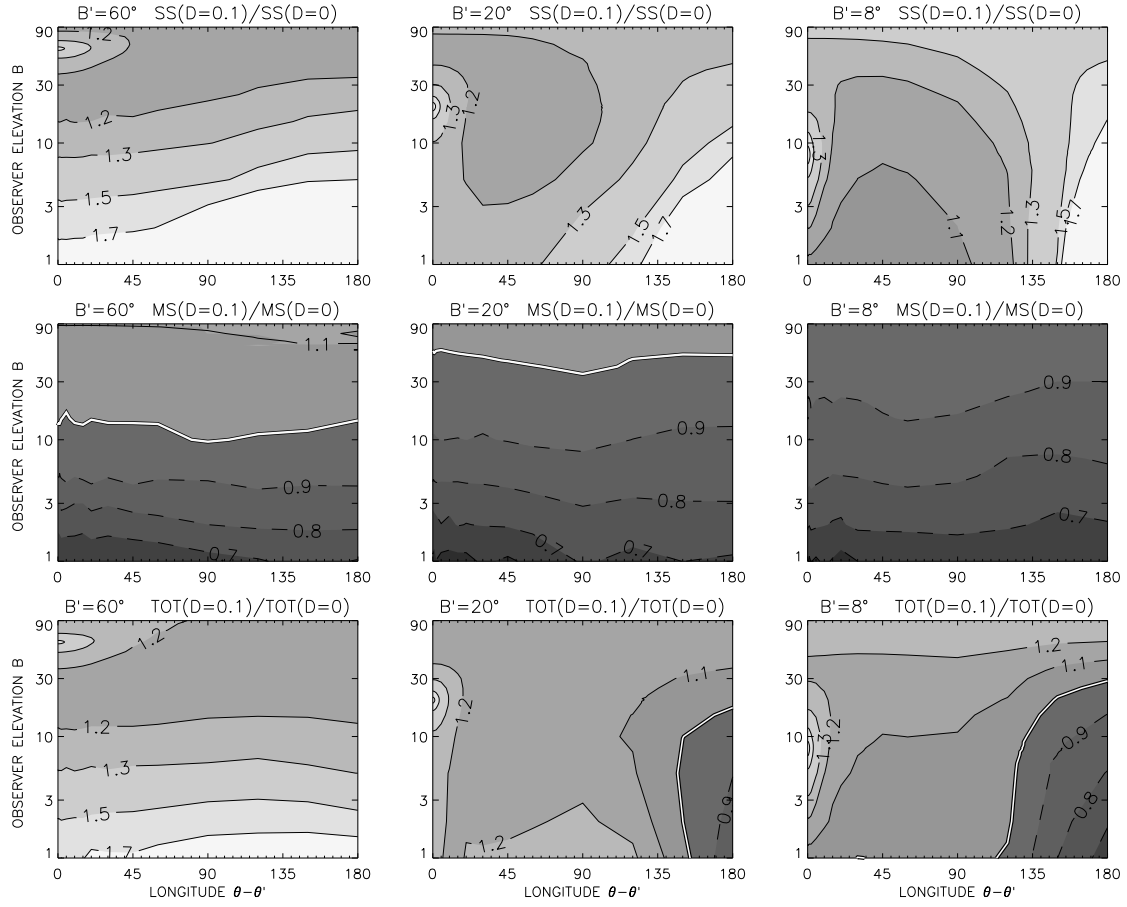


Fig. 7.

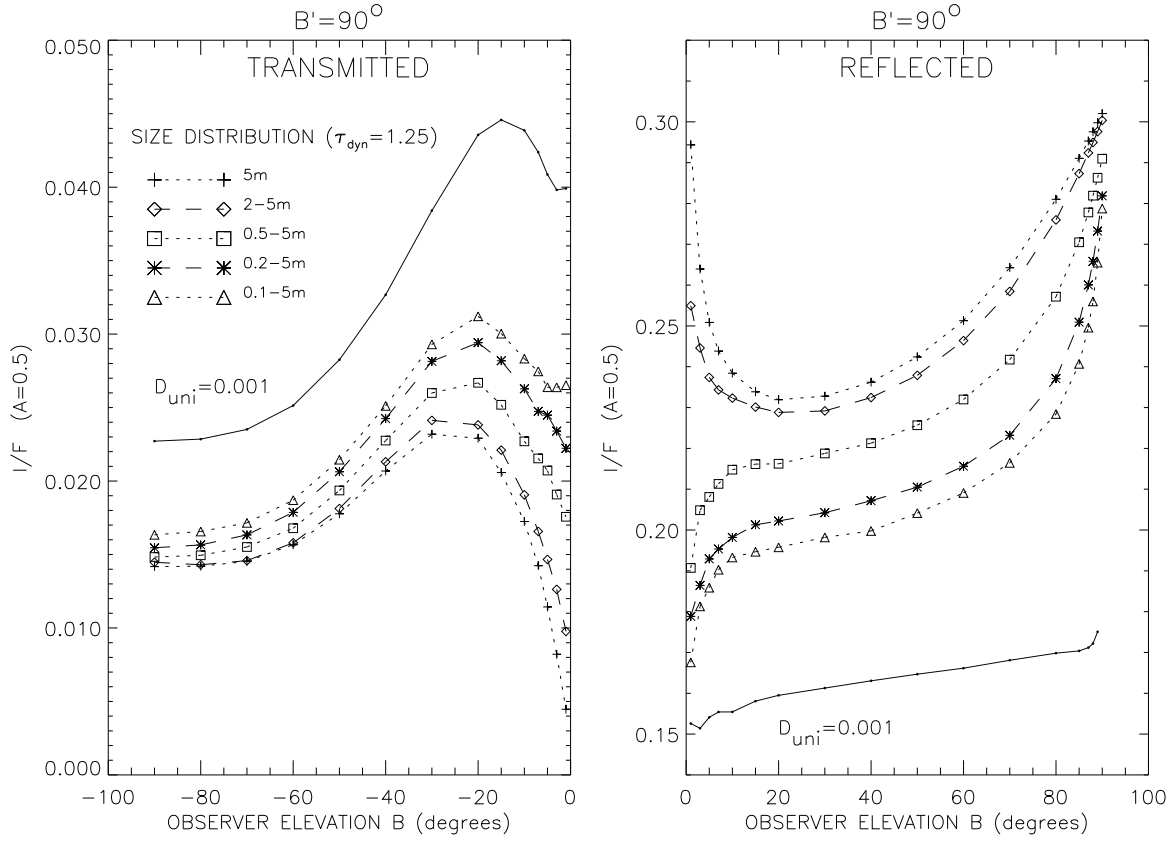


Fig. 8.

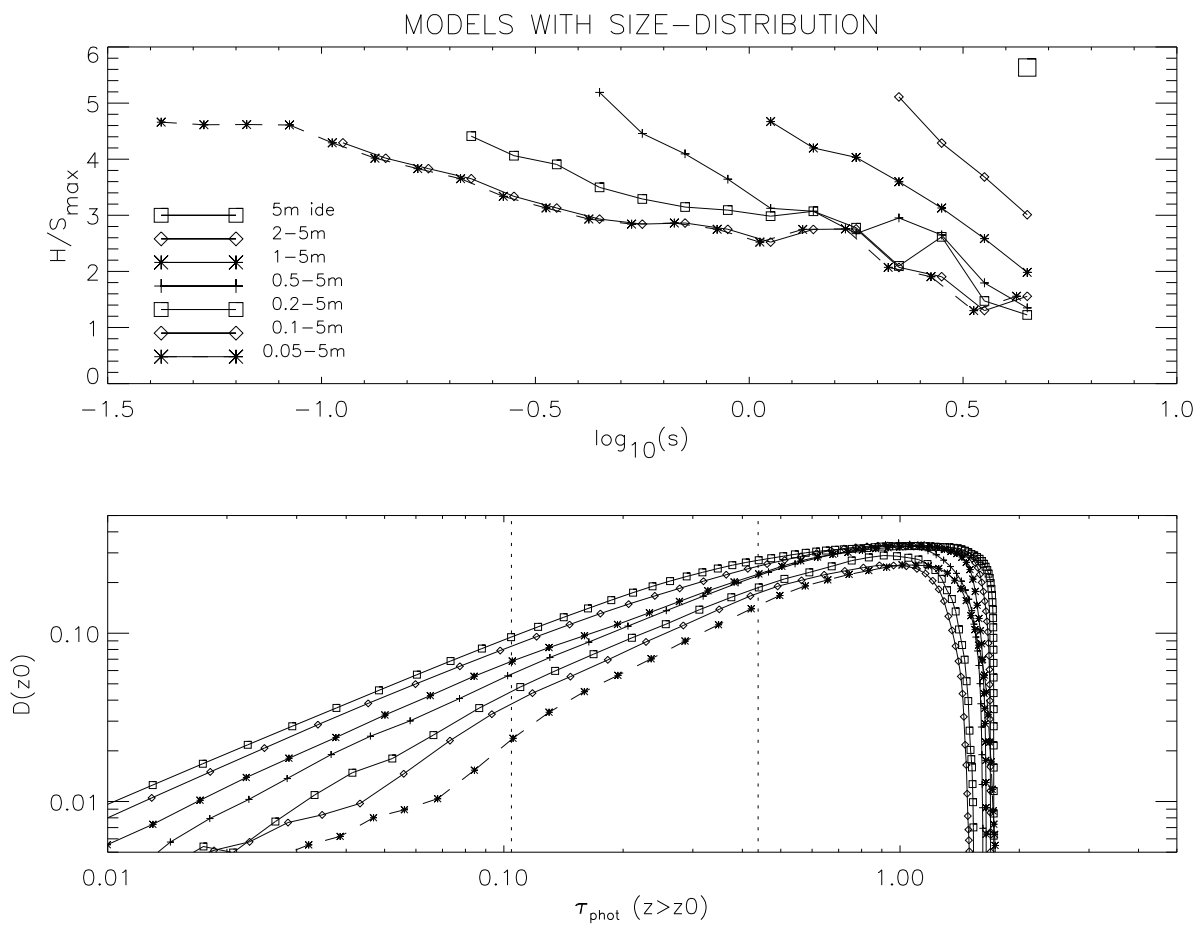


Fig. 9.

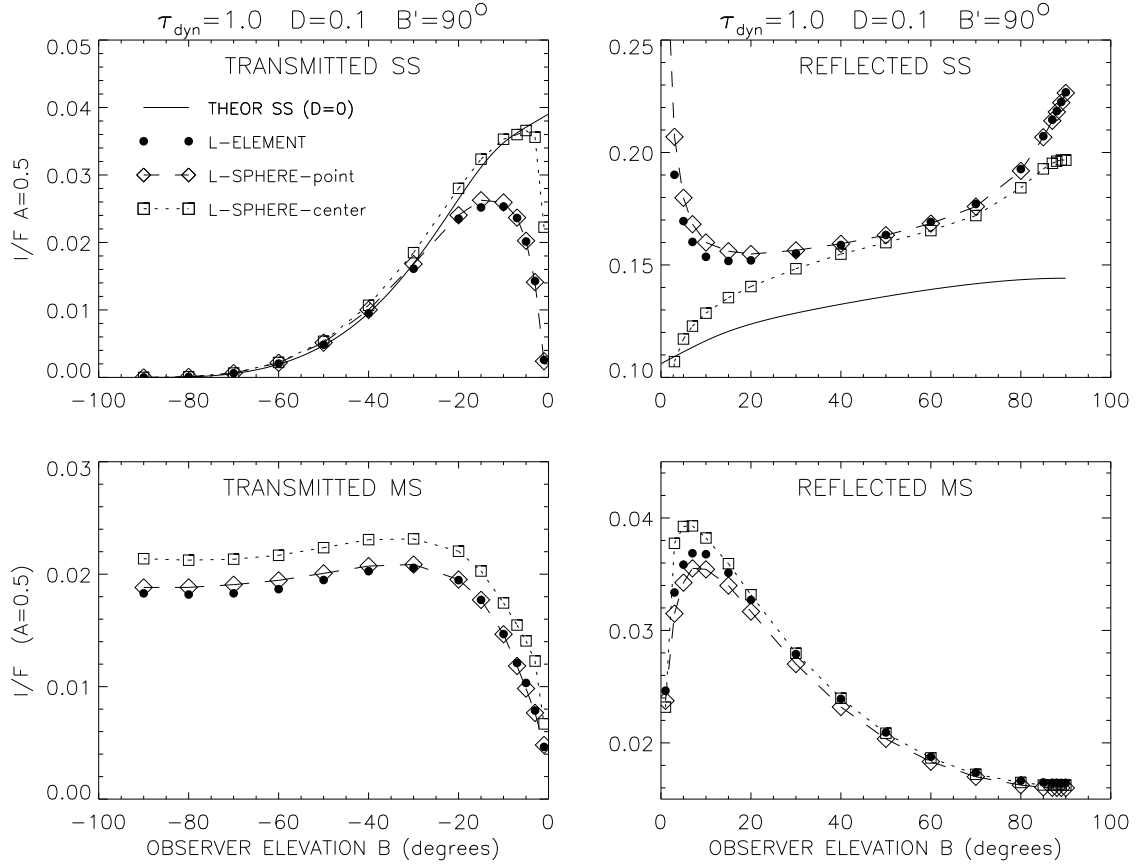


Fig. 10.

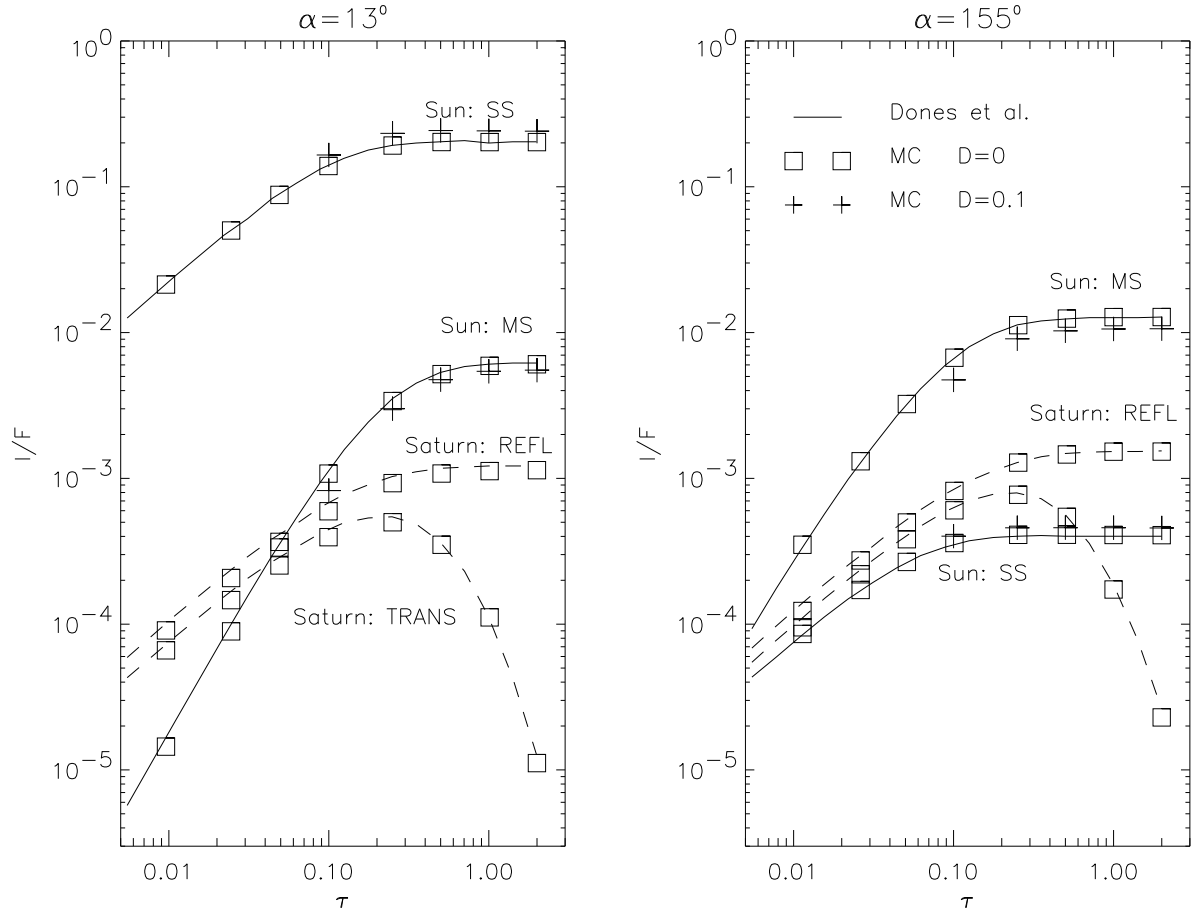


Fig. 11.

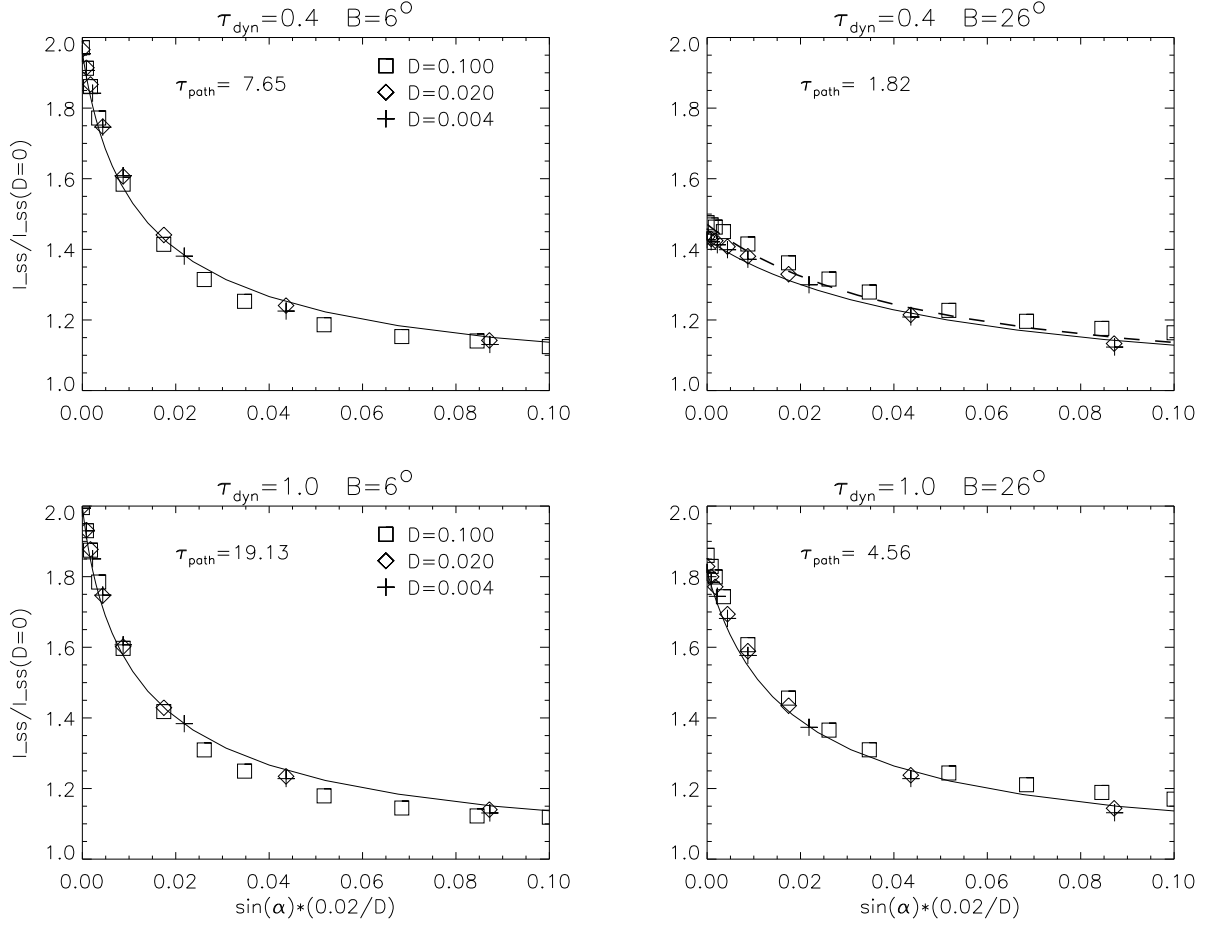


Fig. 12.

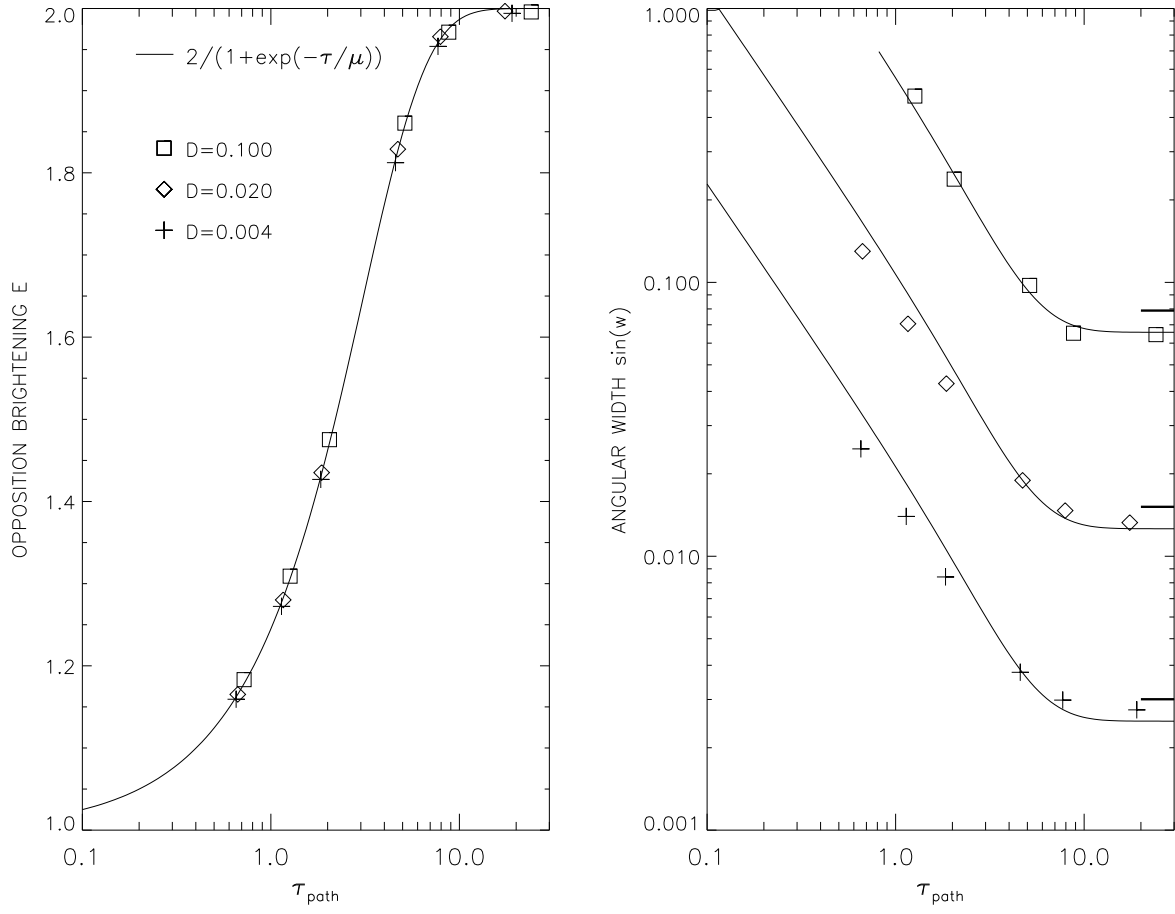


Fig. 13.



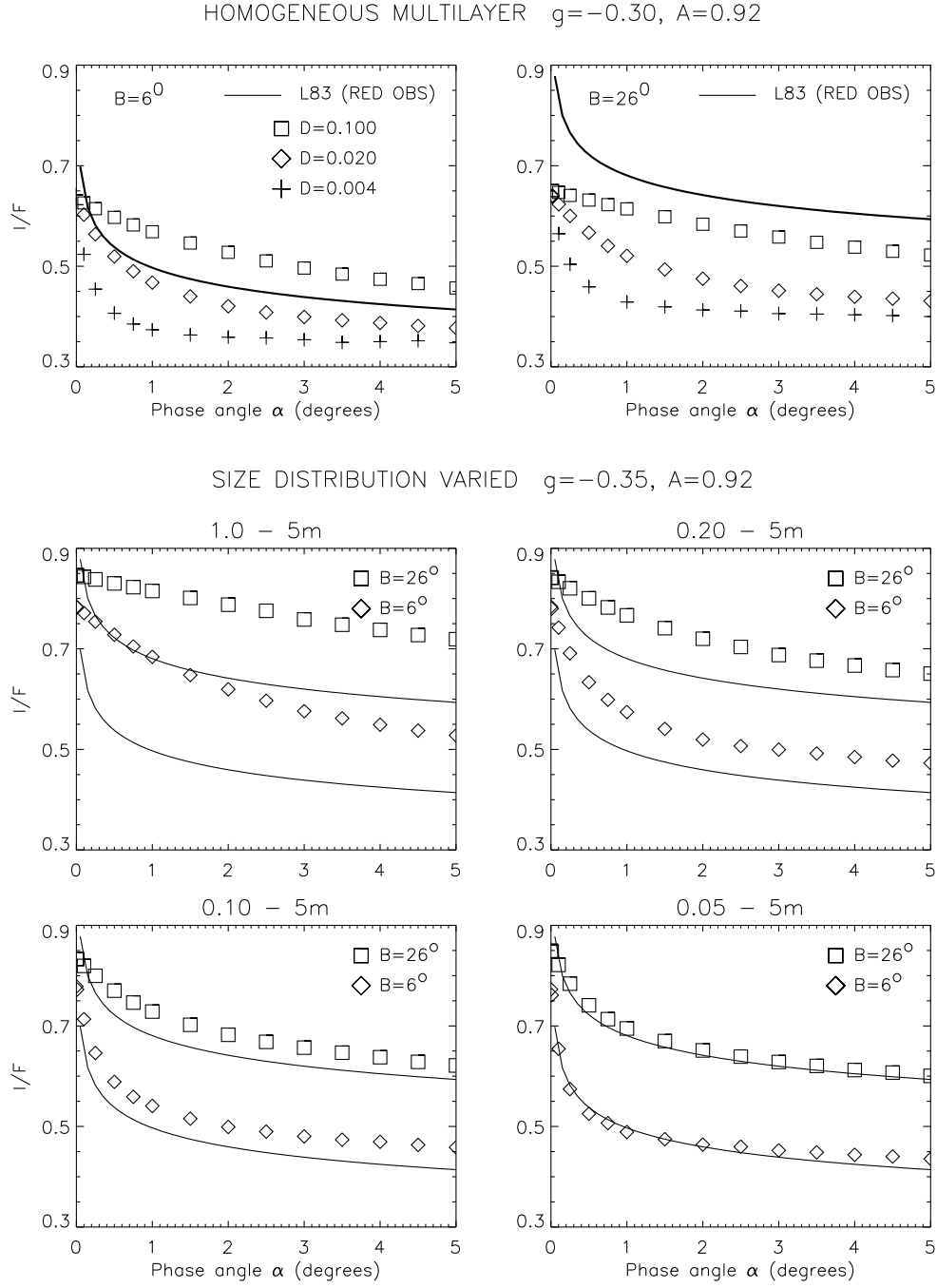


Fig. 14.

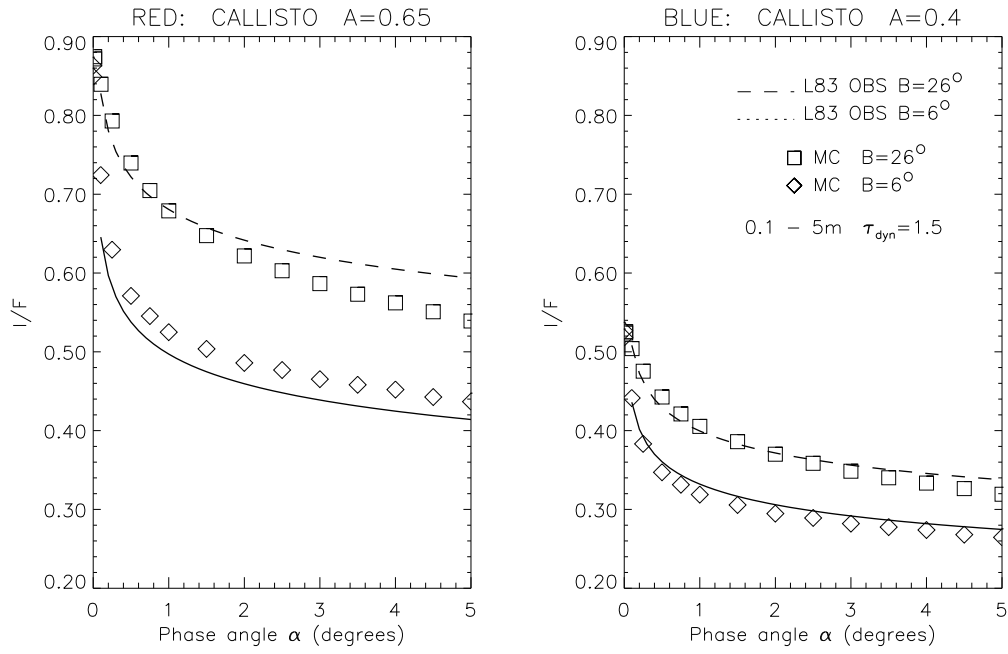


Fig. 15.

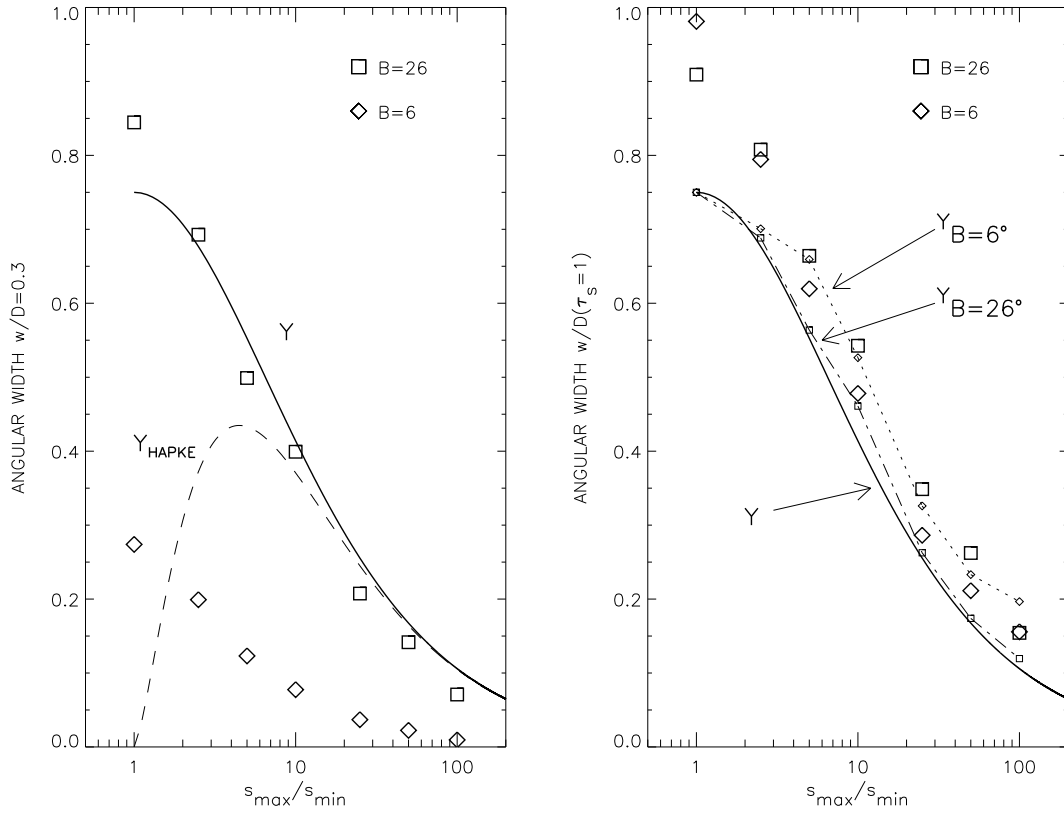


Fig. 16.

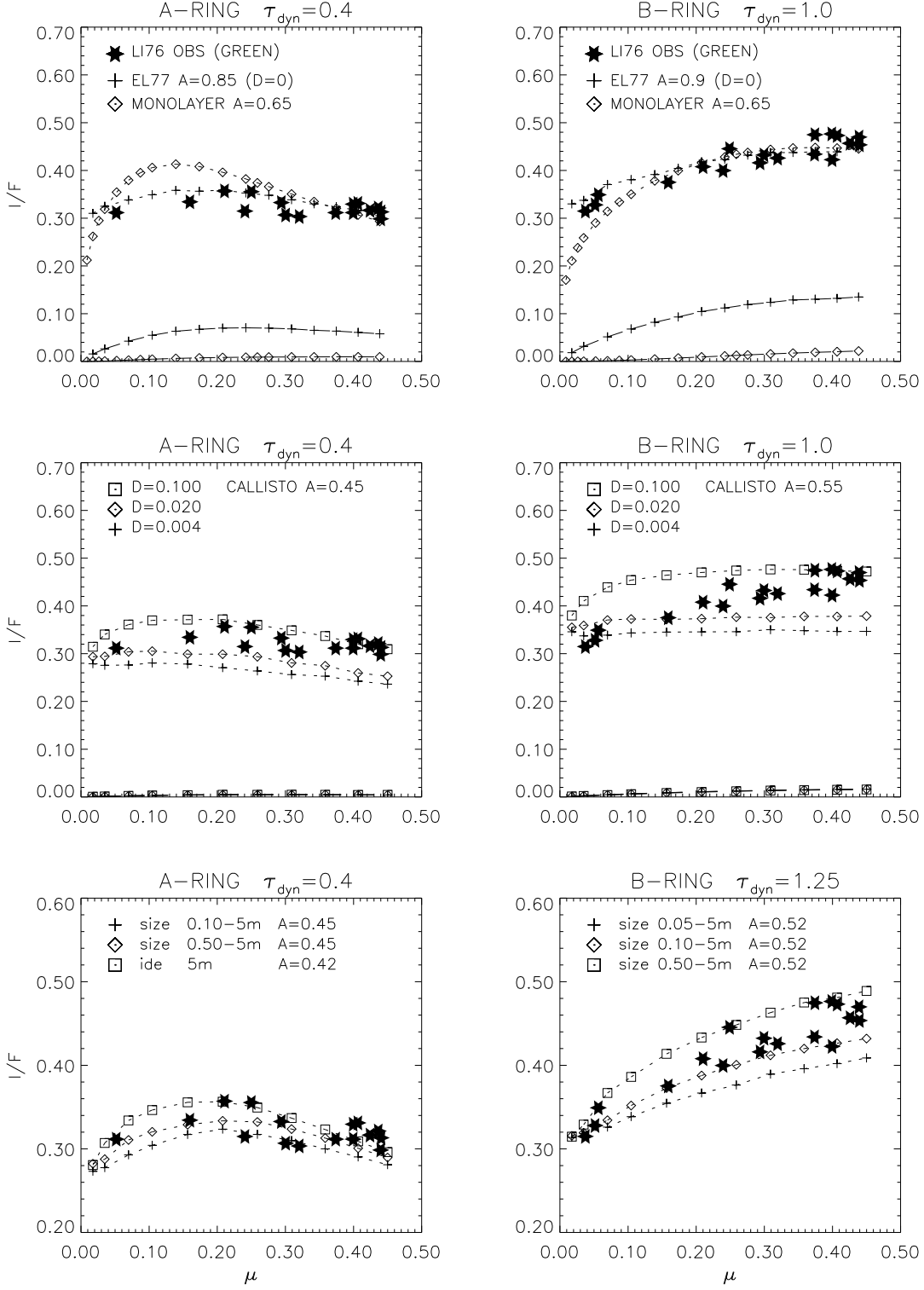


Fig. 17.

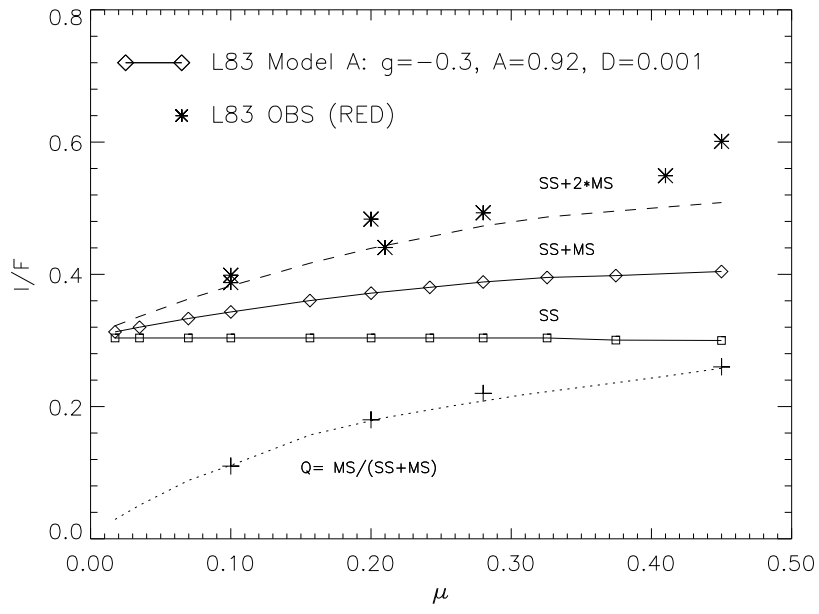


Fig. 18.

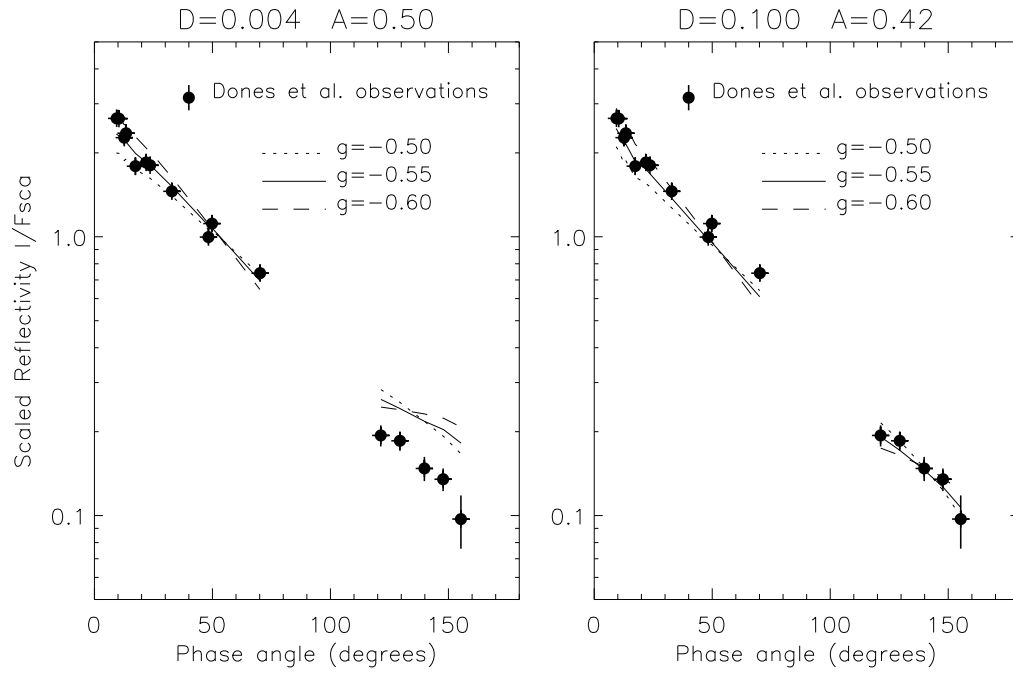


Fig. 19.

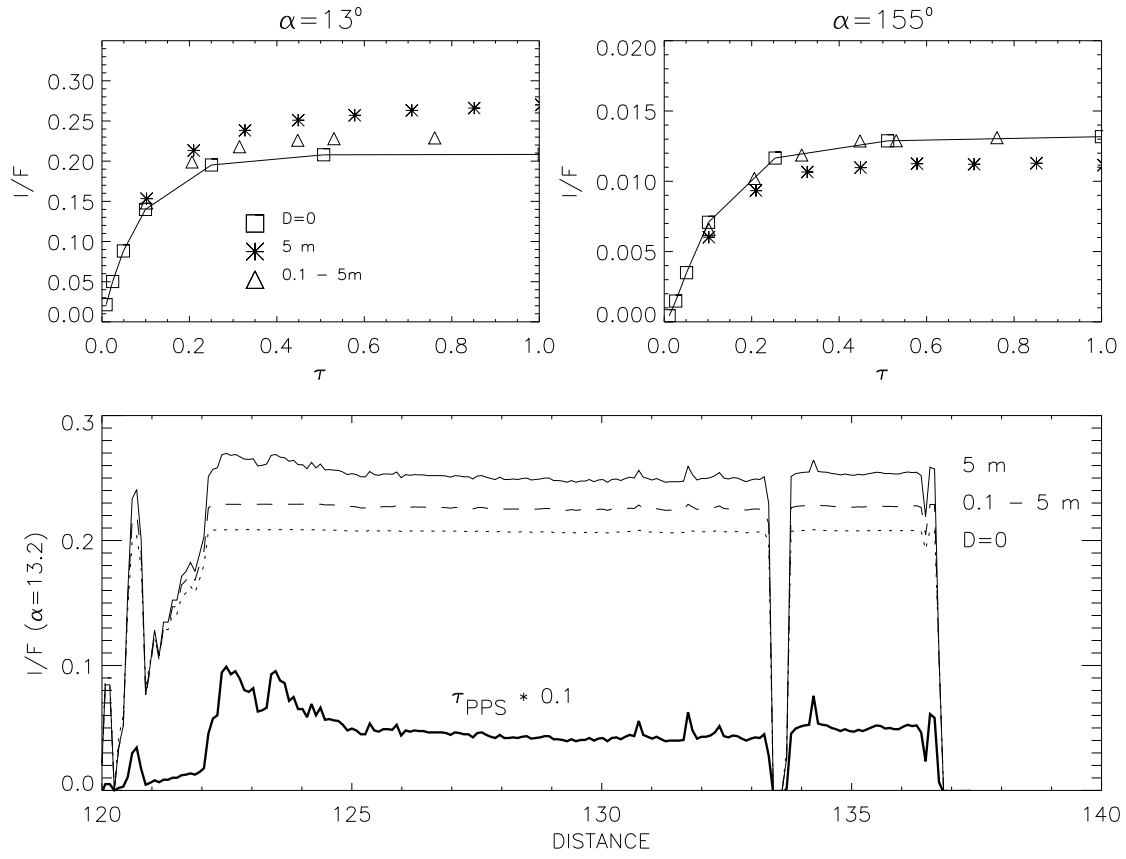


Fig. 20.

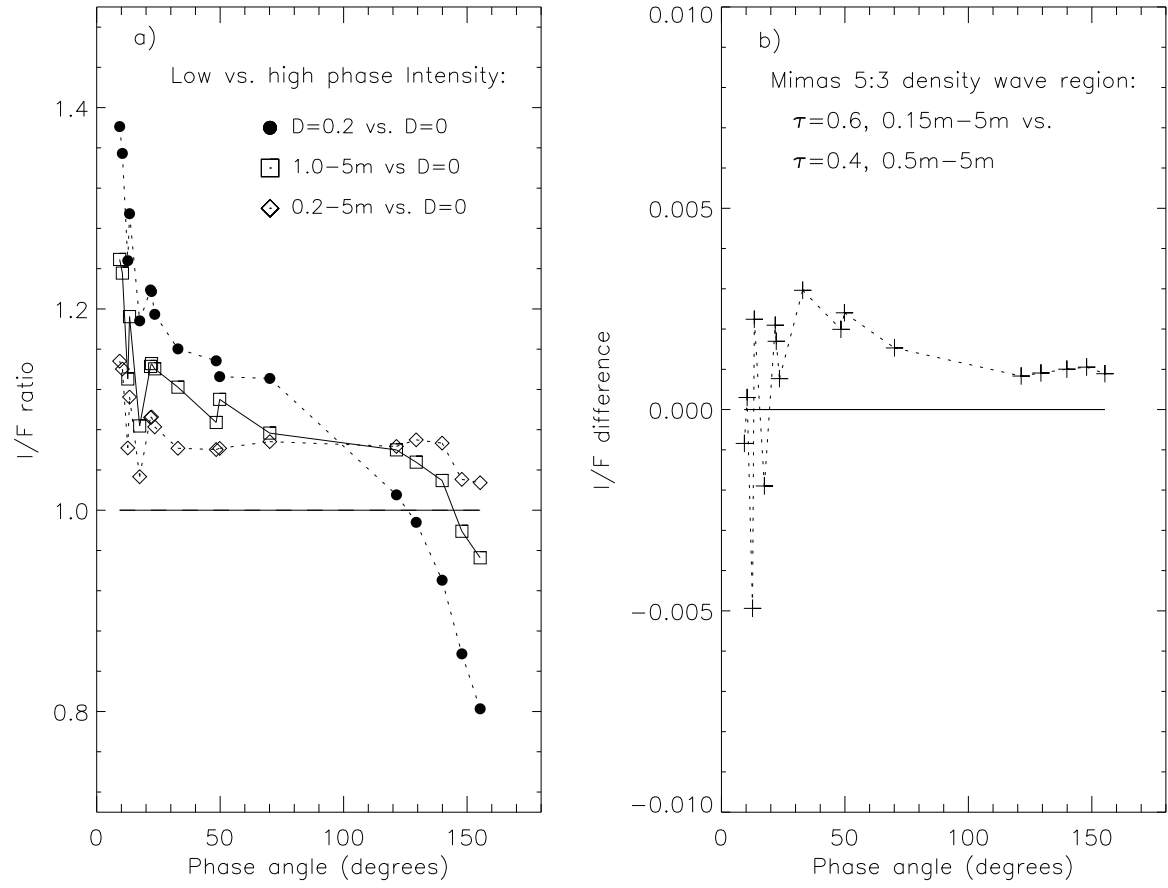


Fig. 21.



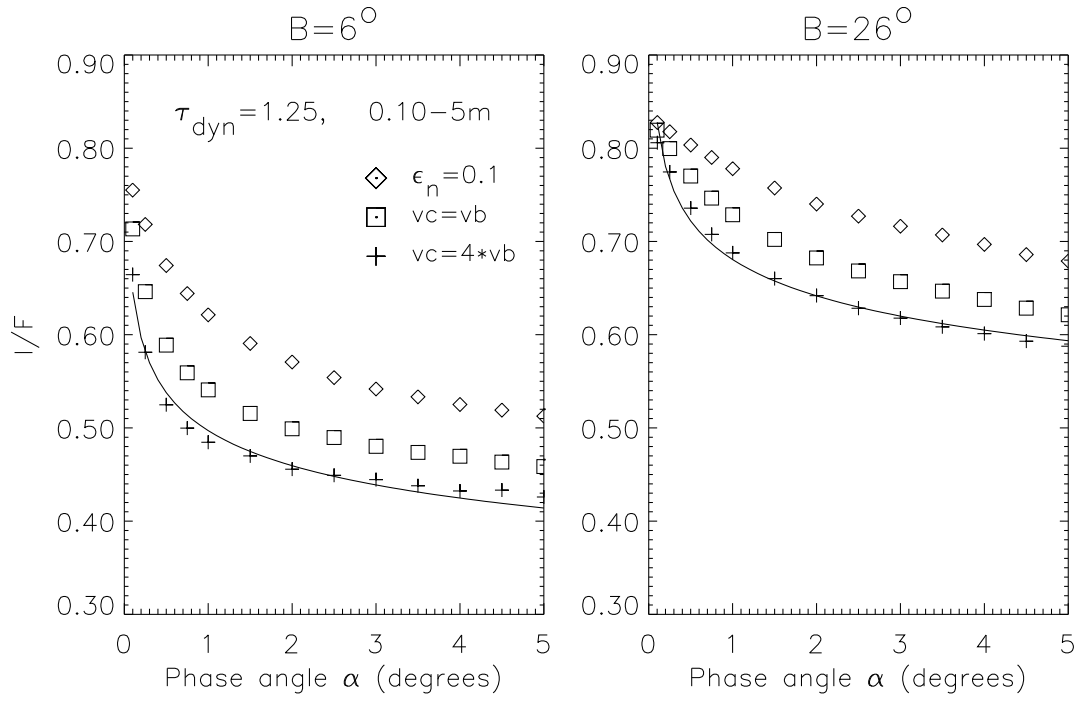


Fig. 22.